UNIVERSIDAD CARLOS III DE MADRID

DOCTORAL THESIS

ADEQUACY OF GENERATION SYSTEM WITH LARGE-SCALE DEPLOYMENT OF SOLAR POWER AND ENERGY STORAGE

Author:
Tokhir Gafurov

Director and tutor:
Julio Usaola García

Co-director:
Milan Prodanovic

Department of Electrical Engineering

Leganés, April 2015

TESIS DOCTORAL

ADEQUACY OF GENERATION SYSTEM WITH LARGE-SCALE DEPLOYMENT OF SOLAR POWER AND ENERGY STORAGE

Autor:	Tokhir Gafurov
Director y tutor:	Julio Usaola García (UC3M)
Co-director:	Milan Prodanovic (IMDEA Energía)

Firma del Tribunal Calificador:

Presidente:	Andrés Ramos
Vocal:	Manuel Matos
Secretario:	M. Ángeles Moreno López de Saá

Calificación:

Leganés, 8 de abril de 2015

A mi familia, a mis imdeanos

ABSTRACT

Solar power and energy storage technologies are expected to have a large contribution in future electricity supply mix. This implies their significant impact on generation system adequacy (GSA) and creates the need for their inclusion into reliability studies. The most precise approach for performing such analyses, particularly in the presence of time-dependent power sources and complex operating policies, is the sequential Monte Carlo (SMC) technique.

The general objective of this thesis was to develop new or adapt the existing models for creating chronological time series of power production/consumption from solar power and energy storage plants that would allow incorporating the given power sources into the SMC-based adequacy assessments. The final models had to be reasonably simplified to reduce the overall calculation time. The simplification also concerned the minimization of the required specific knowledge and input data.

To achieve the goal of the thesis, the following four tasks were completed. *First*, a solar radiation model (SRM) was developed to create synthetic values of the hourly total, beam and diffuse radiation for single or multiple locations. SRM represents a set of single-site univariate stochastic algorithms and other auxiliary models which deploy the clearness index as a primary predictor. The SRM extension for multiple locations, i. e. incorporation of the spatial correlation of solar radiation (SCSR), was accomplished in two steps. In the first step a hypothesis was made that at long timescales simple characterizations of SCSR are possible. To prove the hypothesis, the author performed a regression analysis of the satellite-derived monthly and daily values of the clearness index for over 300,000 location pairs in 4 US regions; the given analysis is an original contribution of the thesis. In the second step, by applying the derived SCSR formulae and the existing methods of linear algebra, a general procedure was introduced for incorporating SCSR into stochastic algorithms. The performed validation studies showed that the proposed individual modifications and procedures are effective and SRM, overall, provides the synthetic solar radiation data of good quality.

Second, simplified models of photovoltaic and concentrated solar (parabolic trough and central receiver based) power plants were developed for translating solar radiation to the corresponding power production. The proposed photovoltaic system model combines the Hay-Davies-Klucher-Reindl correlation for calculating solar radiation on a tilted surface and a reduced version of the 5-parameter model for converting the incident radiation to net power output. The new concentrated solar power models use a simplified simulation procedure consisting of three steps: (a) calculation of the solar field thermal output, (b) plant dispatch and conversion of useful thermal energy to gross power, and (c) estimation of parasitic losses and net production. The results from the validation studies, using the System Advisor Model as a reference, demonstrated the adequacy of the adopted approaches to model reductions.

Third, a general dispatch model was developed for energy storage system (ESS) taking into account the inherent characteristics of the simulation-based adequacy evaluations. It represents another original contribution of the thesis. According to the proposed approach, energy storage is deployed to reduce the renewable energy curtailments and thermal generation capacity, which allows natural combination of its normal and emergency operations. The main novelties in this case are: (a) the use of detrended residual load during ESS control to be able to consider renewable power production and distinguish between different operating timescales, and (b) the correction of ESS dispatch based on the classical proportional integral controller technique to achieve a realistic representation of the storage level variations. The individual calculation steps of the proposed methodology were demonstrated through a simple adequacy analysis of a generation system comprising thermal power plants and hydroelectric ESS with annual and daily operating cycles.

And finally, a case study of GSA in peninsular Spain was performed. The focus areas of the study were limited to: (a) adequacy of the existing Spanish generation system and the level of redundancy, (b) capacity credit of time-dependent power sources, and (c) sensitivity of the final results to certain modeling aspects. The Spanish power system was represented by system load, thermal generation, renewable energy sources (wind, solar and run-off-the-river hydro) and ESS (reservoir-based hydro). The excess of thermal generation and the capacity credits of the time-dependent power sources were estimated by using the effective load carrying capability as the metric. The study demonstrated how the new solar power and energy storage dispatch models could be applied to the Monte Carlo based GSA assessments, and provided additional knowledge on generation adequacy in Spain.

RESUMEN

Se espera que las tecnologías de energía solar y de almacenamiento energético vayan a tener una gran contribución al suministro eléctrico del futuro. Esto supone un impacto enorme de dichas tecnologías sobre la adecuación del sistema de generación (GSA) y hace necesario incorporarlas en los estudios de fiabilidad. El enfoque más preciso para este tipo de análisis, sobre todo en presencia de fuentes de energía intermitentes, es el método de Monte Carlo secuencial (SMC).

El objetivo general de esta tesis es desarrollar los modelos de energía solar y almacenamiento energético que permiten crear las series temporales de generación o demanda eléctrica de dichas fuentes de energía para las evaluaciones de adecuación basadas en las simulaciones de SMC. Los modelos finales tuvieron que ser simplificados para reducir el tiempo de cálculo. La simplificación incluyó también la reducción al mínimo de los conocimientos necesarios sobre las plantas de generación y los datos de entrada requeridos.

Para conseguir el objetivo de la tesis, se realizaron las siguientes cuatro tareas. *Primero*, se desarrolló un modelo de la radiación solar (SRM) para crear los valores sintéticos horarios de la radiación global, directa y difusa en una ubicación o en múltiples ubicaciones. El SRM representa un conjunto de algoritmos estocásticos univariantes de una ubicación y otros modelos auxiliares que utilizan el índice de claridad como una variable de predicción. La extensión del SRM para múltiples ubicaciones, es decir, la incorporación de la correlación espacial de la radiación solar (SCSR), se realizó en dos pasos. En el primer paso se planteó la hipótesis de que la caracterización simple de SCSR es posible en las escalas de tiempo largas. Para probar la hipótesis, se llevó a cabo un análisis de regresión de los valores mensuales y diarios del índice de claridad obtenidos por el satélite para más de 300,000 pares de ubicaciones en 4 regiones de EEUU; este análisis es una contribución original de la tesis. En el segundo paso, mediante de las formulas derivadas de SCSR y de los métodos existentes de álgebra linear, se introdujo el procedimiento general para incorporar la correlación espacial en los algoritmos estocásticos. Los estudios de validación realizados mostraron que los modelos y procedimientos individuales son eficaces, y SRM, en su conjunto, proporciona datos de la radiación solar fiables.

En segundo lugar, se desarrollaron modelos simplificados de plantas solares fotovoltaica y termoeléctrica (cilindro-parabólico y torre central) para transformar la radiación solar en la producción eléctrica correspondiente. El modelo propuesto del sistema fotovoltaico combina la correlación de Hay-Davies-Klucher-Reindl para calcular la radiación solar sobre una superficie inclinada y la versión reducida del modelo de 5 parámetros para convertir la radiación incidente en la potencia neta. Los nuevos modelos de solar termoeléctrica usan un procedimiento simplificado de tres pasos: (a) cálculo de la producción térmica del campo solar, (b) despacho de la planta y conversión de la

energía térmica útil en la potencia eléctrica bruta, (c) estimación de las pérdidas parasitas y la potencia neta. Los resultados de los estudios de validación con System Advisor Model como referencia demostraron la idoneidad de los enfoques adoptados para la reducción de los modelos.

En tercer lugar, se desarrolló un modelo de despacho general para el sistema del almacenamiento energético (ESS) teniendo en cuenta las características de las evaluaciones de GSA basadas en simulaciones. Este modelo representa otra contribución original de la tesis. Según el enfoque propuesto, el almacenamiento energético se despliega para reducir la capacidad de la generación convencional y el acortamiento de las energías renovables, lo que permite la combinación natural de la operación normal y la de emergencia. Las principales novedades en este caso son: (a) el uso de la demanda residual desestacionalizada durante el control de ESS para poder considerar la producción renovable y distinguir entre varias escalas de tiempo de funcionamiento, y (b) la corrección del despacho de ESS basada en el control clásico proporcional e integral para conseguir la representación realista de las variaciones del nivel de la energía almacenada. Los pasos individuales del cálculo se ilustraron mediante un simple análisis de adecuación de un sistema de generación que consta de centrales térmicas y ESS hidroeléctrico con ciclos de funcionamiento anual y diario.

Y por último, se ha realizado un estudio de caso de GSA en España peninsular. Las áreas del estudio se limitaron a las siguientes: (a) adecuación del sistema de generación existente y el nivel de redundancia, (b) crédito de capacidad de las fuentes de energía intermitentes, y (c) sensibilidad de los resultados finales a ciertos aspectos del modelado. La representación del sistema eléctrico peninsular español incluye la demanda, la generación térmica, las energías renovables (eólica, solar y hidráulica fluyente) y ESS (hidráulica de embalse). El exceso de la generación térmica y el crédito de capacidad de las fuentes intermitentes fueron estimados usando la capacidad efectiva para soportar carga (ELCC) como métrica. El estudio demostró cómo se pueden aplicar los nuevos modelos de la energía solar y del despacho del almacenamiento energético en las valoraciones de GSA basadas en las simulaciones de Monte Carlo, y proporcionó conocimientos adicionales sobre la adecuación de la generación en España.

PUBLICATIONS

Some results of this work have been mentioned previously in the following publications:

- T. Gafurov, J. Usaola, and M. Prodanovic. PV system model reduction for reliability assessment studies. In *Proc. of IEEE ISGT-Europe*, October 2013.
- T. Gafurov, J. Usaola, and M. Prodanovic. Modelling of concentrating solar power plant for power system reliability studies. *IET Renewable Power Generation*, vol. 9 (2), pp. 120–130, March 2015.
- T. Gafurov, J. Usaola, and M. Prodanovic. Incorporating spatial correlation into stochastic generation of solar radiation data. *Elsevier Solar Energy*, vol. 115, pp. 74–84, May 2015.
- T. Gafurov, J. Usaola, and M. Prodanovic. Modelling of energy storage dispatch for generation system adequacy studies. *IET Generation, Transmission & Distribution* (under review)

"All paths lead nowhere; but one has a heart, the other doesn't. One makes for a joyful journey; as long as you follow it, you are one with it. The other will make you curse your life. One makes you strong; the other weakens you."

— Carlos Castañeda

ACKNOWLEDGMENTS

I would like to thank *Institute IMDEA Energy*, in particular *Electrical Systems Unit*, for the opportunity to work as a predoctoral researcher and to write this thesis.

I would like to express my deepest gratitude to my supervisors *Prof. Julio Usaola* and *Dr. Milan Prodanovic* for their continuous support of my PhD research, for their patience, encouragement, and insightful comments.

I must also acknowledge *Jan Remund* from Meteotest and *Dr. Paul Denhom* from NREL for their assistance on certain aspects of solar energy modeling.

A very special thanks goes to my family and friends who are far away, but are still with me in my heart.

And finally, I would like to thank all wonderful people I met during my stay in Madrid. Thank you for sharing with me this journey!

CONTENTS

LIST OF FIGURES

LIST OF TABLES

In this work, all symbols are explained in each chapter the first time they are used. The following list includes only the general or most used symbols and not variations, usually denoted with subscripts. The symbols with prime x', star x^* and hat $\widehat{x}$ refer to transformation, normalization and averaging, respectively. Since the minimum considered time interval is an hour, the power value is the same as the hourly energy amount.

ENGLISH SYMBOLS

A_{pv}	Total area of modules in PV system (m^2)
A_{sf}	Solar field (collector aperture or heliostat mirror) area in CSP plant (m^2)
C_r	Correlation matrix for random number streams
CAP_{avail}	Available capacity of dispatchable generation (W)
CapFac	ESS capacity factor in consumption (in) or production (out) mode
d_{hel}	Distance between heliostat and central receiver (km)
d_{site}	Distance between two sites (km)
E	Reservoir energy capacity (Wh)
F_{in}, F_{out}	Power thresholds during ESS dispatch for valley filling and peak shaving (W)
$G_{o,n}$	Normal extraterrestrial solar irradiance (W/m^2)
H_{tot}, H_o	Daily terrestrial and extraterrestrial solar radiation on a horizontal plane (Wh/m^2)
H_h	Net hydraulic head (m)
h_{hel}	Height of heliostat mirror (m)
h_{tower}	Height of central tower (m)
I_{tot}, I_o	Hourly terrestrial and extraterrestrial solar radiation on a horizontal plane (Wh/m^2)
I_b, I_d	Hourly beam and diffuse radiation on a horizontal plane (Wh/m^2)
$I_{b,n}$	Hourly normal beam (direct) radiation (Wh/m^2)
$I_{(b,d,g),T}$	Hourly beam, diffuse and ground-reflected solar radiation on a tilted plane (Wh/m^2)
$I_{sf,min}$	Minimum hourly normal beam radiation required for CSP plant operation (Wh/m^2)
K_P, K_I	Proportional and integral gain constants used in the ESS dispatch model (non-dimensional equivalents are k_p and k_i, respectively)
KT	Clearness index
KT_{base}	Trend (base) component of the hourly clearness index

KT_{rand}	Random component of the hourly clearness index
$\widehat{KT}_{month}$	Average monthly clearness index
L_{pb}	Relative loading of power block in CSP plant ($Q_{pb}/Q_{pb,nom}$)
L_{sys}	System load (W)
M_{air}	Optical air mass
$N_{hel,z}$	Number of heliostats in a given field zone
N_Y	Number of simulation years
N_P	Number of operating periods per year for ESS
n_p	Polynomial degree
P	ESS power (W)
P_{csp}	Gross power from CSP plant (W)
$P_{csp,net}$	Net power from CSP plant (W)
P_{pv}	Gross power from PV system (W)
$P_{pv,net}$	Net power from PV system (W)
P_{RES}	Power from all RES (W)
P_{ror}	Power from run-off-the-river plant (W)
PL_{csp}	Total parasitic power losses in CSP plant (W)
PL_{pv}	Total parasitic power losses in PV system (W)
r, r_{corr}	Uncorrelated and correlated random numbers
Q	Energy carrier flow from storage to conversion unit of ESS
Q_{pb}	Thermal power delivered to power block in CSP plant (W)
$Q_{rec,loss}$	Fixed thermal power loss in central receiver (W)
Q_{sf}	Thermal power from solar field in CSP plant (W)
$Q_{sf,warm}$	Required warm-up energy for solar field in CSP plant (Wh)
Q_{sink}	Hourly energy carrier flow from conversion unit to primary sink of ESS
R^2	Coefficient of determination
RL	Residual load (W)
RL_{trend}	Trend component of residual load (W)
S	Unknown energy carrier flow from storage to primary sink of ESS
SM_{csp}	Solar multiple of CSP plant
T_{amb}	Ambient air temperature (°C)
T_{HTF}	HTF average temperature (°C)
T_{pv}	PV cell temperature (°C)
T_{rise}, T_{set}	Local time at sunrise and sunset (hours)
T_{tes}	Capacity of thermal storage in equivalent number of the full load hours (hours)
t_Y	Number of hours in a year
t_C	Length of the ESS operating cycle (hours)
U	Upper triangular matrix in the Cholesky factorization

V	Storage level for ESS (e.g. water volume in reservoir)
V_{aver}	Long-term average value of storage level for ESS
$\widehat{V}_{ref}$	Reference profile of storage level variations for ESS
W_{in}	Energy carrier flow from primary source to storage unit of ESS
W_{loss}	Energy carrier loss from storage unit of ESS
W_{out}	Known energy carrier flow from storage to primary sink of ESS
w_{hel}	Width of heliostat mirror (m)
X_j	Mathematical indicator for intersite dependence (MIID)
x_{hel}, y_{hel}	Cartesian coordinates of given point in heliostat field (m)
y, y'	Actual and predicted values of a given variable
Z	Hourly precipitation (m^3)
Z_s	Surface azimuth angle (degrees)

GREEK SYMBOLS

α_s	Solar altitude angle (degrees)
β	Slope (tilt) angle (degrees)
β_{Voc}	Normalized temperature coefficient of the open-circuit voltage
γ_s	Solar azimuth angle (degrees)
ΔA_{hel}	Azimuthal spacing between heliostats (m)
ΔKT	First difference (ramp rate) of the clearness index series
ΔR_{hel}	Radial spacing between heliostats (m)
ΔRL	Detrended residual load (W)
ΔY_{ab}	Relative position of the additional boundary applied during zoning of heliostat field (m)
$\Delta\lambda$	Difference between standard and local longitude angles (degrees)
δ	Solar declination (degrees)
$\eta_{hel,refl}$	Reflectivity of heliostat mirror
$\eta_{hel,atm}$	Heliostat efficiency due to atmospheric attenuation
η_h	Hydro-to-power efficiency
η_{pb}	Efficiency of power block in CSP plant
$\eta_{pv,SRC}$	PV module efficiency at reference conditions
η_{pv}	PV module efficiency
η_{ptr}	Overall efficiency of parabolic trough
$\eta_{ptr,max}$	Maximum optical efficiency of parabolic trough
$\eta_{rec,abs}$	Central receiver efficiency based on absorptivity
$\eta_{rec,refl}$	Central receiver efficiency based on reflectivity
$\eta_{rec,spill}$	Central receiver efficiency based on spillage
η_{sf}	Total efficiency of solar field in CSP plant
$\eta_{sf,opt}$	Average optical efficiency of solar field in CSP plant

$\eta_{sf,other}$	Solar field efficiency in CSP plant based on other energy losses
η_{shbl}	Efficiency due to shadowing and blocking of incident radiation
η_{tes}	Round-trip efficiency of thermal storage in CSP plant
θ	Incidence angle in PV and PTR system (degrees)
θ_{hel}	Incidence angle at given point of heliostat field (degrees)
λ	Longitude angle (degrees)
λ_H	Ratio of minimum to maximum hydraulic head
λ_V	Ratio of minimum to maximum reservoir volume
ν_i	Constants in the functional relation between C_r and PCC
ρ_g	Ground albedo
υ_{a-c}	Coefficients used in defining the trend component of the hourly clearness index (see equation 5.2)
ϕ	Latitude angle (degrees)
ω	Solar hour angle (degrees)
ω_{ss}	Solar hour angle at sunset (degrees)

SUBSCRIPTS AND SUPERSCRIPTS

aver	Average
des	Design
max	Maximum
min	Minimum
nom	Nominal
ref	Reference
req	Required

ABBREVIATIONS

AST	Apparent solar time
BRL	Boland-Ridley-Lauret
CSP	Concentrated solar power
DLR	German Aerospace Center
DPG	Dispatchable generation
ENS	Energy not supplied
EOT	Equation of time
ESS	Energy storage system
GSA	Generation system adequacy
HDKR	Hay-Davies-Klucher-Reindl
HL	Hierarchical level
HPP	Conventional hydro power plant

HTF	Heat transfer fluid
IAM	Incidence angle modifier
LLD	Loss of load duration
LLO	Loss of load occurrence
LOEE	Loss of energy expectation
LOLF	Loss of load frequency
LOLE	Loss of load expectation
LST	Local standard time
MAE	Mean absolute error
MARE	Mean absolute relative error
MIID	Mathematical indicator for intersite dependence
NOCT	Nominal operating cell temperature
NREL	National Renewable Energy Laboratory
NSDD	Normalized standard deviation of difference
NSRDB	National Solar Radiation Data Base
PB	Power block
PCC	Pearson's correlation coefficient
PSP	Pumped storage hydro power plant
PTR	Parabolic trough
PV	Photovoltaic
RES	Renewable energy source (with none or low storage capacity)
RMSE	Root mean square error
ROR	Run-off-the-river
SAM	System Advisor Model
SCSR	Spatial correlation of solar radiation
SDD	Standard deviation of difference
SF	Solar field
SMC	Sequential Monte Carlo
SRC	Standard rated conditions
SRM	Solar radiation model
TAG	Time-dependent autoregressive Gaussian
TES	Thermal energy storage
TMY	Typical meteorological year

Part I

GENERAL BACKGROUND, AIM AND STRUCTURE OF THE THESIS

1 INTRODUCTION

1.1 GENERATION SYSTEM ADEQUACY

Definition

Electric power system aims to provide reliable and cost-effective electricity supply to its customers. The desired reliability is normally achieved by using spare or redundant capacities in generation and network facilities, which obviously incurs additional investments. To eliminate or reduce the excessive redundancy, appropriate assessment of power system reliability is required in both planning and operational phases.

In reliability assessment it is common to distinguish between two aspects: adequacy and security [16]. Adequacy refers to static conditions of power system and characterizes the existence of sufficient facilities to generate and transport the needed energy to the actual consumption points. Whereas security relates to the operating conditions and reflects the system ability to respond to dynamic and transient disturbances. Due to high modeling complexity in security domain, most of the traditional reliability evaluation techniques have been developed for adequacy studies.

Power system adequacy is categorized in terms of three functional zones: generation, transmission and distribution. Combination of these zones, as shown in Fig. 1.1, gives three hierarchical levels (HL) used in adequacy assessment. Generation system adequacy (GSA), the focus of this thesis, corresponds to hierarchical level 1 and represents the ability of generation facilities to meet the total system load by assuming that all electricity is produced and consumed at a single node, i. e. by ignoring the power network.

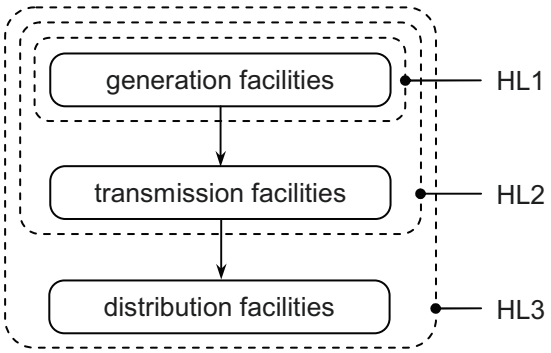

Figure 1.1: Functional zones and hierarchical levels used in adequacy assessment

Evaluation methods

The existing methods for GSA assessment can be divided into two groups: deterministic and probabilistic (Fig. 1.2). The deterministic approach is the oldest and it applies rules of thumb derived from previous experience and can express the required minimum generation reserve, for example, as a fixed fraction of the expected peak demand or as the capacity of the largest generation unit. The approach tends to overestimate the reserve requirements as it evaluates adequacy only with respect to certain hazardous events that are selected by severity without considering their actual likelihood. Due to its simplicity deterministic technique, however, is very attractive to power system planners and still widely used by utilities in European countries [25, 92].

The probabilistic methods take into account stochastic nature of the power system behavior and incorporate both risk components – severity and likelihood of the capacity shortage – into adequacy assessment, which allows higher precision. The final results in this case are usually represented by reliability indices such as loss of load expectation (LOLE) and loss of energy expectation (LOEE). The LOLE is the average number of days or hours per year in which the system load is expected to exceed the available generation capacity. And the LOEE index is the average annual energy expected not to be supplied due to the capacity shortages.

The probabilistic approach is either analytical or simulation-based. The analytical methods are more popular among planners and designers due to relatively shorter computational time. They represent the GSA problem through a mathematical model and calculate from it the reliability indices by using direct numerical solution. Analytical modeling however requires certain simplifications which in case of complex systems and complex operating procedures can undermine the significance of the final results. In such situations the simulation (Monte Carlo) technique becomes more advantageous for GSA evaluation.

Despite inherently high computational cost the Monte Carlo methods have gained increased interest among the reliability research community with the advances in the underlying theory and computer technology. The methods determine the reliability indices by simulating the random behavior of the system

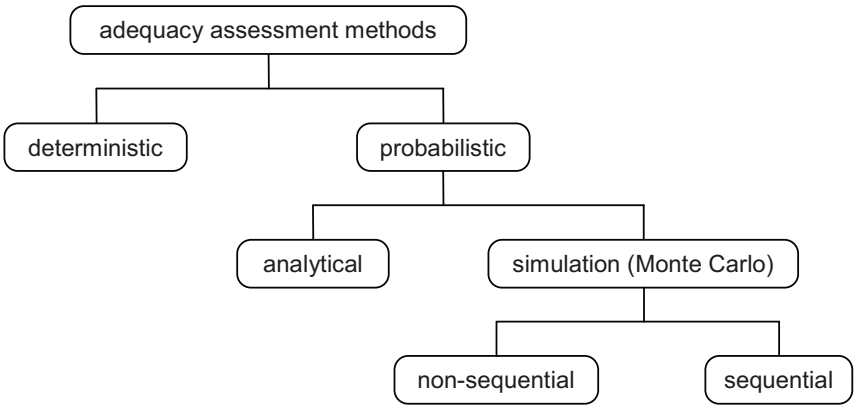

Figure 1.2: Classification of GSA evaluation methods

and its elements for a long period of time. This technique allows taking into account most of the relevant aspects and contingencies, such as generation unit outages (forced and planned) and repairs, variations in the load and renewable production, and operating policies [4, 16, 44], which provides a very detailed description and understanding of the system adequacy.

In the Monte Carlo simulations the random sampling of the system component states can be sequential (state-duration sampling) or non-sequential (state-sampling) depending on whether the history of the events is to be considered or not. The sequential Monte Carlo (SMC) approach, the focus of this thesis, in its simplest form involves superimposition of the time series of the available thermal generation capacity and the net (residual) consumption, i. e. system load minus intermittent production. The SMC method achieves higher accuracy, but at the expense of the increased calculation time [19]. The accuracy gain is expected to be significant for GSA studies of the systems with high share of time-dependent power sources such as renewables and energy storage [106]. Another important advantage of the SMC technique is possibility to combine adequacy and security analyses by incorporating the unit commitment and other operational details [84, 92].

Selection of the suitable GSA evaluation approach represents a trade-off between the precision and computational effort and depends on the objectives and requirements of the study. In case of conventional or moderately evolved power systems analytical probabilistic methods are the most appropriate [128]. And for the reliability assessment of future power systems with high share of variable generation and thus more dynamic operating conditions, the SMC simulations would be preferred.

1.2 SOLAR POWER

Concerns over global climate change and fossil fuel scarcity drive industrialized nations towards renewable energy, and particularly solar energy. Abundance of sunlight and continuous technological developments allow contemplating solar power as a major contributor in future electricity supply [65]. For example, by 2050 solar energy is estimated to provide 27% of the total and 34% of renewable electricity in the world [66, 67].

Two main technologies for solar electricity are photovoltaics (PV) and concentrated solar power (CSP). As shown in Table 1.1, the penetration of both technologies is expected to increase drastically in future with the faster growth and the larger share attributed to PV systems. The CSP global production may remain 'invisible' in the coming decade despite the notable contribution from Spain. The distinct prospects for PV and CSP electricity are explained by inherent differences between the two technologies.

	2013	2020	2050
World [66, 67]	135/3.6	400/11	4670/980
Spain [64, 126]	4.4/2.3	7.3/4.8	–

Table 1.1: Current and projected future PV/CSP capacities in GW

PV technology [67, 125, 135]

The core element of PV system is a solar cell – a semiconducting device exhibiting the photovoltaic effect (Fig. 1.3). The traditional PV cell technology uses single- (c-Si) or multi-crystalline (mc-Si) silicon and constitutes 85-90% of the current PV market. The remaining share is taken by more economical, but less efficient thin film solar cells which can deploy copper indium gallium selenide (CIGS), cadmium telluride (CdTe) or amorphous silicon (a-Si). The best research cell efficiencies[1] for silicon and thin film technologies exceed 25% and 20%, respectively.

To obtain higher performance a number of approaches are available, such as: tandem cells, impurity-band and intermediate-band devices, hot-electron extraction, and carrier multiplication. As a result of the increased manufacturing costs, however, these methods can be economically viable only in combination with solar concentration which allows reaching the cell efficiencies over 40%.

Ultra-high performances above 80% are hoped to be achieved by the so-called third-generation PV cells based on future advances in nanotechnology. Among the novel design concepts that are being considered are quantum wells, quantum dots and rectenna conversion. It is interesting to note that in case of successful development the third-generation PV cells would make CSP irrelevant.

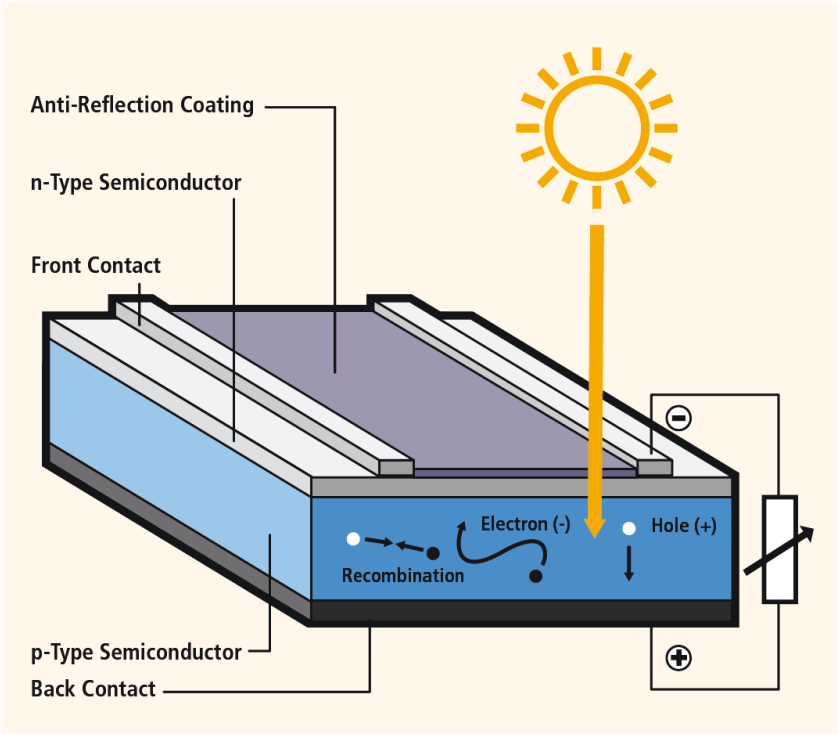

Figure 1.3: Generic schematic cross-section illustrating the operation of an illuminated solar cell [8]

1 The final output of PV system can be reduced further by up to 20% as a result of light absorption losses, cell mismatch, inverter inefficiency, wiring, and other parasitic power losses.

Despite the currently low energy efficiencies the advantage of PV technology is that it uses both beam and diffuse solar radiation. Direct conversion of sunlight to electricity also simplifies overall power production system and its operation.

The expansion of the technology, however, might be limited due to potential shortage in the supply of feedstock materials, particularly silicon. Another drawback is the inherent complexity of the solar cell manufacturing process which besides the increased costs also attributes to high lifecycle CO_2 emission levels of PV system compared to other renewable sources.

CSP technology [13, 66, 134]

CSP system uses mirrors with single or double axis tracking to redirect, focus and collect sunlight as a heat, that is subsequently converted to electricity based on a thermodynamic power cycle. The collected thermal energy is normally passed to the working fluid of the cycle (e. g. steam, air) through intermediate heat transfer fluid (HTF), consisting of certain type of synthetic oil. The overall system performance depends significantly on its optical efficiency and achieved solar concentration ratio. The latter is of importance because it determines the operating temperatures and thus performance of the power cycle.

The main four CSP technologies are parabolic trough, linear Fresnel, solar tower and parabolic (Stirling) dish, which basically refer to different solar concentration approaches. The primary characteristics of these technologies are summarized in Fig. 1.4 and Table 1.2.

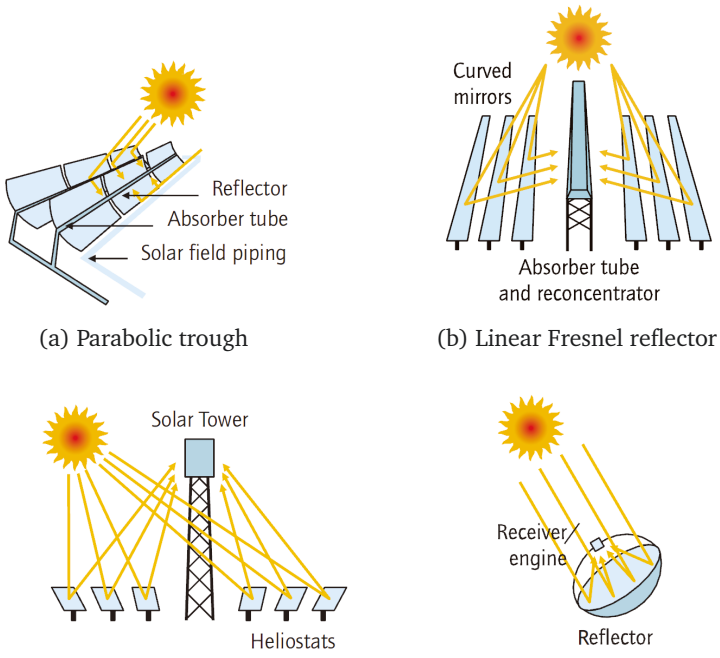

(a) Parabolic trough

(b) Linear Fresnel reflector

(c) Central tower

(d) Parabolic dish

Figure 1.4: Schematic showing the basic operation of a solar power system [66]

Parabolic troughs, currently, are the most common solar concentrators. They consist of long rows of parabolic reflectors with receiver (heat absorber) tubes mounted along the reflector's focal line. The typical tracking orientations of parabolic troughs are East-West and North-South, which allow maximizing solar radiation collection during the year and summer, respectively. Parabolic trough based CSP plants operate on the conventional Rankine (steam turbine) cycle.

Linear Fresnel reflectors approximate the parabolic reflectors by using long rows of flat or slightly curved mirrors positioned below a linear fixed receiver. Such simple design requires lower investments costs, but with the penalty in efficiency compared to the trough technology.

Solar towers, also known as central receiver systems, use thousands of heliostats – sun-tracking flat or slightly curved mirrors – to focus sunlight on a central receiver at the top of a fixed tower. Relatively higher solar concentration ratios and therefore higher operating temperatures in this case increase the Rankine cycle efficiency and also allow deploying the Brayton (gas turbine) cycle instead. The tower technology is approaching commercial maturity and has high development potential.

And finally, parabolic dishes track the sun and concentrate solar radiation at a focal point of the dish. The inherent technical characteristics of dishes makes them suitable for more advanced Stirling power cycle. This design is the most expensive, but also the most efficient and with the lowest environmental impact.

Compared to photovoltaics, CSP technology has modular and scalable components and does not require any exotic materials. The use of heat in the energy conversion chain allows aggregation of back-up fossil fuel burners (plant hybridization) and thermal energy storage, which, in turn, can significantly improve the production flexibility and firm the plant capacity, i. e. reduce intermittency of the supply.

And yet, CSP systems operate only with direct (beam) solar radiation, which limits their application to the regions with relatively high number of clear sky days. Typically, CSP plants become economically viable with the average annual beam solar radiation levels over 2000 kWh/m^2.

	Trough	Fresnel	Tower	Dish
Total efficiency [%]	15–16	8–10	12–20	20–25
Water use	high	high	medium	none
Land occupancy	large	medium	medium	small
Tech. maturity	very mature	mature	most recent	recent
Cost	low	very low	high	very high
Oper. temper. [°C]	50–400	50–300	300–2000	150–1500
Concentr. ratio [sun]	15–45	10–40	150–1500	100–1000
Tracking	one-axis	one-axis	two-axis	two-axis

Table 1.2: Comparison of CSP technologies [13, 66, 134]

Another disadvantage is related to the fact that the most suitable locations are usually found in semi-arid and hot regions that lack water resources and tend to be distant from the main electricity consumption points. Among the solutions being considered to deal with these issues are reduction of the water requirements of the plant by using dry cooling and application of high-voltage direct current power transmission systems.

1.3 ENERGY STORAGE

As noted earlier, renewable, and particularly, solar energy represents an effective approach to reduce dependence of humankind on fossil fuels and mitigate climate change. The primary obstacle to large-scale deployment of renewables is their inherent intermittency, which is exhibited through uncertainty and variability of the supply. To deal with these two negative aspects of renewable energy sources (RES), power systems require back-up generation capacity and operational flexibility[2]. The former guarantees that electricity is supplied to the consumers even on days with no wind and overcast sky, whereas the latter assures that the system facilities are capable to follow the changes in the net load, i. e. the total load minus renewable production [36, 97].

Technically, it is possible to have a power system with large penetration of RES that are firmed by reasonably flexible thermal generation plants. However, such system design might not be economically efficient, because it would lead to low utilization of the conventional power plants and also to notable spillage of renewable energy considering inevitable limitations in the operational flexibility. A natural solution in this case is considered to be utility-scale energy storage, which could level the net load variations and thereby reduce the renewable energy curtailments and the back-up generation requirements.

Currently, the global electricity storage capacity exceeds 140 GW, of which 99% corresponds to pumped hydro and 1% – to compressed air and electrochemical storage. The future expansion of energy storage systems is uncertain and depends on the economic and technological advances. According to the development scenarios in [68] the 2050 target for Europe, the US, China and India is estimated to be 310 GW. In Spain the existing planning includes only pumped hydro (as expected) and aims to increase the available storage capacity of 5.4 GW up to 8.8 GW by 2020 [64, 126].

Pumped hydro and compressed air storage technology [68, 136]

Energy storage technologies and their power applications are numerous. At present, the most suitable technologies that allow high storage unit capacities (>10 MW) and discharge times (>1 hour) are pumped hydro and compressed air energy storage (CAES).

Pumped hydro systems store electricity as potential energy of water. As shown in Fig. 1.5a, they use two reservoirs at different elevations, hydraulic pump and hydraulic turbine. During off-peak periods water is pumped from

2 The main requirements for flexible generation units are short start-up times, fast ramping capabilities, efficient partial load operation and high cycling durability.

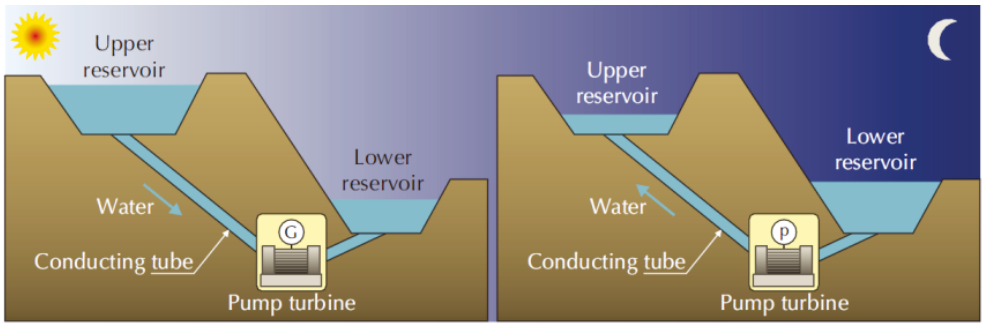

(a)

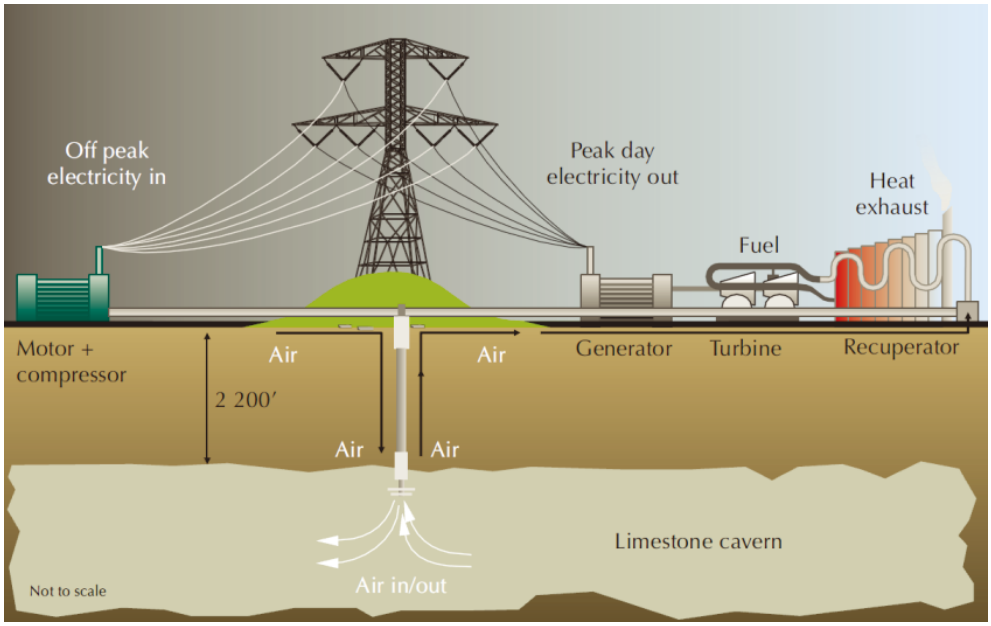

(b)

Figure 1.5: Schemes of (a) pumped hydro and (b) compressed air energy storage [65]

the lower reservoir to the upper. And when needed water is discharged back to the lower reservoir to produce electricity as in a conventional hydropower plant. The round-trip efficiency in this case can vary in the range of 50–85%.

Pumped hydro is the most mature and economical technology. Its deployment, however, is not always possible or preferred due to the lack of suitable sites, limited water availability and relatively high environmental impact (water and land footprint).

CAES systems, on the other hand, use electricity to compress air and store it in underground cavern (Fig. 1.5b). During peak periods the compressed air is released to an expansion turbine to generate electricity. To compensate for the heat loss in case of diabatic compression or to boost the power output the air can be heated through a combustor before entering the turbine. The round-trip efficiency of CAES is in the range of 27–70%.

The main advantage of CAES is that it allows large energy and power capacity at a reasonable cost. And yet, the technology is constrained by the availability of geological formations suitable for storing compressed air. Another drawback is the reliance of the existing CAES designs on gas burners.

CAES technology is approaching maturity, though its share is still negligible compared to pumped hydro. The current global installed capacity is only 440 MW and it is primarily concentrated in Germany and the US.

1.4 THESIS OBJECTIVES AND STRUCTURE

Thesis objectives

Solar power and energy storage are expected to have a large contribution in future electricity supply and therefore a significant impact on generation system adequacy. This naturally creates the need for their inclusion into GSA studies. The most effective and precise approach for performing such analyses, particularly in the presence of time-dependent power sources and complex operating policies, is the sequential Monte Carlo technique, which analyzes GSA by superimposing the time series of the available generation capacity and the net consumption.

Considering this, the general objective of the present thesis is to develop new or adapt existing models for creating chronological series of power production/consumption from solar power and energy storage plants that would allow incorporating the given power sources into generation system adequacy assessment based on the sequential Monte Carlo simulations. The final models have to be reasonably simplified to reduce the overall calculation time. The simplification also concerns the minimization of the required specific knowledge and input data which enables power system planner to evaluate the impact of the given power sources without substantial expertise in their underlying physics and by focusing on the key design parameters.

To achieve the goal of the thesis the following specific tasks are set:

1. to develop a solar radiation model that allows generating hourly synthetic time series of diffuse and beam solar radiation for single or multiple locations

2. to develop solar power plant models that allow translating solar radiation to the corresponding power production. The selected types of the plants are photovoltaics and concentrated solar power based on parabolic trough and central tower technology.

3. to develop a general energy storage dispatch model taking into account inherent characteristics of GSA study. The work focuses on energy storage dispatch because it represents the main difficulty when integrating energy storage into GSA evaluation.

4. to perform a GSA analysis of the power system in peninsular Spain by using the sequential Monte Carlo simulations. The given case study is intended to demonstrate the developed models and to evaluate the adequacy impact of time-dependent sources, such as solar power and energy storage, in real power system.

Thesis structure

The thesis content is organized into six parts. Part I provides general background and motivation for the work, and introduces the basics of generation adequacy assessment using the sequential Monte Carlo simulations and the basics of solar energy calculations. Part II, dedicated to stochastic modeling of solar radiation, describes a developed single-site solar radiation model and its extension for multiple locations incorporating spatial correlation. Part III focuses on solar power plant modeling and presents alternative models of PV and CSP (trough and tower) systems. Part IV addresses energy storage dispatch modeling in simulation-based reliability evaluations and proposes a new general methodology. Part V demonstrates the developed models through a case study of generation system adequacy in peninsular Spain. And finally, Part VI summarizes the main conclusions and future work.

One should note that the structure of this thesis does not follow a traditional layout. Considering multidisciplinary nature of the research questions, Parts II, III and IV are designed to be freestanding with their own sections for literature review, objectives, methods and conclusions.

2 BASICS OF GENERATION ADEQUACY ASSESSMENT

This chapter introduces the selected basic definitions and procedures related to generation system adequacy (GSA) assessment. They will be used in Parts IV and V of the thesis.

2.1 EVALUATION OF GENERATION SYSTEM ADEQUACY BASED ON SEQUENTIAL MONTE CARLO SIMULATIONS

As noted earlier, probabilistic GSA study aims to estimate the reliability indices, such as loss of load expectation (LOLE), loss of energy expectation (LOEE) and loss of load frequency (LOLF). For a conventional single-area generation system comprising only thermal (dispatchable) power units GSA evaluation based on the sequential Monte Carlo (SMC) method is performed in the following three steps [16]:

1. The chronological hourly series of the total load and available generation capacity are obtained. The load sequence is usually created by taking the historical data segment for one or several years and repeating it until the required full length is achieved. And the curve of the available system capacity is obtained by combining the operating cycles of individual power units, which, in turn, are created through random sampling of the unit failure and repair time periods as shown in Fig. 2.1a. The simplest approach to simulate the generation unit operating cycle is to approximate it as a two-state stochastic (Markov) process in which both up and down state durations are exponentially distributed and therefore can be estimated as:

   $$\text{Time to failure (repair)} = -\text{Mean time to failure (repair)} \times \ln r \quad (2.1)$$

   where r is the uniformly distributed random number from 0 to 1.

2. The time series of the system load and available capacity are superimposed to detect the periods with the capacity shortages as demonstrated in Fig. 2.1b.

3. And finally, the reliability indices are calculated as:

$$\text{LOLE} = \frac{1}{N_Y} \sum_{i=1}^{N_Y} \text{LLD}_i \quad (2.2)$$

$$\text{LOEE} = \frac{1}{N_Y} \sum_{i=1}^{N_Y} \text{ENS}_i \quad (2.3)$$

$$\text{LOLF} = \frac{1}{N_Y} \sum_{i=1}^{N_Y} \text{LLO}_i \quad (2.4)$$

where N_Y is the number of simulated years; LLD is the annual loss of load duration – the number of hours when the system load exceeds the available generation capacity; LLO is the annual loss of load occurrence – the number of times when the capacity shortage takes place; and ENS is the annual energy not supplied – the amount of electricity demand that cannot be met due to the capacity shortages (Fig. 2.1b).

The estimated this way reliability indices approach to their 'real' values, as the number of sampling years increases. Considering fluctuating nature of the convergence process, the minimum value of N_Y is chosen based on the maximum allowed variation level of the indices, particularly LOEE, which is the slowest to converge. Typically, the required number of simulation years is up to several thousands and it increases even further for highly reliable generation systems. This explains the significant computational cost of the SMC technique.

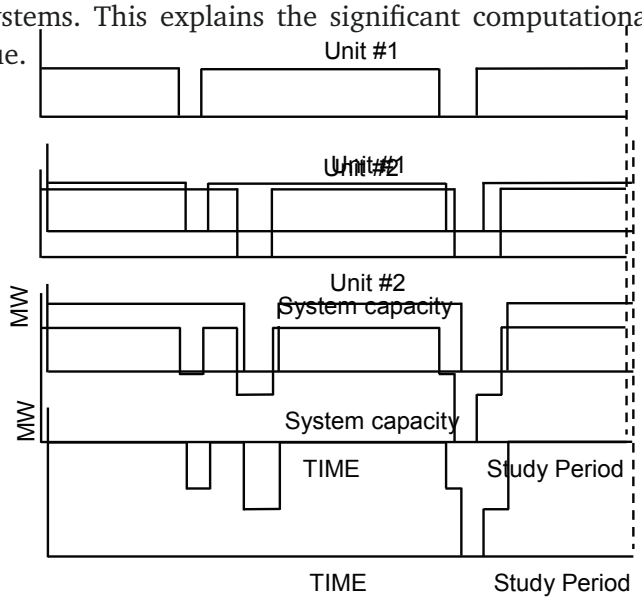

(a)

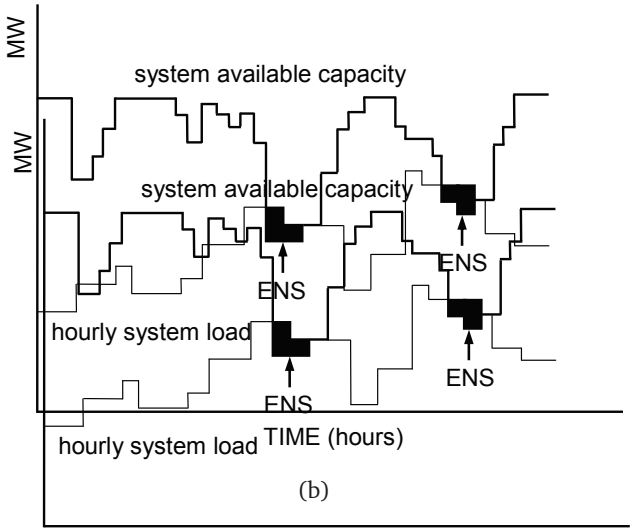

(b)

Figure 2.1: Generation of the available capacity series (a) and its superimposition with the system load curve (b) based on [16]

In the presence of time-dependent power sources, such as renewables and energy storage, the described GSA assessment procedure has to be adapted. In case of renewable production the procedure would require the corresponding chronological hourly series and the substitution of the load by the residual (net) load, i. e. the system load minus renewable generation. Incorporation of energy storage into GSA study, however, is not straightforward and it is the focus of Part IV of the thesis.

2.2 ESTIMATION OF CAPACITY CREDIT OF INTERMITTENT GENERATION

A common objective of GSA analysis is to evaluate the contribution of various time-dependent power sources to the overall system reliability. This contribution, usually referred to as the capacity credit or capacity value, basically represents the equivalent capacity of the conventional plant that could be displaced or the equivalent load increase that could be applied by incorporating a given intermittent source while maintaining the system adequacy at the same level.

There are numerous methods for the capacity credit estimations as described in [7, 106]. The most popular approach is to deploy the effective load carrying capability (ELCC) as the metric. The given technique, initially proposed by Garver [53], can be implemented in various forms. In this work the preference is given to the ELCC procedure from [75], which comprises the following two steps:

1. GSA assessment of the initial system configuration, i. e. without a given time-dependent power source. If desired, the load can be adjusted to match the reliability level to the target value expressed in terms of LOLE or LOEE index. The load adjustment is an iterative process which involves at each run the increase or reduction of the load time series by a constant across all hours and recalculation of the reliability indices.

2. GSA assessment of the modified system configuration, i. e. with the given intermittent source. The estimated reliability level in this case, of course, will be higher. To match it to the initial value (from Step 1), the load time series is adjusted through iterations. Once the matching process is completed, the ELCC value for the selected time-dependent power source is determined as

$$\mathrm{ELCC} = \Delta \mathrm{L}_{\mathrm{sys}}^{\mathrm{II}} - \Delta \mathrm{L}_{\mathrm{sys}}^{\mathrm{I}}, \tag{2.5}$$

   where $\Delta \mathrm{L}_{\mathrm{sys}}^{\mathrm{I}}$ and $\Delta \mathrm{L}_{\mathrm{sys}}^{\mathrm{II}}$ are the final adjustments applied to the load time series in the initial and modified system configurations, respectively. If the load is increased, $\Delta \mathrm{L}_{\mathrm{sys}}$ is considered positive.

One should note that it is common to express the capacity credit of intermittent power source in relative terms. This requires simply the division of the ELCC value from (2.5) by the nominal capacity of a given source.

3 BASICS OF SOLAR ENERGY CALCULATIONS

This chapter introduces the basic parameters and concepts required for calculations of the Sun position and energy based on [41, 72, 144]. The given definitions will be used in Parts II and III of the thesis.

The adopted units for simulation interval and angles are hours and degrees, respectively. The assumed sign convention for latitude ϕ and longitude λ is: North/West – positive and South/East – negative.

3.1 TIME RECKONING

Solar energy calculations usually use apparent solar time (AST), which is based on the apparent angular motion of the sun. The conversion between AST and local standard time (LST) requires two corrections. The first is the equation of time (EOT) estimated as:

$$\mathrm{EOT} = (9.87 \sin 2\mathrm{d}' - 7.53 \cos \mathrm{d}' - 1.5 \sin \mathrm{d}')/60, \tag{3.1}$$

where $\mathrm{d}' = (\mathrm{d}-1)360/364$ and d is the day of the year.

The second correction takes into account the difference between the standard and local longitudes $\Delta\lambda$ leading to the following final expression for AST:

$$\mathrm{AST} = \mathrm{LST} + \mathrm{EOT} + \Delta\lambda/15 \tag{3.2}$$

Time convention

In this work solar energy calculations employ hourly basis as in the majority of the existing tools for solar energy modeling.

The time convention for solar radiation or other 'cumulative' parameter is the same as in TMY2 and TMY3 weather file formats, i. e. the solar radiation for the given time stamp represent the total energy received during the 60 minutes preceding the indicated hour in the local standard time. For example, the radiation value for hour 1 represents the total radiation received between midnight and 1:00 am of the first hour of the year. It is assumed that one year consists of 8760 hours (365 days).

In case of solar angles, the primary 'non-cumulative' variables, the calculations are done at the middle of the hour (at 30 minutes past the hour) and applied to the entire hour as in [109].

For the sunrise hour, the sun position is at the midpoint between sunrise time and the end of the timestep. Similarly, for the sunset hour, the sun position is the midpoint between the beginning of the timestep and sunset time.

3.2 SOLAR ANGLES

The calculations of the main solar angles as defined in Fig. 3.1 are explained below.

Solar declination δ is the angle between the sun rays and the equatorial plane defined mainly by the day of the year d

$$\delta = 23.45 \sin\left(360\,\frac{d+284}{365}\right) \tag{3.3}$$

Solar hour angle ω is the angle between the local meridian and the meridian plane containing the sun

$$\omega = 15\,(\mathrm{AST} - 12) \tag{3.4}$$

Its value at sunset (sunrise) is estimated as

$$\cos\omega_{ss} = -\tan\phi\tan\delta \tag{3.5}$$

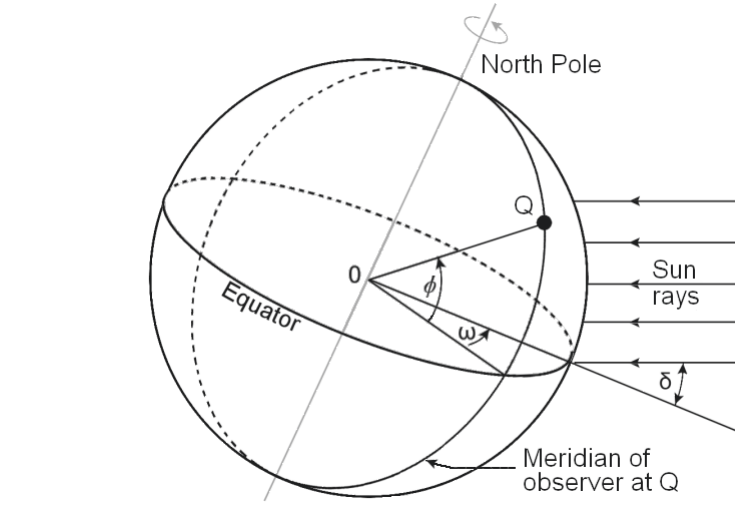

(a)

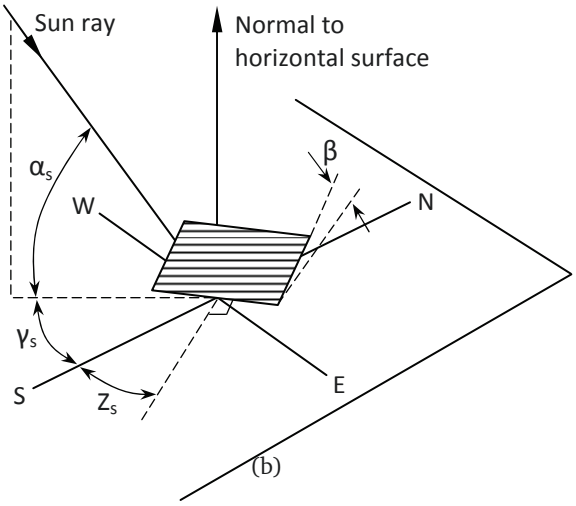

(b)

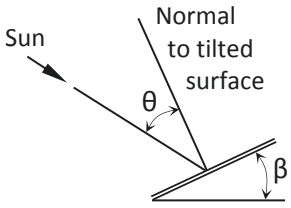

(c)

Figure 3.1: Solar angles (based on [41, 144])

Combination of equations (3.2), (3.4) and (3.5) allows calculating the local times of sunset and sunrise

$$\begin{cases} T_{rise} = 12 - EOT - (\Delta\lambda + \omega_{ss})/15 \\ T_{set} = 12 - EOT - (\Delta\lambda - \omega_{ss})/15, \end{cases} \tag{3.6}$$

which, in turn, are used to determine the equivalent LST values for the given hourly interval h according to the adopted time convention

$$LST_h = \begin{cases} (T_{rise} + h)/2 & \text{if } h = \text{sunrise time interval} \\ (T_{set} + h - 1)/2 & \text{if } h = \text{sunset time interval} \\ h - 0.5 & \text{if sunrise} < h < \text{sunset} \end{cases} \tag{3.7}$$

Solar altitude angle α_s is the angle between the sun rays and a horizontal plane (i. e. complementary of the zenith angle)

$$\sin\alpha_s = \cos\omega\cos\delta\cos\phi + \sin\delta\sin\phi \tag{3.8}$$

Solar azimuth angle γ_s is the horizontal angle between the sun rays and due south (north) for the Northern (Southern) Hemisphere with the values eastward designated as positive

$$\gamma_s = \text{sgn}(\omega)\left|\cos^{-1}\left(\frac{\sin\alpha_s\sin\phi - \sin\delta}{\cos\alpha_s\cos\phi}\right)\right| \tag{3.9}$$

Solar incidence angle θ is the angle between the sun rays and the normal on a surface, which for stationary plane is defined as

$$\begin{aligned} \cos\theta = {} & \sin\phi\sin\delta\cos\beta - \cos\phi\sin\delta\sin\beta\cos Z_s \\ & + \cos\phi\cos\delta\cos\omega\cos\beta + \sin\phi\cos\delta\cos\omega\sin\beta\cos Z_s \\ & + \cos\delta\sin\omega\sin\beta\sin Z_s \end{aligned} \tag{3.10}$$

where β is the plane slope (tilt) angle and Z_s is the surface azimuth angle. In case of employing the sun tracking mechanisms the expression is simplified. For example:

at dual axis tracking[1]

$$\cos\theta = 1, \quad \beta = 90 - \alpha_s, \quad Z_s = \gamma_s \tag{3.11}$$

at East-West tracking with horizontal North-South axis

$$\cos\theta = \sqrt{\sin^2\alpha_s + \cos^2\delta\sin^2\omega} \tag{3.12}$$

$$Z_s = \begin{cases} 90^\circ & \text{if } \gamma_s > 0 \\ -90^\circ & \text{if } \gamma_s \leqslant 0 \end{cases} \tag{3.13}$$

$$\tan\beta = \tan(90 - \alpha_s)\,|\cos(Z_s - \gamma_s)| \tag{3.14}$$

1 In central tower systems full tracking is used to project the sun rays on the central receiver and incidence angle among other parameters depends also on the heliostat position in the solar field. The incidence angle in this case is defined by (9.7).

3.3 SOLAR RADIATION

Solar radiation is the energy of the electromagnetic waves emitted by the Sun during certain period of time. In this work when not specified otherwise, the hourly solar radiation is equivalent to the average solar irradiance (rate of solar energy).

Extraterrestrial radiation is the solar radiation at the top of the earth's atmosphere. In normal direction it is equal to

$$G_{o,n} = 1366 \left(1 + 0.033 \cos \frac{360\,d}{365}\right) \tag{3.15}$$

On a horizontal plane daily and hourly values of extraterrestrial radiation are estimated as:

$$H_o = 24 G_{o,n} \left(\frac{1}{\pi} \sin\omega_{ss} \cos\delta \cos\phi + \frac{\omega_{ss}}{180} \sin\delta \sin\phi\right), \tag{3.16}$$

$$I_o = 12 G_{o,n} \left(\frac{1}{\pi}(\sin\omega_2 - \sin\omega_1) \cos\delta \cos\phi + \frac{\omega_2 - \omega_1}{180} \sin\delta \sin\phi\right), \tag{3.17}$$

where ω_1 and ω_2 are the solar hour angles at the start and end of the hour. For sunrise and sunset time intervals one of the boundaries is defined by ω_{ss}.

Terrestrial radiation, i. e. amount of solar radiation reaching the earth surface, is reduced by the effects of atmospheric absorption and scattering. The latter is also responsible for splitting of terrestrial radiation into beam I_b and diffuse I_d components.

The ratio of terrestrial to extraterrestrial radiation on a horizontal plane is referred to as the *clearness index*. Its monthly, daily and hourly values are defined as:

$$KT_{month} = \frac{\sum H_{tot,i}}{\sum H_{o,i}}, \quad i \text{ - day of the month} \tag{3.18}$$

$$KT_{day} = \frac{H}{H_o} = \frac{\sum I_{tot,i}}{\sum I_{o,i}}, \quad i \text{ - hour of the day} \tag{3.19}$$

$$KT_{hour} = \frac{I_{tot}}{I_o} \tag{3.20}$$

Based on these equations the individual clearness indices can be related as follows:

$$KT_{month} = \frac{\sum \left(H_{o,i}\, KT_{day,i}\right)}{\sum H_{o,i}}, \quad i \text{ - day of the month} \tag{3.21}$$

$$KT_{day} = \frac{\sum \left(I_{o,i}\, KT_{hour,i}\right)}{\sum I_{o,i}}, \quad i \text{ - hour of the day} \tag{3.22}$$

Traditionally, the clearness index has been an important dimensionless parameter in solar radiation modeling and served as the main variable in classical empirical relations and stochastic algorithms. Its alternative, the clear-sky index, which seems to be preferred in recent studies [10], is obtained by dividing the terrestrial solar radiation on a horizontal plane to the corresponding value at clear-sky conditions.

Part II

SOLAR RADIATION MODELING

4 INTRODUCTION

Solar radiation model proposed in Part II of the thesis is used for stochastic generation of the synthetic solar radiation values, which then serve as input for solar power plant models. The power production series obtained from the latter subsequently can be used for power system studies, particularly for generation system adequacy assessments based on the sequential Monte Carlo simulations.

4.1 LITERATURE REVIEW

4.1.1 *Stochastic algorithms*

It is a common practice to use synthetic solar radiation data when meteorological measurements for a certain location or timescale are unavailable or unreliable. The synthetic data in this case can be generated by multivariate or univariate statistical model. The former, also known as the weather generator, creates the radiation sequence (usually on a daily basis) together with other weather parameters. The existing types of weather generators are described in [161]. The classical version, developed by Richardson [129], involves, first, synthesis of daily precipitation time series by using a Markov chain-exponential model, and then generation of maximum/minimum temperature and solar radiation sequences by treating these variables as multivariate stochastic process conditioned on the wet or dry state of the day.

The univariate model, on the other hand, creates only the values of solar radiation based on simple inputs, typically comprising the long-term statistics for the clearness index KT [10]. The well-known Aguiar [2, 3] and Graham [56, 57] algorithms for daily and hourly timescales employ Markov transition matrix or autoregressive moving average based techniques by assuming that: (a) second- and higher order autocorrelation effects are negligible, and (b) for any location and season the probability distribution of KT is dependent only on its average value. In direct or adapted form the Aguiar and Graham models are implemented in the software tools Meteonorm [94] and Watgen [159], respectively. The synthesis at a monthly timescale is less common, though less complex. For example, with the Bohlen [22] and Tiba [148] approaches the individual monthly clearness index values are created by adding Gaussian noise to the long-term average, where the standard deviation is determined based on a simple empirical relation. The Tiba model in general form also includes the autocorrelation coefficient with lag 1. When the long-term statistics for solar radiation is not available, the synthetic data can be created by alternative techniques using the observed or simulated cloud coverage [42].

Despite high performance the traditional stochastic algorithms are intended for single-site data generation. Their adaptation for the case of multiple locations requires incorporation of the spatial correlation of solar radiation (SCSR), which is not straightforward. The review of the recent literature indicates that there have not been any successful attempts to integrate SCSR into univariate solar radiation models. Yet, a number of methods for multivariate algorithms have been proposed. The effective and relatively simple approach in this case seems to be not to change the conventional single-site weather generator, but to modify the input random number streams instead, for the given network of locations so that the resultant synthetic values of solar radiation (or other weather parameter) have realistic spatial correlations [76, 160]. Even though this technique allows adequate reproduction of SCSR, it still requires synchronized regional meteorological measurements for tuning the model coefficients, which, to some extent, defeats the purpose of using the synthetic data.

Apparently, there are no known methods for multisite generation of solar radiation data from reduced (easily available) inputs. This might be explained by the absence of general formal description of SCSR that could allow estimating the spatial correlation for any two locations based on simple predictor variables. Obviously, at short timescales (up to several hours), since local weather factors become significant, such a general characterization of SCSR is unrealistic. However, at long timescales the author believes that this is possible. Interestingly, the literature reveals few research papers addressing this subject. For example, [1, 147] estimate the coefficients of variability (the standard deviation of the intersite daily radiation differences divided by the mean values) for the selected station pairs by using directly the measured daily solar radiation values. And in recent studies, [11, 62] evaluate SCSR by Pearson's correlation coefficient and represent the solar resource via ramp rates (deltas) of the clear-sky index, which is more suitable for such analyses [10]. The paper [62] is of particular interest as it employs satellite-derived data covering over 70,000 pairs of points, though the considered timescales are only up to 4 hours. The common shortcoming of the existing studies is that they try to relate SCSR to the intersite distance only, whereas the results clearly show that this dependence changes from one region to the other.

4.1.2 *Diffuse solar radiation models*

The global solar radiation values generated by stochastic algorithms have to be split into diffuse and beam (direct) components. This is typically done by using empirical correlations linking the diffuse or beam solar fraction to the hourly clearness index and other optional parameters. The most common correlations are reviewed and compared in [32, 69, 70, 117, 122].

Among the traditional diffuse (beam) solar radiation models are Erbs [47], Skartveit [141] and Perez [118] approximations, which differ in complexity, particularly in the predictor variable selection. Erbs uses the clearness index as the only input; Skartveit incorporates the solar zenith angle as an additional predictor; whereas Perez chooses the solar zenith angle, the stability index reflecting the KT dynamics and the precipitable water as extra parameters.

A recent development in the given area is the Boland-Ridley-Lauret (BRL) method [130], which as the Perez technique is based on multiple input variables and adopted in Meteonorm software. The BRL model is relatively easy to implement and according to [94, 149] achieves a similar accuracy as the 'best' Perez technique.

4.2 OBJECTIVES AND METHODOLOGY OF PART II

The objective of Part II of the thesis is to develop a solar radiation model (SRM) that allows generating hourly synthetic sequence of diffuse and beam solar radiation for single or multiple locations from easily available inputs. To achieve the research objective the following tasks are established:

1. to develop a single-site solar radiation model
2. to extend the model for multiple locations by incorporating the spatial correlation of solar radiation

The first task is accomplished by deploying the Bohlen and Aguiar univariate stochastic algorithms and the BRL diffuse radiation model. The calculation procedures are checked for possible improvements and the corresponding modifications are applied.

The second task is particularly challenging. It is centered around the hypothesis that at long timescales general and simple characterization of SCSR is possible; in other words, that mathematical expressions can be derived to quantify SCSR between any two locations by using a reduced set of information. The hypothesis is tested through a regression analysis of historical solar radiation series covering multiple geographical and climatic regions at monthly and daily timescales. Once empirical formulae for SCSR estimation are known, spatial correlation is incorporated to multisite generation of solar radiation by applying it to the random number streams that drive the stochastic algorithms.

The programming is done in Matlab. The single-site SRM is validated as an integrated tool by statistical comparison of the synthetic and typical meteorological year data for selected locations. The model performance in case of multiple sites is demonstrated by using the same historical solar radiation series that are used for the SCSR characterization.

5 SINGLE-SITE MODEL OF SOLAR RADIATION

5.1 GENERAL DESCRIPTION

A solar radiation model (SRM) is developed for generating synthetic values of the hourly total, beam (direct) and diffuse radiation on a horizontal plane at a given single location. SRM deploys the long established stochastic algorithms and other auxiliary models. The general calculation procedure is similar (but not identical) to that adopted in Meteonorm [94], and comprises the following steps:

1. Definition of the inputs – the long-term monthly average clearness index values $\widehat{\mathrm{KT}}_{month}$. The required data directly or indirectly can be obtained from various sources such as [102, 151].
2. Stochastic generation of the monthly clearness index KT_{month} time series based on the Bohlen approach [22]. The given step is optional and can be omitted when the interannual variations in the monthly solar radiation are of no interest.
3. Stochastic generation of the daily clearness index KT_{day} series by using the Aguiar algorithm for a daily timescale [3].
4. Stochastic generation of the hourly clearness index KT_{hour} sequence according to a time-dependent, autoregressive Gaussian (TAG) model from Aguiar [2].
5. And finally, calculation of the beam $\mathrm{I_b}$ and diffuse $\mathrm{I_d}$ radiation components based on the Boland-Ridley-Lauret (BRL) method [130].

The Bohlen model, implemented as in [22] with no adjustments, creates the monthly KT time series simply by adding Gaussian noise to the long-term average values. The model deploys an empirical linear relation to estimate the standard deviation of the interannual fluctuations of KT_{month} from the corresponding $\widehat{\mathrm{KT}}_{month}$ values.

The Aguiar algorithm for a daily timescale generates the KT_{day} series based on a library of the Markov transition matrices. The approach assumes that (a) daily radiation value is correlated only to that of the previous day, and (b) the form of the probability function for any given month is determined by the value of $\widehat{\mathrm{KT}}_{month}$. The involved calculations are according to the original paper [3]. To match the algorithm output to that of the Bohlen model, the following small modification is applied: the KT_{day} generation process for each month driven by $\widehat{\mathrm{KT}}_{month}$ is repeated until the resultant average is close to the corresponding KT_{month} from Step 2 and not to the $\widehat{\mathrm{KT}}_{month}$ value.

The TAG and BRL methods are adjusted based on the additional investigations as described below.

5.2 SYNTHESIS OF THE HOURLY CLEARNESS INDEX VALUES

The TAG model from Aguiar [2], selected in this work for creating synthetic hourly clearness index values, has certain general similarities with the other widely used approach by Graham [56]. The TAG method, however, uses computationally less expensive technique to ensure a good quality of the synthetic radiation data. To improve the effectiveness of SRM, two important modifications are applied to the TAG algorithm. The overall calculation procedure is as follows.

The hourly clearness index is split into trend (base) and random components:

$$KT_{hour} = KT_{base} + KT_{rand} \tag{5.1}$$

The trend part basically represents the average daily profile of clearness index for the given (target) value of KT_{day} and is estimated based on the empirical correlation:

$$KT_{base} = \upsilon_a + \upsilon_b \, e^{-\upsilon_c M_{air}}, \tag{5.2}$$

where M_{air} is the optical air mass (approximately equals to $1/\sin\alpha_s$ if the site altitude and the earth curvature are ignored), and υ_{a-c} are the coefficients calculated by using one of the sets of equations given below:

from Aguiar [2]

$$\begin{cases} \upsilon_a = -0.19 + 1.12 KT_{day} + 0.24 e^{-8 KT_{day}} \\ \upsilon_b = 0.32 - 1.60 (KT_{day} - 0.5)^2 \\ \upsilon_c = 0.19 + 2.27 KT_{day}^2 - 2.51 KT_{day}^3 \end{cases} \tag{5.3}$$

from Graham [56]

$$\begin{cases} \upsilon_a = KT_{day} - 1.167 KT_{day}^3 (1 - KT_{day}) \\ \upsilon_b = 0.979 (1 - KT_{day}) \\ \upsilon_c = 1.141 (1 - KT_{day}) / KT_{day} \end{cases} \tag{5.4}$$

In SRM the Graham definitions (5.4) are used (*the first modification*) as they seem to provide relatively smaller deviation of the average KT_{base} from the reference KT_{day} value (see Fig. 5.1).

The random component of the hourly clearness index is expressed as:

$$KT_{rand} = \sigma_k \, KT'_{rand} \tag{5.5}$$

The parameter σ_k is the standard deviation of KT_{hour} values for the given daily clearness index and KT'_{rand} is the normalized first order autoregressive function. These variables in the original paper [2] are defined as follows:

$$\begin{cases} \sigma_k = 0.14 \, e^{-20 (KT_{day} - 0.35)^2 + (3 (KT_{day} - 0.45)^2 + 16 KT_{day}^5)(1 - \sin\alpha_s)} \\ KT'_{rand,[h]} = \varphi_1 \, KT'_{rand,[h-1]} + \mathcal{N}(0, \sigma'_k) \\ \varphi_1 = 0.38 + 0.06 \cos(7.4 KT_{day} - 2.5) \end{cases} \tag{5.6}$$

where φ_1 is the autocorrelation coefficient, $\mathcal{N}(0, \sigma'_k)$ is the random Gaussian number with null average and standard deviation equal to $\sigma'_k = \sigma_k (1 - \varphi_1^2)^{0.5}$.

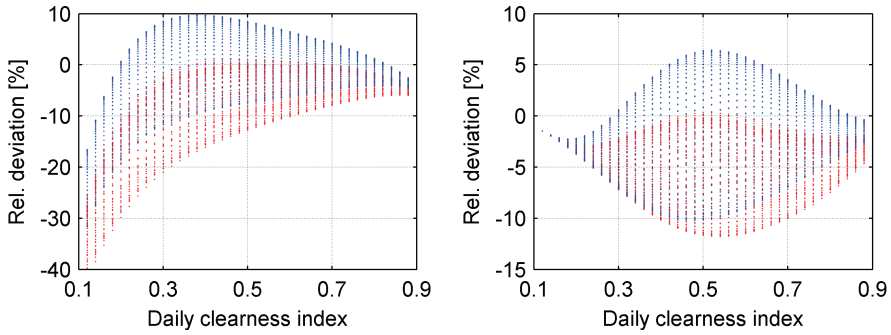

(a) (b)

Note: The deviations are calculated for each day of the year in Madrid in the following steps: (i) the actual/target daily clearness index KT_{day} is obtained from the typical meteorological year data, (ii) the corresponding daily profile of the base hourly clearness index KT_{base} is estimated by using (5.2) with the Aguiar (5.3) or Graham (5.4) definitions of the coefficients υ_{a-c}, (iii) the KT_{base} daily profile is averaged to obtain KT'_{day}, and (iv) the relative deviation between the calculated and target values of the daily clearness index is determined as $(KT'_{day} - KT_{day})/KT_{day}$. The results with simple algebraic averaging are shown in red and with the averaging based on (3.22) are presented in blue. The given example demonstrates that, overall, the Graham approximation and the adopted averaging approach provide higher precision.

Figure 5.1: Example of relative deviations in the calculated clearness index trend component when using the Aguiar (a) and Graham (b) approximations

In Meteonorm software, the TAG model has been adjusted based on recent validation studies and the following set of equations is used instead [94]:

$$\begin{cases} \sigma_k = 0.32\, e^{-50(KT_{day}-0.4)^2} + 0.002 \\ KT'_{rand,[h]} = 2\,\varphi_1\, KT'_{rand,[h-1]} + \mathcal{N}(0, \sigma'_k) \\ \varphi_1 = 0.148 + 2.356 KT_{day} - 5.195 KT^2_{day} + 3.758 KT^3_{day} \end{cases} \tag{5.7}$$

In this work the preference is also given to the revised set of formulas (5.7) which is *the second final modification* of the original Aguiar algorithm.

Thus, according to the adopted approach the hourly clearness index is determined using the equations: (5.1), (5.2), (5.4), (5.5) and (5.7). The calculations are performed only for the time intervals between sunrise and sunset. At each hour it is assured that KT_{hour} is positive and not larger than the clear-sky value, where the latter can be estimated, for example, as $0.88 \cos 0.4\omega$ [2]. Once the KT_{hour} sequence is created for the given day, its average $KT_{day,syn}$ is calculated based on expression (3.22) and compared with the target value KT_{day} as follows:

$$|KT_{day,syn} - KT_{day}|/KT_{day} \leqslant \text{Deviation limit} \tag{5.8}$$

If the deviation is larger than the allowed limit (say 5%), then the calculations are repeated. Otherwise, the generated daily profile of clearness index is simply scaled to match $KT_{day,syn}$ with KT_{day}. It is important to note that as the daily average of KT_{base} sequence can deviate from KT_{day} (see Fig. 5.1), the scaling is also applied to the trend component of the clearness index.

5.3 CALCULATION OF DIFFUSE AND BEAM SOLAR RADIATION

The generated time series of the hourly clearness index values is converted into that of the total radiation I_{tot} simply by using equation (3.20). The beam and diffuse radiation components are calculated based on the BRL model approximating the diffuse solar fraction as follows [130]:

$$\begin{cases} \dfrac{I_d}{I_{tot}} = (1+e^n)^{-1}, \\ n = 6.63KT_{hour} + 0.006AST - 0.007\alpha_s + 1.75KT_{day} + 1.31KT' - 5.38 \end{cases} \tag{5.9}$$

where AST is the apparent solar time, α_s is the solar altitude angle, KT' is the stability index characterizing the KT dynamics and is defined as:

$$KT'_{[h]} = \begin{cases} KT_{hour,[h+1]} & \text{if } h = \text{sunrise interval} \\ KT_{hour,[h-1]} & \text{if } h = \text{sunset interval} \\ 0.5\left(KT_{hour,[h-1]} + KT_{hour,[h+1]}\right) & \text{if sunrise} < h < \text{sunset} \end{cases} \tag{5.10}$$

Since the BRL formula as any other I_d/I_{tot} correlation is developed based on the weather data for multiple locations and by using only a limited number of predictors, it is natural to expect certain deviations when applying it for individual site. This is well demonstrated in Fig. 5.2 comparing the BRL model predictions with the typical meteorological year (TMY) data for Madrid and Geraldton.

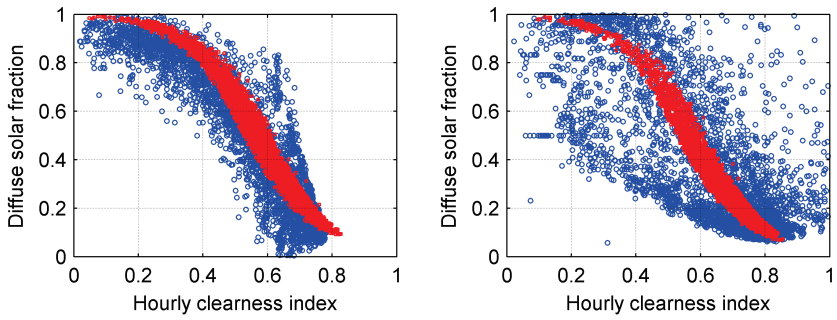

(a) Madrid (b) Geraldton

Figure 5.2: Comparison of the TMY data (blue) with the BRL model predictions (red)

To reduce the quantitative and qualitative discrepancy between the synthetic and actual beam radiation data, the BRL technique is implemented with two adjustments. First, an offset Δdf is added to the I_d/I_{tot} value calculated from (5.9) in order to match the annual average of the generated beam radiation values with the given input within tolerance of 1%. This is equivalent to shifting the points in Fig. 5.2 up ($\Delta df > 0$) or down ($\Delta df < 0$).

And second, at solar altitude angles less than 10° the diffuse solar fraction is assumed to be 0.75. The reason is that the BRL model like most others tend to significantly underestimate the diffuse fraction for the hours close to sunrise and sunset. This, in turn, is explained by the fact that solar radiation measurements used in developing I_d/I_{tot} correlations exclude the data approximately at $\alpha_s < 10°$ [70] and thus the effect of low solar altitude angles is ignored. The adopted diffuse fraction value of 0.75 represents a rough estimation based on the actual weather data in [141].

5.4 MODEL VALIDATION

SRM is validated as an integrated tool, assuming that the individual adopted methods perform adequately as described in the original references. The validation is done simply by statistical comparison of the synthetic data and TMY[1] for 8 selected locations.

The solar radiation time series is created for each site for the period of 30 years[2] using the monthly radiation values from the corresponding TMY files [151]. The calculation time per year on a workstation (Intel Xeon W3503, 12 GB RAM, 2.4 GHz) is approximately 0.24 seconds.

The simulated and actual solar radiation data are compared on an annual basis in Table 5.1. The variations in the monthly deviations of the beam normal radiation are presented in Fig. 5.3. Qualitative differences between the synthetic and reference time series of I_{tot} and $I_{b,n}$ are shown through cumulative distribution plots in Figs. 5.4 and 5.5.

According to the results, the annual average of the generated total radiation sequence matches ideally with the reference (input) data. Though not presented here, this holds true also for the monthly values of I_{tot}. In qualitative terms, the discrepancy between the synthetic and TMY values of total radiation is negligible as well.

In case of direct normal radiation, however, the quality of the synthetic data varies notably among the selected sites. The minimum, maximum and absolute mean monthly errors are –18.2%, +16.5% and 4.1%, respectively. Such relatively large deviations are not unexpected since the BRL correlation adopted in this work for calculating I_d/I_{tot} fraction is a simplified representation of the involved highly complex physical and chemical processes in the atmosphere.

Site	Annual deviation from TMY [%]			Δdf [-]
	Total	Beam normal	Diffuse	
Madrid	+0.3	–0.0 (–11.3)	+14.1 (+31.8)	–0.060
Seville	+0.3	–0.6 (–6.1)	+14.4 (+25.9)	–0.035
Phoenix	+0.2	+0.3 (+4.6)	+8.7 (–2.2)	+0.030
New Delhi	+0.1	+0.6	+9.9	0.0
Adelaide	–0.2	+0.8 (+7.7)	+12.1 (+3.2)	+0.035
Geraldton	–0.1	–0.5 (–1.4)	+16.6 (+18.7)	–0.005
Johannesburg	+0.1	+0.4 (+9.5)	+6.7 (–4.5)	+0.050
Antofagasta	–0.2	–0.1 (+7.2)	+21.5 (+8.6)	+0.040

Note: The values in brackets correspond to the deviations at $\Delta df = 0$.

Table 5.1: Evaluation of synthetic solar radiation data for selected sites

1 Though "typical" in TMY definition, strictly, is not equivalent to "mean", it is still reasonable to assume that TMY represents the average weather conditions for a given site.

2 This is the common time period adopted in generation of TMY.

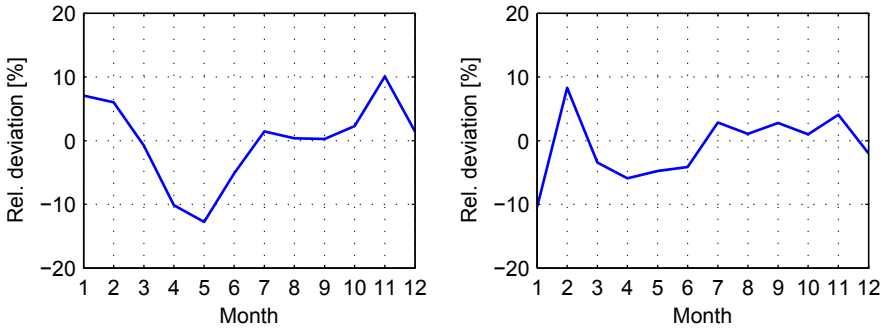

(a) Madrid

(b) Seville

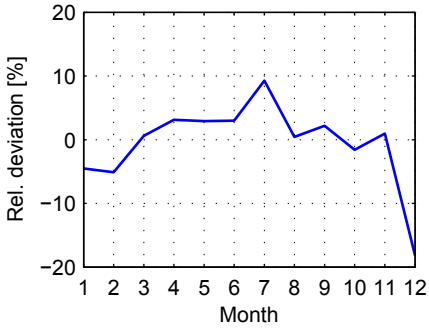

(c) Phoenix

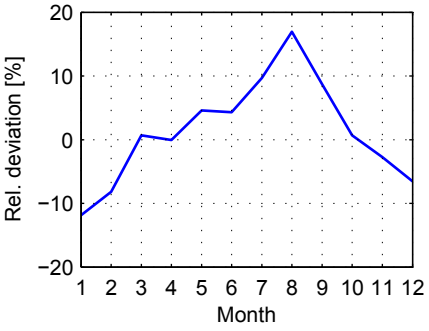

(d) New Delhi

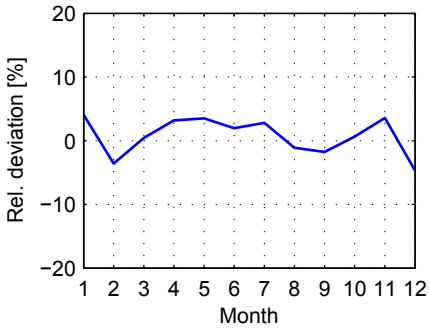

(e) Adelaide

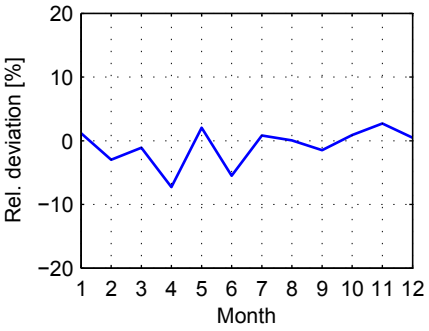

(f) Geraldton

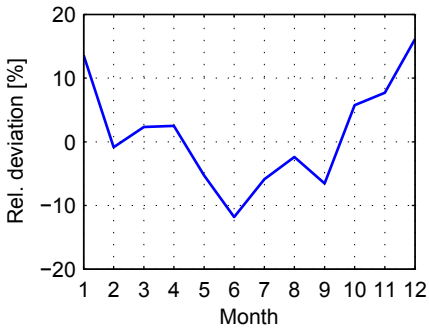

(g) Johannesburg

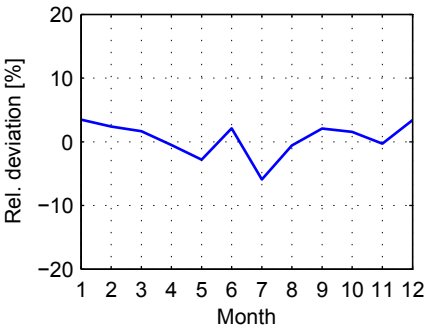

(h) Antofagasta

Figure 5.3: Deviations (%) of the synthetic monthly beam normal radiation from TMY data.

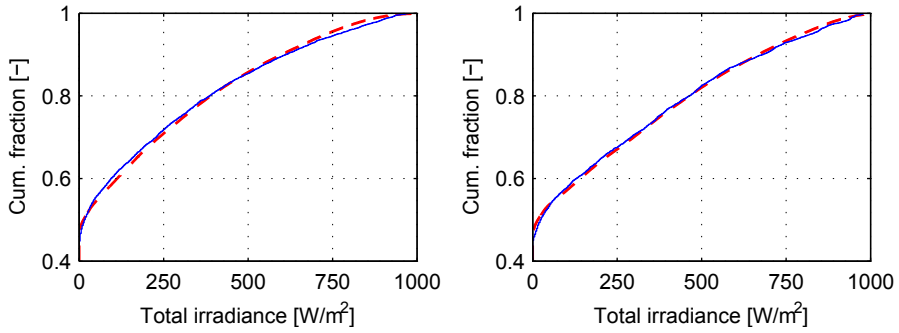

(a) Madrid

(b) Seville

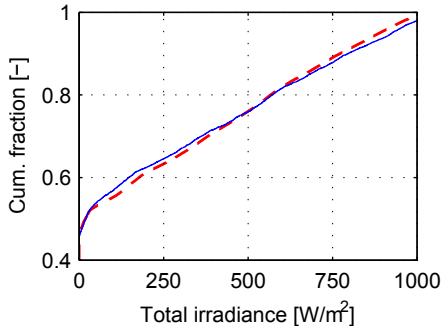

(c) Phoenix

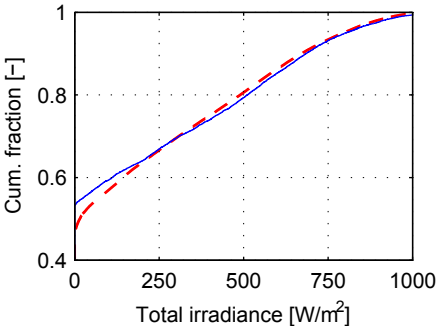

(d) New Delhi

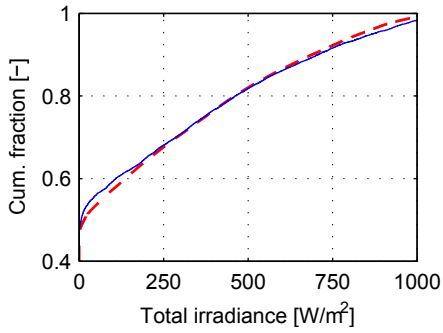

(e) Adelaide

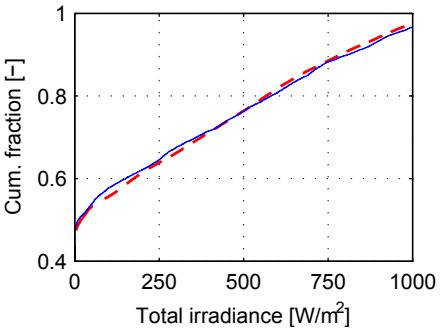

(f) Geraldton

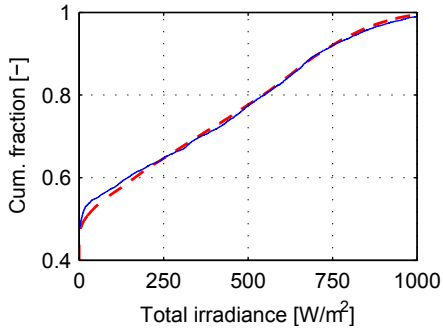

(g) Johannesburg

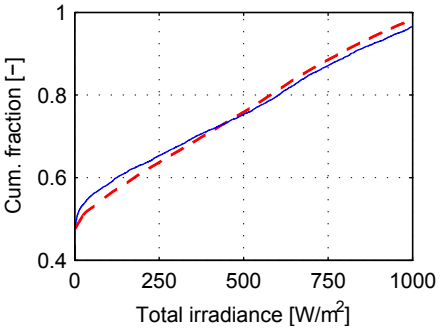

(h) Antofagasta

Figure 5.4: Cumulative distribution of actual (solid blue) and synthetic (dashed red) values of the total irradiance for selected sites

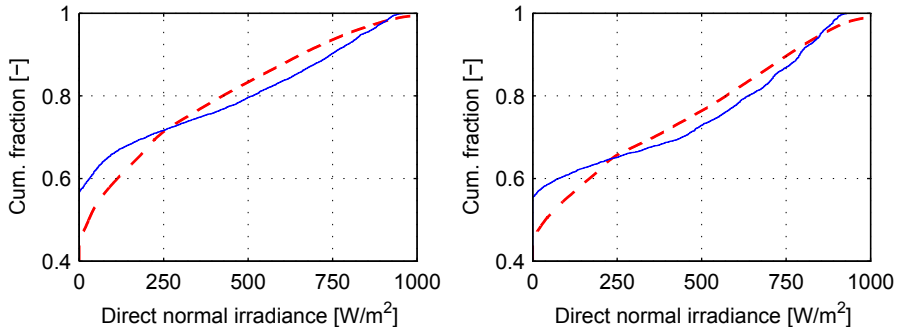

(a) Madrid

(b) Seville

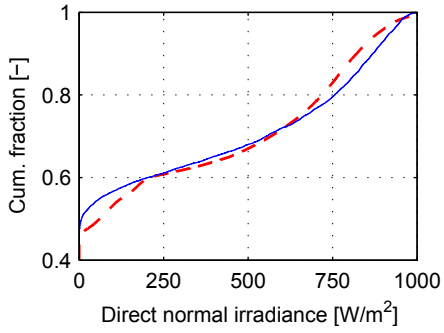

(c) Phoenix

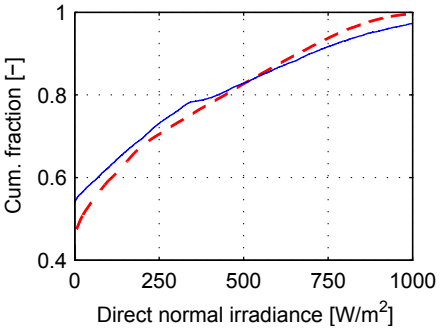

(d) New Delhi

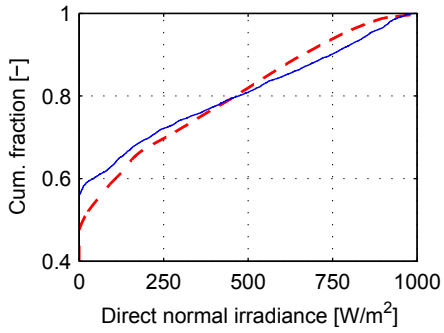

(e) Adelaide

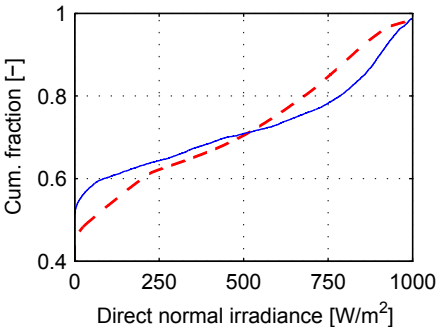

(f) Geraldton

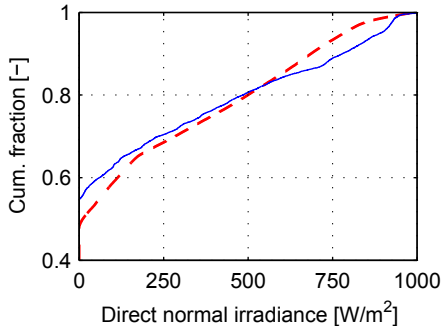

(g) Johannesburg

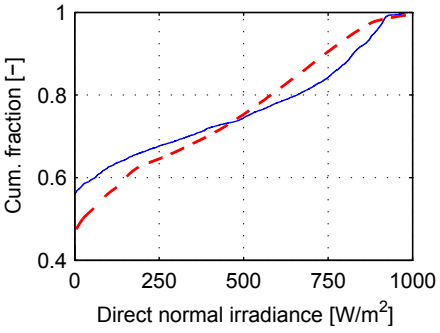

(h) Antofagasta

Figure 5.5: Cumulative distribution of actual (solid blue) and synthetic (dashed red) values of the direct normal irradiance for selected sites

5.5 CONCLUDING REMARKS

A solar radiation model was developed to create synthetic values of the hourly total, beam and diffuse radiation on a horizontal plane at a given single location.

SRM is based on the existing techniques which deploy the clearness index KT as a primary predictor variable. The calculation procedure involves determining:

1. the monthly KT time series by adding Gaussian noise to the long-term average values (the Bohlen approach)
2. the daily KT sequence by using a library of Markov transition matrices (the Aguiar daily algorithm)
3. the hourly KT series with the time-dependent, autoregressive Gaussian model (the Aguiar hourly algorithm)
4. the diffuse and beam components of solar radiation by applying the BRL approximation.

To improve the overall precision, the BRL and the Aguiar hourly (TAG) models were adjusted based on the additional investigations.

SRM was validated as an integrated tool, assuming that the individual adopted methods perform adequately as described in the original references. The validation was done simply by statistical comparison of the synthetic and TMY data for 8 selected locations. The results showed a good match between the generated total radiation sequence and the reference data. In case of direct normal radiation, relatively larger deviations were observed, with the monthly mean value of 4.1%, which are attributed to inherent limitations of the BRL and other similar approximations for the diffuse solar fraction.

Overall, it can be concluded that SRM, despite its moderate level of complexity, still provides the synthetic solar radiation data of good quality.

6 INCORPORATION OF SPATIAL CORRELATION

The solar radiation model (SRM) presented in the previous chapter is intended for single locations only. To enable its use for multisite data generation the spatial correlation of solar radiation (SCSR) has to be incorporated. The given task in this work is accomplished in two separate steps, which are described in Sections 6.1 and 6.2, respectively.

In the first step it is assumed that at long timescales general and simple characterizations of SCSR are possible. To test the given hypothesis, a regression analysis is performed by using the satellite-derived monthly and daily solar radiation data for selected US regions. The obtained regression functions linking SCSR with easily accessible inputs are cross-validated based on the solar radiation time series for locations across Spain and Germany.

In the second step, by applying the derived SCSR formulae and the existing methods of linear algebra, a general procedure is proposed for integrating SCSR into univariate stochastic algorithms. The procedure deploys the common technique of enforcing spatial correlation between output parameters by feeding a given stochastic algorithm with the spatially correlated random number streams.

6.1 CHARACTERIZATION OF THE SPATIAL CORRELATION OF SOLAR RADIATION

6.1.1 *Hypothesis and methodology*

As noted earlier, the hypothesis is that at long timescales a general relation for SCSR can be derived based on simple and easily accessible inputs.

From various available parameters the clearness index KT is selected to represent the solar radiation, by taking into account: (a) its common use in climate research, particularly in the area of synthetic data generation; and (b) its straightforward calculation allowing exclusion of the local factors such as site altitude and turbidity levels required in the clear-sky index estimation.

In order to remove the non-stationarity (trend) in the KT time series, the differencing is applied, which means that the focus is not on the actual values of KT, but on its ramp rates ΔKT – the changes in the KT value from one timestep (e. g. month, day or hour) to the next.

The final objective in this case is defined as to perform a regression analysis of historical meteorological data and to determine mathematical expressions that would allow quantifying SCSR for any two locations at monthly and daily timescales by using intersite distance and monthly statistics of KT.

The adopted methodology involves:

- use of extensive meteorological data covering multiple geographical regions and climate zones to capture general patterns of SCSR
- simplification of descriptive models to avoid overfitting [81]

The main aspects of the performed regression analysis are described in the following text. Considering the heuristic nature of the study the author admits that the selected methods and the obtained results might not be optimal.

All simulations and data analyses were done in Matlab.

6.1.1.1 *Data*

Two datasets were used in the study. The main set, taken from the satellite-derived SolarAnywhere Data (available within the US National Solar Radiation Database [104]), comprises the hourly radiation data for the period of 1998–2009 at 1591 locations evenly distributed (grid spacing 0.2°) over 4 US regions as shown in Fig. 6.1a. The total number of location pairs is over 300,000 with intersite distances in the range of 15–540 km (mean 205 km). The regions were selected arbitrarily to represent various climates and thus to increase the data diversity. The boundaries and resolution of the data grid points had to be limited to reduce the computational time. The chosen distance range was found to be sufficient to model fully SCSR at a daily timescale.

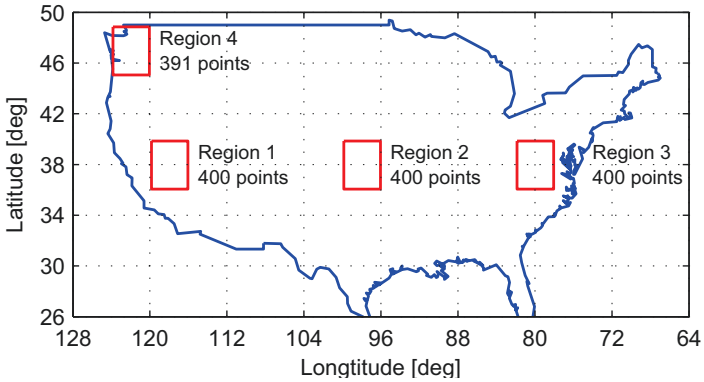

(a) Main locations in the US

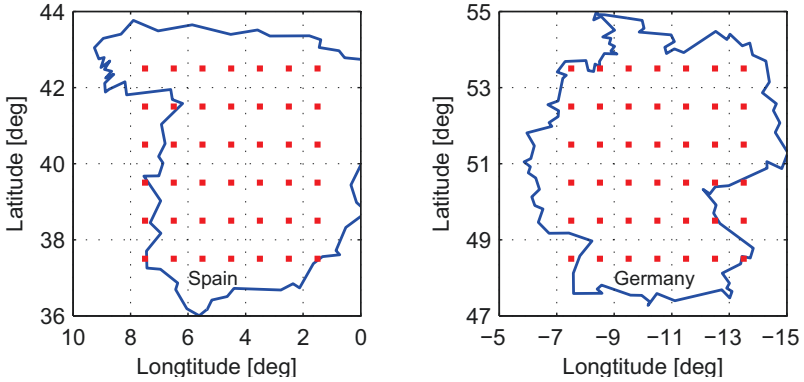

(b) Additional locations in Europe

Figure 6.1: Selected sites for solar radiation data

The additional dataset, taken from [102], consists of daily solar radiation values for the period of 1993–2004 at 84 locations (grid spacing 0.5°) primarily over Spain and Germany as shown in Fig. 6.1b. The total number of location pairs is over 1500 with intersite distances in the range of 65–550 km (mean 295 km). The additional set was used only for testing the performance of the final regression models.

The clearness index, when not given directly, was calculated from its definition as the ratio between the global solar radiation on a horizontal plane and the corresponding extraterrestrial radiation (see Chapter 3).

6.1.1.2 *Initial domain of variables*

The initial domain of variables refers to the set of the response (output) and the explanatory (input) parameters used during the regression analysis. The selected candidate response variables or SCSR estimators consist of:

standard deviation of difference

$$\mathrm{SDD} = \mathtt{std}(\Delta \mathrm{KT}_a - \Delta \mathrm{KT}_b) \tag{6.1}$$

normalized standard deviation of difference

$$\mathrm{NSDD} = \frac{\mathrm{SDD}}{[\mathtt{std}(\Delta \mathrm{KT}_a)\,\mathtt{std}(\Delta \mathrm{KT}_b)]^{0.5}} \tag{6.2}$$

Pearson's correlation coefficient

$$\mathrm{PCC} = \mathtt{corr}(\Delta \mathrm{KT}_a, \Delta \mathrm{KT}_b) \tag{6.3}$$

where the subscripts a and b refer to the two locations in the data pair. Note, that PCC can alternatively be expressed as:

$$\mathrm{PCC} = \frac{\mathtt{std}(\Delta \mathrm{KT}_a)^2 + \mathtt{std}(\Delta \mathrm{KT}_b)^2 - \mathrm{SDD}^2}{2\,\mathtt{std}(\Delta \mathrm{KT}_a)\,\mathtt{std}(\Delta \mathrm{KT}_b)} \tag{6.4}$$

For the explanatory parameters, it was assumed that besides the distance d_{site}, SCSR can also be characterized by certain mathematical indicators of intersite dependence (MIID) X_j determined by the monthly average values of the clearness index $\widehat{\mathrm{KT}}_{month}$. The author chose arbitrarily 16 MIIDs as shown in Table 6.1. Thus, the initial set of input variables was limited to d_{site} and X_{1-16}.

The intersite distance was calculated based on the Haversine formula [138]:

$$\begin{cases} d_{site} = 2 \times 6371 \times \mathrm{atan2}(\sqrt{C}, \sqrt{1-C}), \\ C = \sin^2 \dfrac{\phi_a - \phi_b}{2} + \sin^2 \dfrac{\lambda_a - \lambda_b}{2} \times \cos\phi_a \times \cos\phi_b, \end{cases} \tag{6.5}$$

where ϕ and λ are the latitude and longitude of the site.

$$
\begin{aligned}
X_1 &= \{\mathtt{mean}(A) + \mathtt{mean}(B)\}/2 \\
X_2 &= \{\mathtt{max}(A) - \mathtt{min}(A) + \mathtt{max}(B) - \mathtt{min}(B)\}/2 \\
X_3 &= \{\mathtt{std}(A) + \mathtt{std}(B)\}/2 \\
X_4 &= \{\mathtt{mean}(|\Delta A|) + \mathtt{mean}(|\Delta B|)\}/2 \\
X_5 &= \{\mathtt{max}(\Delta A) - \mathtt{min}(\Delta A) + \mathtt{max}(\Delta B) - \mathtt{min}(\Delta B)\}/2 \\
X_6 &= \{\mathtt{std}(\Delta A) + \mathtt{std}(\Delta B)\}/2 \\
X_7 &= |\mathtt{mean}(A) - \mathtt{mean}(B)| \\
X_8 &= |\mathtt{max}(A) - \mathtt{min}(A) - \mathtt{max}(B) + \mathtt{min}(B)| \\
X_9 &= |\mathtt{std}(A) - \mathtt{std}(B)| \\
X_{10} &= |\mathtt{mean}(|\Delta A|) - \mathtt{mean}(|\Delta B|)| \\
X_{11} &= |\mathtt{max}(\Delta A) - \mathtt{min}(\Delta A) - \mathtt{max}(\Delta B) + \mathtt{min}(\Delta B)| \\
X_{12} &= |\mathtt{std}(\Delta A) - \mathtt{std}(\Delta B)| \\
X_{13} &= \mathtt{std}(A - B) \\
X_{14} &= \mathtt{std}(\Delta A - \Delta B) \\
X_{15} &= \mathtt{corr}(A, B) \\
X_{16} &= \mathtt{corr}(\Delta A, \Delta B)
\end{aligned}
$$

Note: $\widehat{\mathrm{KT}}_{\mathrm{month}}$ values for two locations are substituted by A and B. The ramp rate ΔA (or ΔB) is defined as the difference between A (or B) values for the current and previous month.

Table 6.1: Chosen mathematical indicators of intersite dependence (MIID)

6.1.1.3 *Functional form of the regression*

The regression function represents a mathematical relation between the selected response and explanatory variables. Its objective is to quantify SCSR for a given location pair with the best possible precision when the historical solar radiation time series are not available and thus the expressions (6.1)–(6.3) cannot be used.

In this study the functional form of the regression was assumed to be a linear or quadratic polynomial. The fitting of the polynomial to the main dataset was done by using Matlab function *polyfitn* from [37]. The intercept was not forced to zero (or unity), because it reduces the model performance to a certain extent. In order to avoid overfitting, the number of explanatory variables was limited to two, which means that in addition to the intersite distance $\mathrm{d}_{\mathrm{site}}$ the author had to choose one of the candidate MIIDs defined in Table 6.1.

The polynomials of a higher degree ($\mathrm{n_p} > 2$), not preferred due to their complexity (large number of terms), were also tested in the preliminary studies and the results showed that the regression model would not improve significantly and it would usually produce unrealistic nonlinear patterns.

6.1.1.4 *Model performance assessment and variables selection*

The goodness of fit was evaluated by the coefficient of determination R^2, which is a commonly reported measure of regression fit [59] and a reasonable estimator of single variable relevance [58]. R^2 equals to the square of the correlation coefficient between the actual and predicted values of a given variable.

The parameters selection in this study was straightforward and involved data fitting at various combinations of response (SDD, NSDD or PCC) and explanatory (d_{site}, X_j) variables and choosing the most adequate ones based on the R^2 value.

The dependence of the regression fit on the number of predictors was estimated based on step-wise regression [58], which starts with d_{site} in the model and at each step adds the indicator X_j that improves the model performance most.

Considering a large sample size, the application of more advanced statistical tests such as the Fisher test was found to be unnecessary [59, 86]. For the same reason the cross-validation during variables selection was not required [58].

In addition to the quantitative assessments, the visual examination of the model predictions and mispredictions was also conducted, though not presented in this thesis.

6.1.2 *Results*

The regression analysis was performed on a workstation (Intel Xeon W3503, 12 GB RAM, 2.4 GHz) in three general steps: (a) the required data for each site were extracted from the original source files and the missing variables were calculated; (b) the selected SCSR estimators were determined for each location pair; and (c) the linear and quadratic polynomial regressions were fitted for different combinations of the response and explanatory parameters. The respective computational times were approximately 2 seconds per site, 0.1 seconds per location pair and 0.5 seconds per parameter combination, which, for example, for the main dataset totals to more than 9 hours of simulations.

6.1.2.1 *Regional features of the main dataset*

According to the adopted approach for the SCSR characterization, the main data should have a large number of samples and a certain level of diversity. To demonstrate the latter, the plots of PCC versus distance at monthly, daily and hourly timescales are presented in Fig. 6.2 for each of the selected US regions. As one can see, there are notable variations in SCSR within and among the regions.

The spatial correlation in general decreases with higher distance and lower timescale. This trend, however, is less pronounced and even reversed when moving to the hourly timescale. As shown in Fig. 6.2 after the initial sharp drop the hourly PCC declines with the distance very slowly and maintains relatively high values (at some point exceeding the corresponding daily PCC) even at the distances for which the hourly weather changes at two locations are expected to be nearly independent. The reason is that the clearness index probability

distribution depends not only on the sky conditions (e.g. cloud cover, aerosol content), but also on the optical air mass [10, 116], which means that the hourly KT variations are driven to a certain extent by the diurnal cycle of the sun.

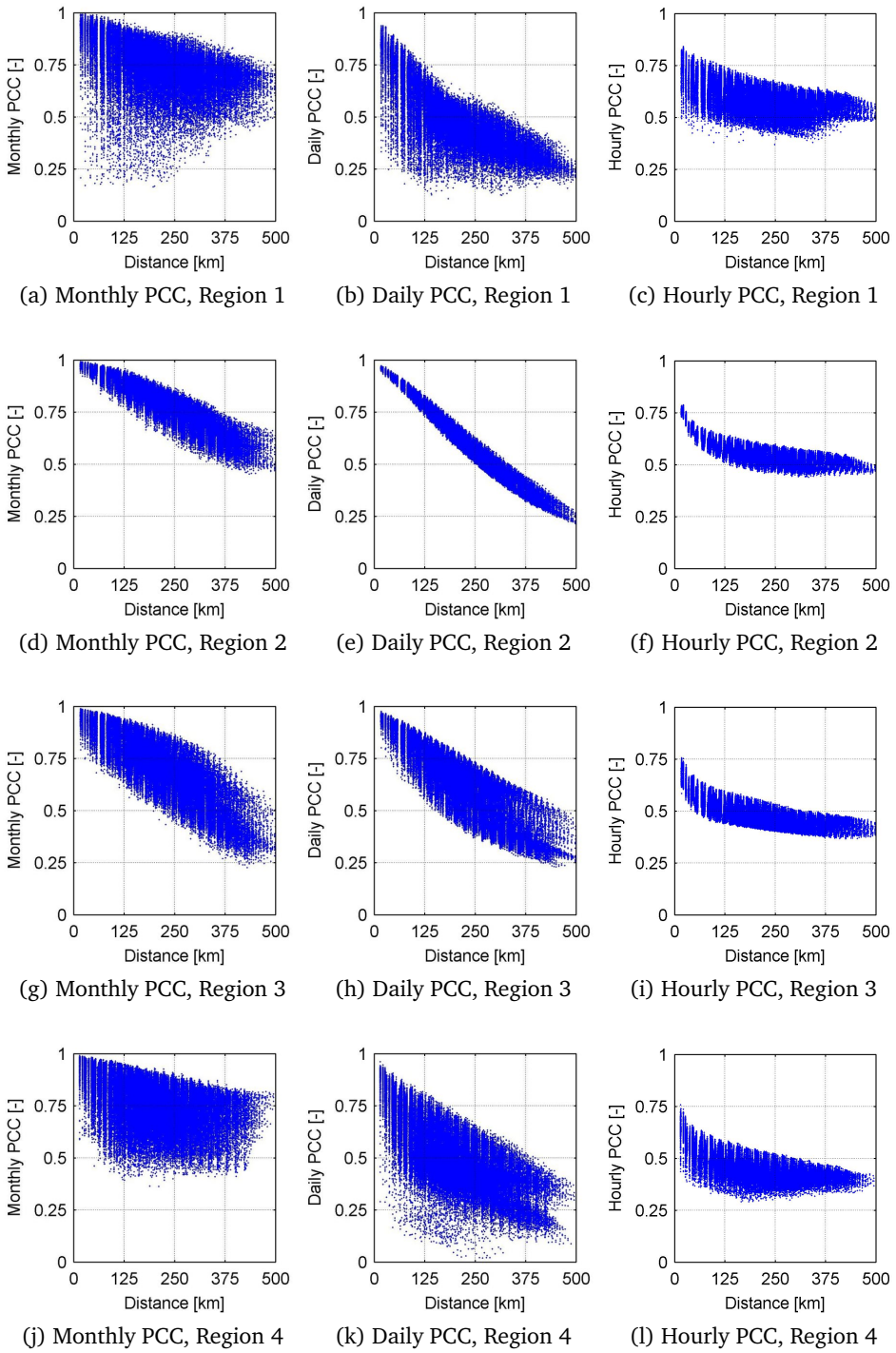

(a) Monthly PCC, Region 1 (b) Daily PCC, Region 1 (c) Hourly PCC, Region 1

(d) Monthly PCC, Region 2 (e) Daily PCC, Region 2 (f) Hourly PCC, Region 2

(g) Monthly PCC, Region 3 (h) Daily PCC, Region 3 (i) Hourly PCC, Region 3

(j) Monthly PCC, Region 4 (k) Daily PCC, Region 4 (l) Hourly PCC, Region 4

Figure 6.2: Actual variation of PCC with distance for the location pairs in the selected 4 US regions

6.1.2.2 *Regression analysis*

The results from the step-wise regressions for all SCSR estimators when using both linear and quadratic models are presented in Fig. 6.3. It shows how the regression fit improves with subsequent aggregation of the explanatory variables; as it was mentioned above the procedure in this case was to start with d_{site} in the model and add at each step the indicator X_j that improves the model performance most. Fig. 6.3 together with the visual data inspection allow the following important observations:

- The adequate response variables are SDD for the monthly timescale and NSDD and PCC for the daily timescale.
- The combination of distance with only one MIID as input improves notably the model performance ($R^2 > 0.8$). The most relevant indicator seems to be X_{14}. With the addition of further MIIDs the corresponding gain is negligible.
- For the monthly SCSR the linear polynomial is sufficient, whereas for the daily SCSR the quadratic approximation is more accurate.

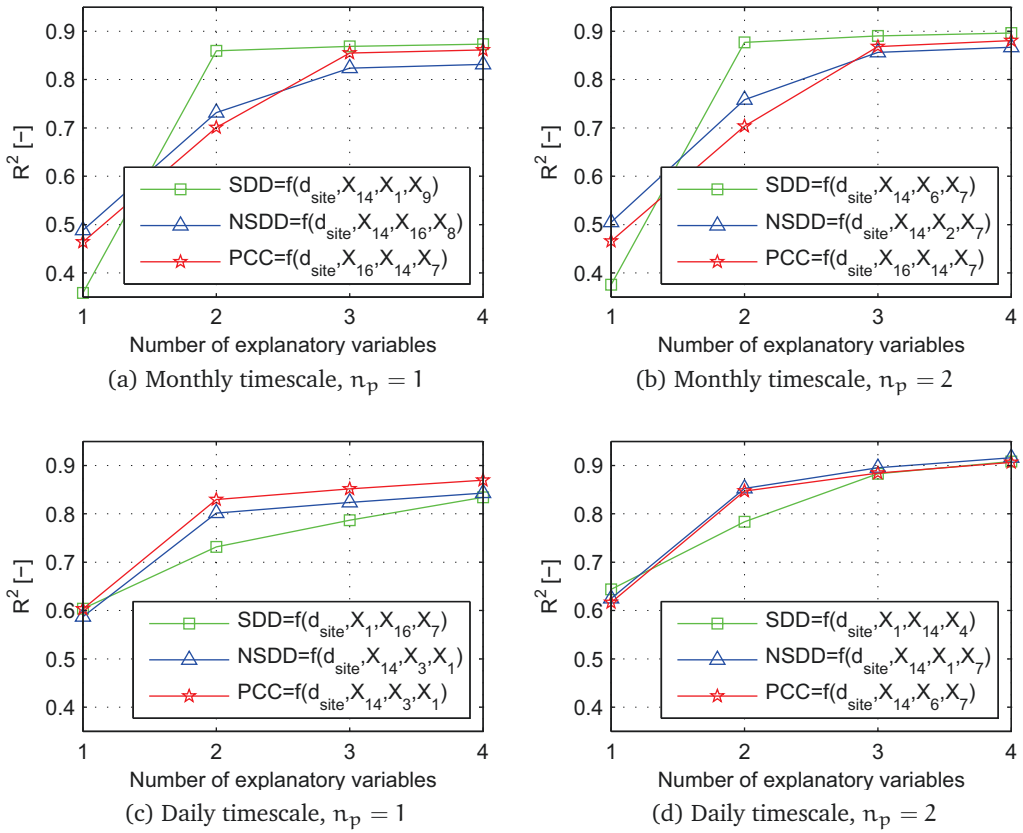

(a) Monthly timescale, $n_p = 1$ (b) Monthly timescale, $n_p = 2$

(c) Daily timescale, $n_p = 1$ (d) Daily timescale, $n_p = 2$

Note: n_p denotes the degree of the fitted polynomial. The legend shows the identified explanatory variables in the order of aggregation.

Figure 6.3: Results of the step-wise regression (main dataset)

The R^2 values of the linear and quadratic models linking the 'best' SCSR estimators (SDD_{month}, $NSDD_{day}$ and PCC_{day}) with the distance and one MIID are compared in Fig. 6.4, which once again demonstrates the relevance of X_{14} as the additional explanatory variable.

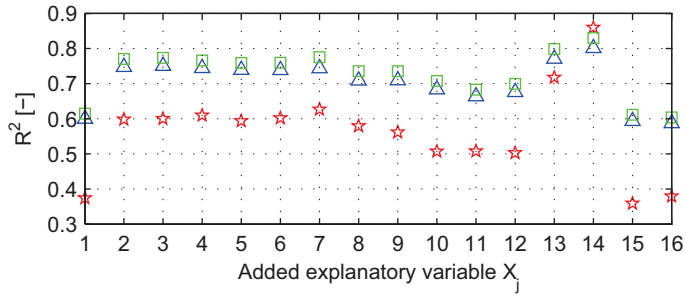

(a) Linear model ($n_p = 1$)

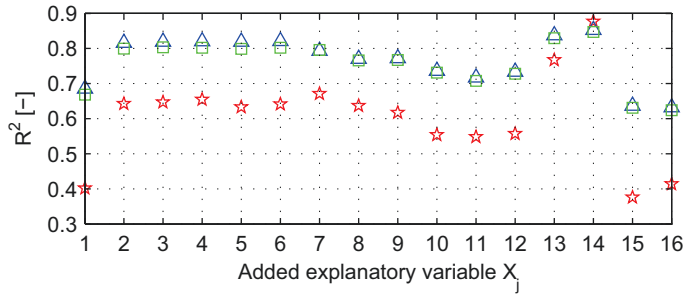

(b) Quadratic model ($n_p = 2$)

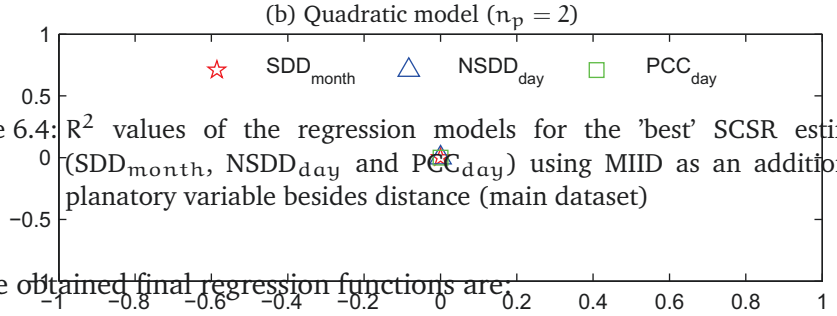

Figure 6.4: R^2 values of the regression models for the 'best' SCSR estimators (SDD_{month}, $NSDD_{day}$ and PCC_{day}) using MIID as an additional explanatory variable besides distance (main dataset)

The obtained final regression functions are:

$$SDD_{month} = 4.462e{-}05\, d_{site} + 1.0594\, X_{14} + 0.017, \tag{6.6}$$

$$\begin{aligned} NSDD_{day} = &- 1.0769e{-}06\, d_{site}^2 - 0.0302\, d_{site}\, X_{14} + 0.0022\, d_{site} \\ &- 132.3022\, X_{14}^2 + 22.8342\, X_{14} + 0.2428, \end{aligned} \tag{6.7}$$

$$\begin{aligned} PCC_{day} = &6.6044e{-}08\, d_{site}^2 + 0.0162\, d_{site}\, X_{14} - 0.0013\, d_{site} \\ &+ 70.8353\, X_{14}^2 - 15.5606\, X_{14} + 1.0516, \end{aligned} \tag{6.8}$$

where the input parameters are limited as:

$$15 \leqslant d_{site} \leqslant 500,\ X_{14} \leqslant 0.06 \tag{6.9}$$

$$d_{site} \leqslant 650 - 7500\, X_{14} \text{ (only for daily SCSR)} \tag{6.10}$$

The restriction associated with (6.10) approximately represents the boundary after which the values of the daily SCSR estimators stagnate; according to (6.7) and (6.8) it roughly corresponds to $NSDD_{day}$=1.2 and PCC_{day}=0.3.

Both the real and the predicted variations of the chosen SCSR estimators with d_{site} and X_{14} are illustrated in Figs. 6.5 and 6.6 for the main and additional (validation) datasets. One can observe how the regression models capture the linear or non-linear trends in the actual values of the response variables.

The goodness of fit statistics of the derived regression functions is summarized in Table 6.2. Besides R^2, the measures of model fit include: the root mean squared error RMSE$=\sqrt{\mathtt{mean}\,((y-y')^2)}$, the RMSE variation coefficient CV(RMSE)$=\frac{\text{RMSE}}{\mathtt{mean}(y)}$, the mean absolute error MAE$=\mathtt{mean}\,(|y-y'|)$ and the mean absolute relative error MARE$=\mathtt{mean}\,(|y-y'|/|y|)$, where y and y' denote the real and predicted values of a given output parameter, respectively. As one can see, the deviations in the case of the additional dataset are somewhat higher, but still reasonable; this confirms the overall adequacy of the proposed regression models and it thus demonstrates the feasibility of the characterization of SCSR at long timescales. It is important to be cautious, however, when applying the given models for climate zones highly divergent from that covered by the main dataset.

During the study the SCSR analysis was also performed for the hourly timescale by using the selected response and explanatory variables. General patterns were detected in the data for some combinations of the hourly SCSR estimators with the distance and MIID; for example, it was observed that the hourly PCC decreases with d_{site} and X_{14}. And yet, the dispersion of the data around the trend was always high, leading to the poor regression fit with the R^2 values less than 0.35. This confirms that at short timescales the correct estimation of SCSR might be impossible without taking into account local weather factors.

SCSR estimator	Model	R^2	RMSE	CV(RMSE)	MAE	MARE
		Main dataset				
SDD_{month}	(6.6)	0.854	0.006	0.113	0.004	0.100
$NSDD_{day}$	(6.7)	0.852	0.080	0.088	0.062	0.076
PCC_{day}	(6.8)	0.846	0.068	0.120	0.053	0.107
		Additional dataset				
SDD_{month}	(6.6)	0.733	0.007	0.158	0.006	0.135
$NSDD_{day}$	(6.7)	0.869	0.099	0.098	0.081	0.080
PCC_{day}	(6.8)	0.857	0.104	0.218	0.082	0.253

Note: The units of the goodness of fit measures are according to their definitions and may vary depending on the selected SCSR estimator.

Table 6.2: Goodness of fit of the final regression models

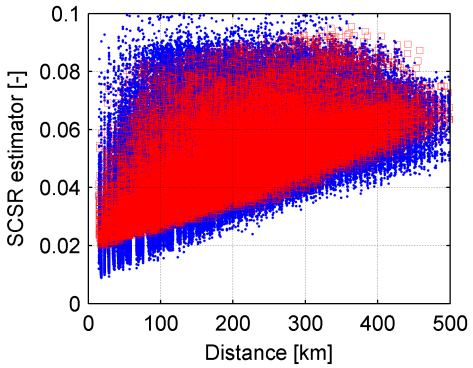

(a) Monthly SDD versus distance

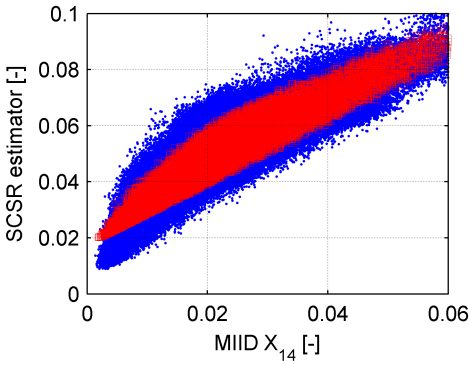

(b) Monthly SDD versus X_{14}

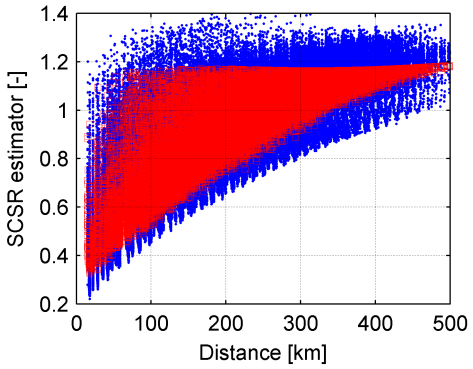

(c) Daily NSDD versus distance

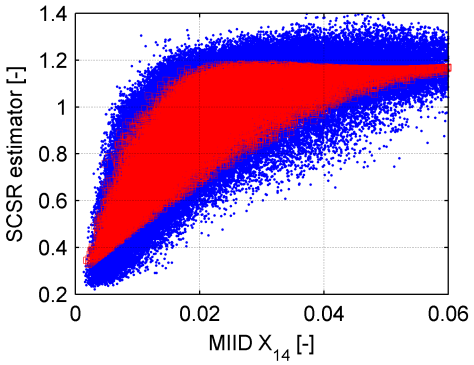

(d) Daily NSDD versus X_{14}

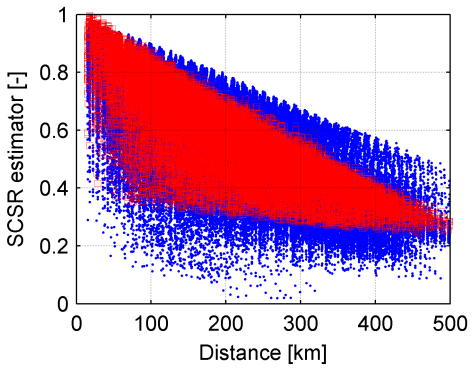

(e) Daily PCC versus distance

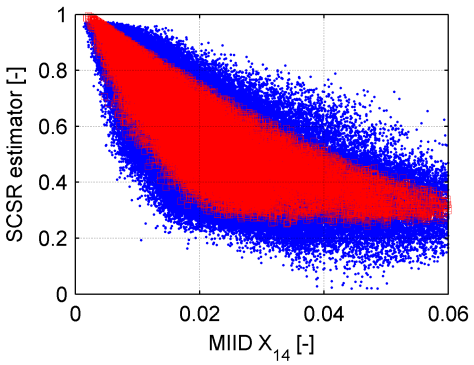

(f) Daily PCC versus X_{14}

Figure 6.5: Predicted (red squares) and actual (blue dots) variation of the chosen response parameters with distance and MIID X_{14} (main dataset)

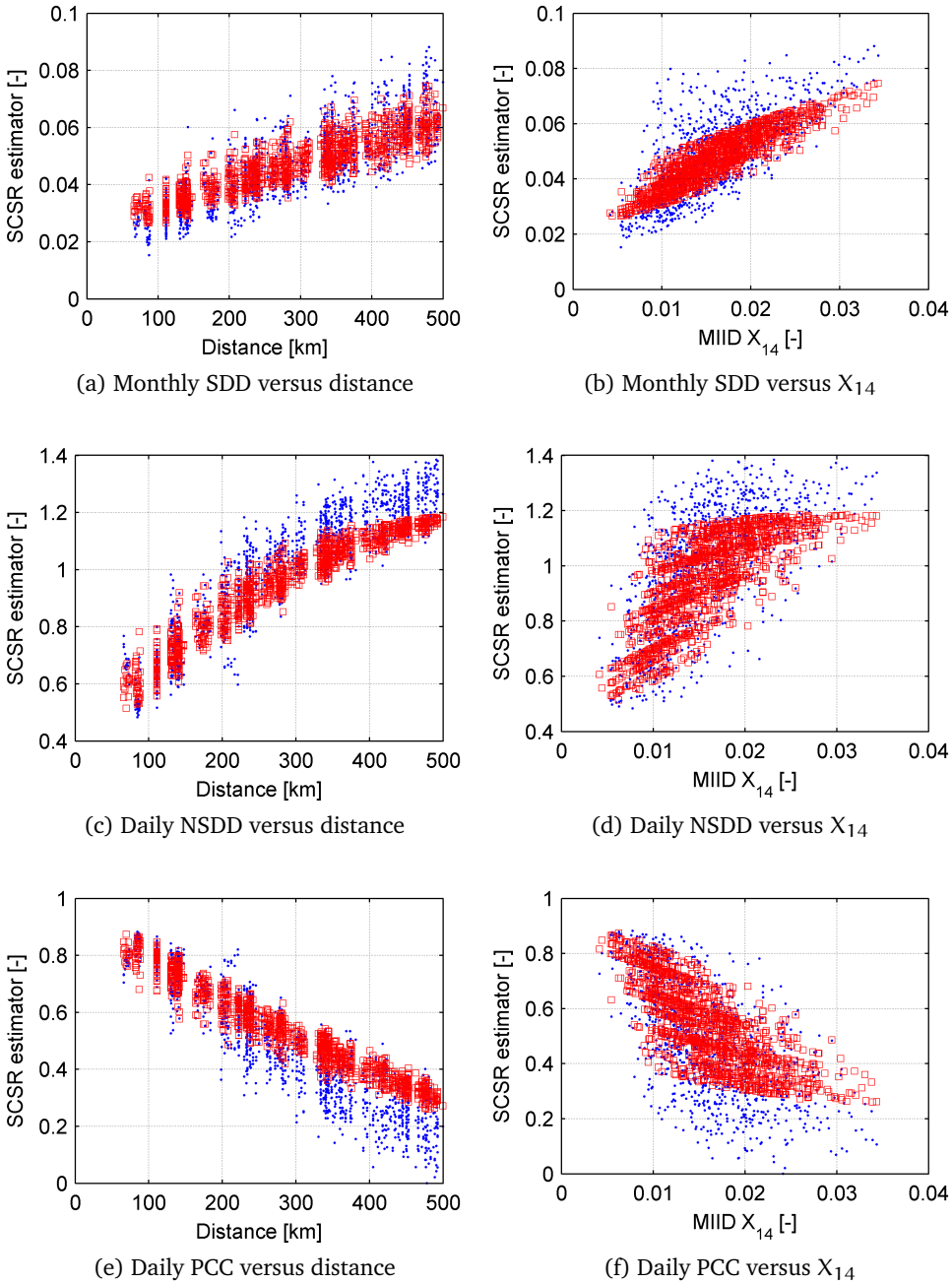

(a) Monthly SDD versus distance

(b) Monthly SDD versus X_{14}

(c) Daily NSDD versus distance

(d) Daily NSDD versus X_{14}

(e) Daily PCC versus distance

(f) Daily PCC versus X_{14}

Figure 6.6: Predicted (red squares) and actual (blue dots) variation of the chosen response parameters with distance and MIID X_{14} (additional dataset)

6.2 INCORPORATING SPATIAL CORRELATION INTO STOCHASTIC MODEL

6.2.1 *Proposed procedure*

The classical univariate stochastic algorithms for synthesizing solar radiation values focus on a single location, a certain timescale and deploy the clearness index KT as the main parameter. The calculation process at each timestep involves generation of the random number $r \in (0, 1)$ and its conversion to the KT value by using autoregressive-moving-average, Markov or other stochastic model.

As it was mentioned, a simple approach to incorporate the spatial correlation when generating the data for multiple sites is to apply it to the random number streams that drive the algorithms. The approach deploys the existing methods of linear algebra and requires the correlation matrix C_r relating the random numbers used for individual sites. It is important to note that C_r refers to the inputs of a given stochastic algorithm, whereas SCSR refers to the algorithm outputs, i. e. the KT time series.

In this work SCSR is also integrated by feeding a stochastic model with the spatially correlated random numbers. The difference of the adopted technique is that the expected SCSR is evaluated by the derived regression equations (6.6)–(6.8), and it is then used to determine C_r through iterative runs of a given stochastic model with the objective to match the simulated and expected values of SCSR. The calculation of C_r is associated with the identification of its mathematical relation to SCSR by trial and error. The relation in general is expressed as:

$$C_r = f(PCC, \nu_i) \tag{6.11}$$

where ν_i are the constants that are to be determined together with the functional form of (6.11). PCC is chosen as a primary SCSR estimator because it makes the overall calculation procedure more robust according to the performed numerical tests.

Considering this, the proposed steps for incorporating spatial correlation into univariate stochastic algorithm are as follows:

1. Calculate the expected PCC values for the given location pairs. At a daily timescale it is done directly by using (6.8). At a monthly timescale (6.4) is employed for which the missing SDD_{month} is obtained from (6.6) and $\mathtt{std}(\Delta KT)$ from the data series created by running the stochastic model for each site independently.

2. Choose (new) functional form (e.g. polynomial) and/or initial values of the constants ν_i for (6.11).

3. Determine the correlation matrix C_r from (6.11) based on the expected PCC and the current values of ν_i.

4. Generate the correlated time series of KT simultaneously for all given locations. This only requires feeding the original stochastic algorithm at each timestep with the correlated random numbers. The latter are obtained by using the Cholesky factorization[1]:

$$U^T \times U = C_r \tag{6.12}$$

$$r_{corr} = r \times U \tag{6.13}$$

where U is the upper triangular matrix satisfying (6.12); and r, r_{corr} are normally distributed independent and correlated random numbers from 0 to 1 for all locations at a given timestep. When a distribution other than normal is needed, r_{corr} can be modified by using inverse transform sampling.

5. Calculate from (6.3) the resultant (simulated) PCC for the generated KT time series.

6. Compare the resultant and expected PCC both qualitatively and quantitatively, for example, by using scatter plot and one of the goodness of fit measures. If the deviations are not acceptable, but there is noticeable reduction compared to the previous run, update the constants v_i by fitting equation (6.11) to the current values of C_r and the resultant PCC based on the least squares method, and repeat from Step 3. If the results are poor and they differ negligibly from the previous iteration, start over from Step 2. The simulations are continued until the desired fit is achieved.

It is important to note that the exact implementation of the described procedure and its success depend on the features of selected stochastic algorithm. For example, if the algorithm performs repetitive runs until certain conditions are satisfied, the simultaneous multisite data generation (Step 4) might not be effective. The reason is that an increase in the number of locations reduces dramatically the probability of achieving the KT values for all sites within the specified limitations. This shortcoming can be mitigated by relaxing the restrictions, but this method implies a compromise between data quality on local and regional scales.

6.2.2 *Demonstration*

The proposed procedure for incorporating SCSR into synthetic data generation was tested by using the Bohlen [22] and Aguiar [3] stochastic algorithms for monthly and daily timescales, respectively. The simulations were performed for the 4 US regions and the time period (12-year) covered by the main dataset (see Section 6.1.1.1) and by using the corresponding average values of the monthly KT as inputs. The total computational time on the workstation was up to 4 seconds per site.

1 If the correlation matrix C_r is not positive-definite as required for the Cholesky decomposition, one can use the nearest positive-definite matrix instead, determined by one of the existing methods of linear algebra. In this work the author adopted the tool from [38].

When applying the Aguiar model, the restriction on the deviation of the generated daily KT values from the monthly average was relaxed in order to avoid an endless loop. Even though this led to the maximum deviations of up to 9%, on the average (among all sites) the observed discrepancy was less than 3%, which was considered reasonable.

The general relation (6.11) was substituted by

$$C_r = \nu_1 \times PCC + \nu_2 \tag{6.14}$$

The constants were initialized as $\nu_1 = 1$ and $\nu_2 = 0$. The calculation procedure had to be repeated only once or twice, since after that no more improvements were observed in the results. The calibrated values of the constants ν_1 and ν_2 are given in Table 6.3.

US region	ν_1	ν_2
1	1.12 (1.04)	–0.16 (0.06)
2	1.00 (0.98)	0 (0.04)
3	1.00 (0.98)	0 (0.06)
4	1.21 (1.04)	–0.27 (0.01)

Table 6.3: The adopted constants for (6.14) at a monthly (daily) timescale

The resultant PCC for the final generated synthetic data are compared to the expected (based on the regression models) values in Fig. 6.7. Relatively higher dispersion of the data points and thus lower R^2 at a monthly timescale is explained mainly by the shorter length of the corresponding KT time series. Overall, the fit between the simulated and expected PCC is high ($R^2 = 0.90 - 0.99$), which confirms that it is an effective approach to enforce spatial correlation to the output of stochastic models by feeding them with the correlated random number streams.

The comparisons of the simulated and actual (based on the main dataset) PCC are presented in Fig. 6.8. The data fit is lower, but reasonable ($R^2 = 0.66 - 0.93$) and it differs among the selected regions with the poor results corresponding to the regions with large spatial variation in SCSR (see Fig. 6.2). The reason is that the deviations in this case include not only the error associated with incorporation of the spatial correlation into stochastic algorithm, but also the errors in the regression functions (6.6) and (6.8) and the Bohlen and Aguiar models used in the given demonstration.

Finally, as an example, the impact of spatial correlation on the cumulative distribution of the regional (average) daily solar radiation is shown in Fig. 6.9. One can see that with integration of SCSR the qualitative difference between the actual and synthetic regional solar radiation series reduces. The main changes are observed in the tails of the cumulative distributions: the minimum and maximum values are decreased and increased, respectively. In other words, if SCSR is ignored during the multisite generation of solar radiation data, the smoothing effect in the combined fluctuations of the solar resource is overestimated.

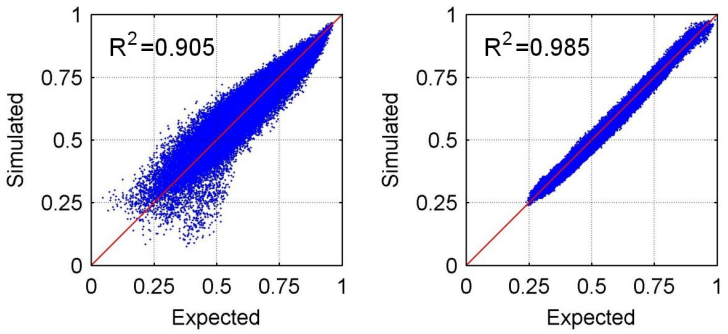

(a) Monthly PCC, Region 1

(b) Daily PCC, Region 1

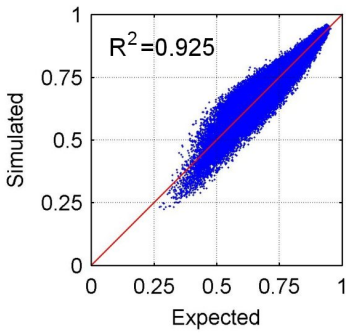

(c) Monthly PCC, Region 2

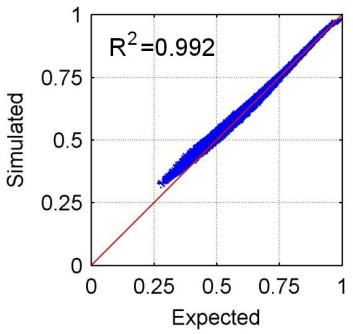

(d) Daily PCC, Region 2

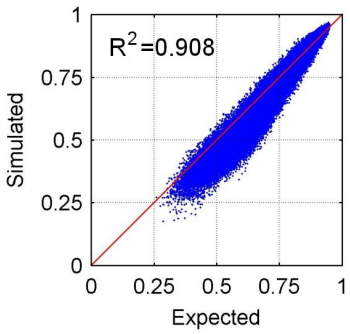

(e) Monthly PCC, Region 3

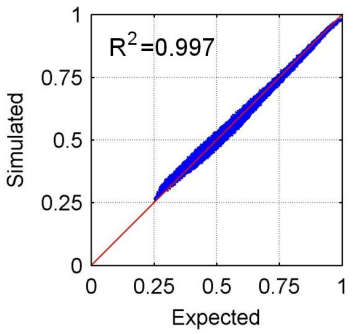

(f) Daily PCC, Region 3

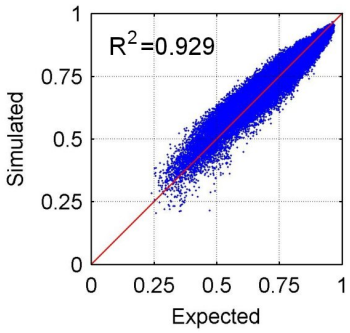

(g) Monthly PCC, Region 4

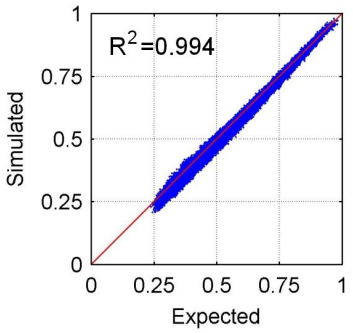

(h) Daily PCC, Region 4

Figure 6.7: Comparison of the simulated and expected PCC for the location pairs in the selected 4 US regions

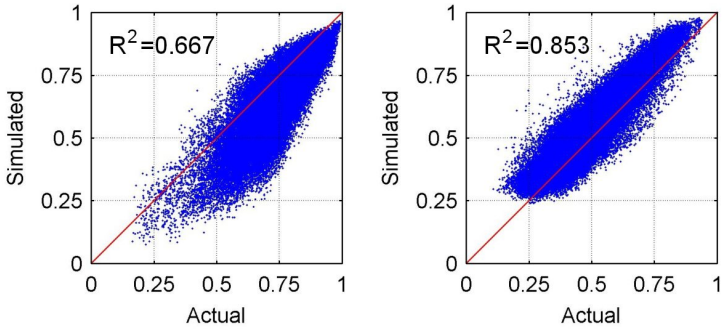

(a) Monthly PCC, Region 1

(b) Daily PCC, Region 1

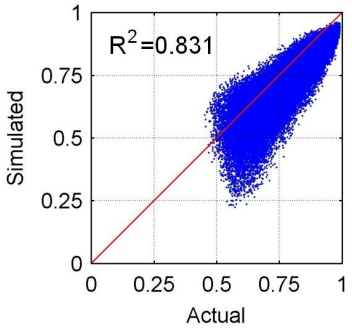

(c) Monthly PCC, Region 2

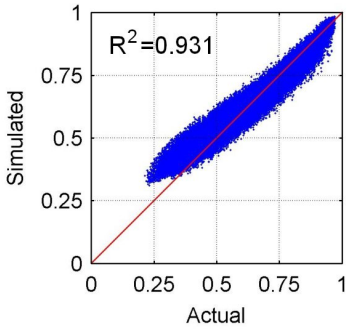

(d) Daily PCC, Region 2

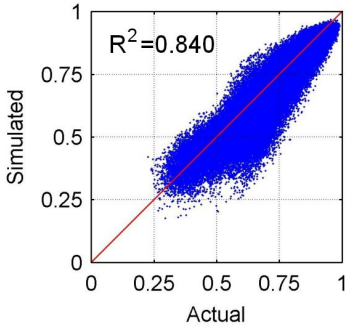

(e) Monthly PCC, Region 3

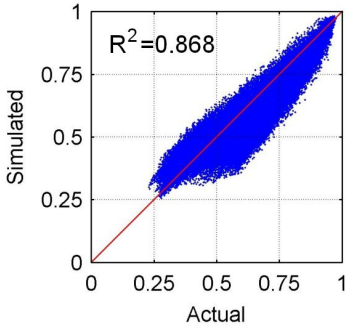

(f) Daily PCC, Region 3

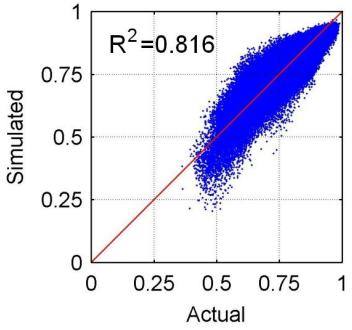

(g) Monthly PCC, Region 4

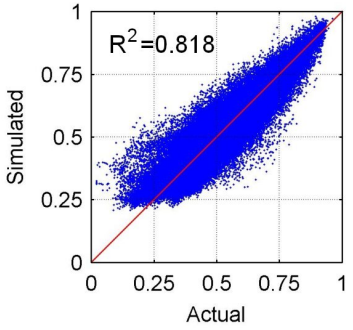

(h) Daily PCC, Region 4

Figure 6.8: Comparison of the simulated and actual PCC for the location pairs in the selected 4 US regions

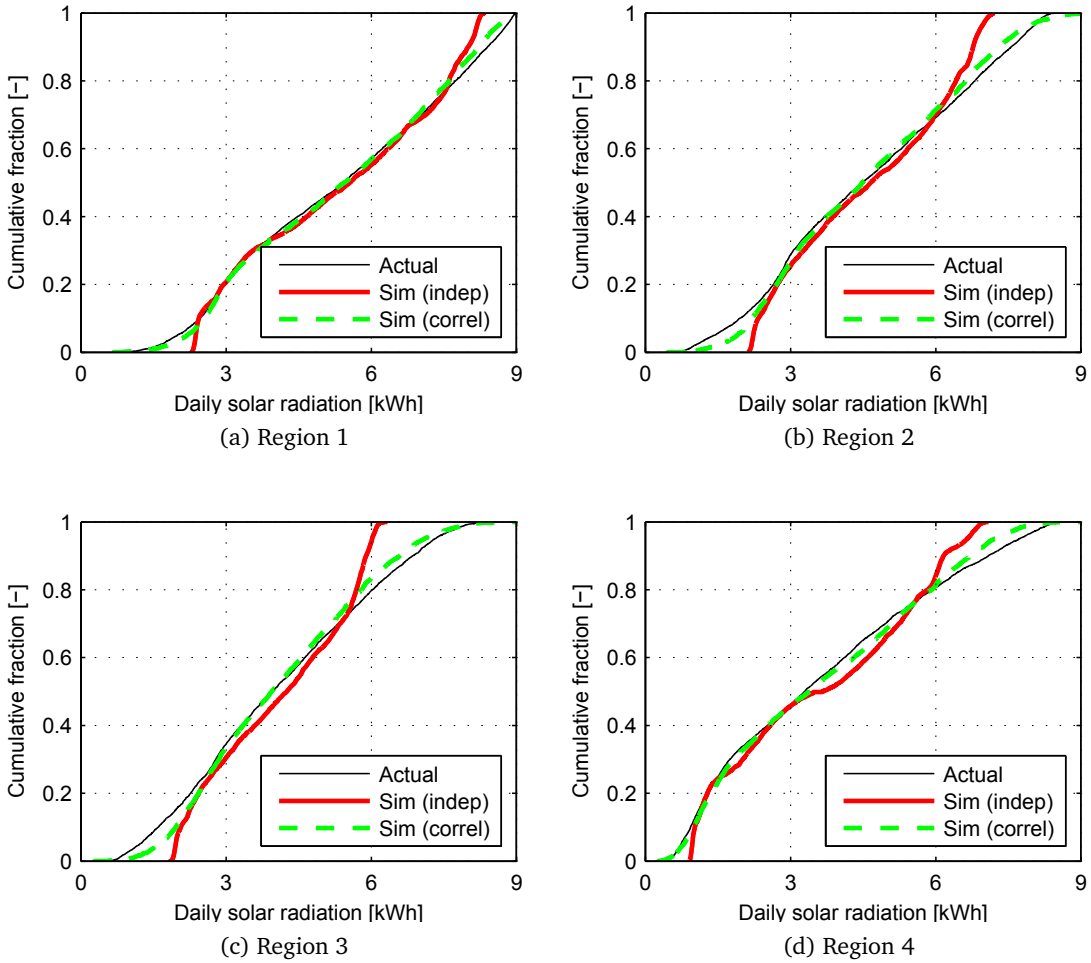

(a) Region 1 (b) Region 2

(c) Region 3 (d) Region 4

Figure 6.9: Cumulative distributions of the averaged actual and simulated time series of daily solar radiation for the selected 4 US regions

6.3 CONCLUDING REMARKS

The task of incorporating the spatial correlation into the developed solar radiation model was accomplished in two steps. In the first step a hypothesis was made that at long timescales general and simple characterizations of SCSR are possible. In order to test the hypothesis, the author performed a regression analysis of the satellite-derived monthly and daily KT values for over 300,000 location pairs in 4 US regions. It was found that:

- The adequate estimators for the spatial correlation of solar resource are $\mathrm{SDD}_{\mathrm{month}}$, $\mathrm{NSDD}_{\mathrm{day}}$ and $\mathrm{PCC}_{\mathrm{day}}$.
- In addition to the distance, the relevant explanatory variable is the indicator of intersite dependence defined by the monthly average values of KT as $X_{14} = \mathtt{std}(\widehat{\Delta \mathrm{KT}}_{\mathrm{month(a)}} - \widehat{\Delta \mathrm{KT}}_{\mathrm{month(b)}})$.
- The relation between the selected input and output parameters shows linear and quadratic trends at monthly and daily timescales, respectively.

The cross-validation of the obtained regression functions by using the additional dataset with over 1500 location pairs across Spain and Germany showed reasonable goodness of fit ($R^2 > 0.7 - 0.8$), and thus confirmed the underlying hypothesis.

In the second step, by applying the derived SCSR formulae and the existing methods of linear algebra, a general procedure was introduced for incorporating SCSR into univariate stochastic algorithms. The procedure deploys the common technique of enforcing spatial correlation between output parameters by feeding a given stochastic model with the spatially correlated random number streams. The numerical tests were performed by using two conventional stochastic solar radiation algorithms of different complexities. In both cases a good match was observed between the expected (from the regression models) and simulated values of the spatial correlation, which confirmed the effectiveness of the proposed procedure. The comparisons of the generated and actual solar radiation values also demonstrated that the quality of the synthetic data is reasonable and it improves with integration of SCSR.

It is important to note that on the hourly timescale the SCSR characterization was not possible due to significance of local weather factors. This means that the spatial correlation cannot be incorporated into the hourly stochastic algorithm (e. g. the TAG model) based on the proposed procedure. The resultant impact on the quality of the synthetic solar radiation data, however, is expected to be small. The reasons are that: (a) the spatial correlation at short timescales is relatively low, and (b) the use of the spatially correlated $\mathrm{KT}_{\mathrm{day}}$ values to generate the $\mathrm{KT}_{\mathrm{hour}}$ time series allows capturing, at least partially, the hourly SCSR.

Part III

SOLAR POWER PLANT MODELING

7 INTRODUCTION

Solar power plant model proposed in Part III of the thesis is intended for translating solar radiation time series to the corresponding power production series. The selected types of the plants are photovoltaics (PV) and concentrated solar power (CSP) based on parabolic trough and central tower technology. Because the resultant production sequence is to be used for generation system adequacy (GSA) assessments based on the sequential Monte Carlo (SMC) simulations, the research efforts focus on the model simplification and input data reduction.

7.1 LITERATURE REVIEW

7.1.1 *Photovoltaic power models*

PV power calculations involve two general steps: estimation of the solar radiation incident on a PV array, and conversion of the incident radiation to electric power.

Solar radiation on a tilted plane consists of beam, ground-reflected and diffuse components. Calculation of the first two is simple, though precision of the reflected radiation may vary depending on how the ground albedo is estimated [124].

The diffuse component is the most difficult to determine. The previous research in the given area is summarized in [108], which in addition compares the predictions by the existing models with the measurements for a site in Corsica. These performance tests can be found also for other locations in Australia [30], Iran [107], Northern Ireland [99], Belgium [35] and Spain [39, 121].

From the large number of available approaches to estimate the diffuse radiation on a tilted surface the following three are usually mentioned in literature [41] or made available in software tools [109]: Liu-Jordan (isotropic), Hays-Davies-Klucher-Reindl (HDKR) and Perez models. The first, the simplest, assumes a uniform distribution of the diffuse radiation over the sky dome, whereas the last two take into account anisotropy of the diffuse sky radiation due to circumsolar and horizon brightening. The Perez technique on average performs best, and yet a number of studies [121], including this one, prefer the HDKR model, as it provides a good balance between accuracy and complexity [41].

When it comes to conversion of the incident radiation to electric power, one way is to use available empirical correlations relating the power to solar radiation and PV cell temperature [142]. The latter in this case is usually expressed as a function of the incident radiation and ambient temperature based on a simplified heat balance.

A more detailed approach involves incorporation of PV cell current-voltage characteristics typically based on a single-diode equivalent circuit model. The comparison of the selected techniques in [28] shows that the existing methods differ mainly in representation of the current-voltage curve and calculation procedure of the missing parameters. According to validation tests the average precision achieved by the detailed physical modeling of PV array performance is approximately 2–5% at a monthly [20, 31] and 6% at an hourly [23] timescale. The model developed by King [77] is considered the most precise, but it requires large number of empirically derived coefficients, which are not always available. De Soto [33, 34] addresses this problem by proposing an alternative 5-parameter model, which uses the typical PV data from manufacturer without compromising the overall accuracy.

These and other models for the tilted surface solar radiation and PV array performance are implemented in a number of software tools as reviewed in [79, 82]. Among the tools made available free of charge are: ESP-r [48] from University of Strathclyde, RETScreen [103] from Natural Resources Canada, Greenius [40] from the German Aerospace Center (DLR), PVWatts [110] and System Advisor Model (SAM) [109] from National Renewable Energy Laboratory (NREL).

7.1.2 *Concentrated solar power models*

Parabolic trough or central receiver based CSP plant is of significantly higher complexity compared to PV system and its modeling requires application of multiple disciplines, such as concentrator optics, heat transfer and thermodynamics.

The CSP plant simulation comprises two general steps: conversion of the normal beam (direct) solar radiation to the useful thermal energy and translation of the latter to electric power. In the first step the analysis is centered on the field of parabolic troughs or heliostats combined with central tower, and the related optical and thermal energy losses are estimated. In the second step the modeling focuses on the power block operating on a conventional Rankine (steam turbine), Brayton (gas turbine) or combined cycle, and the corresponding thermodynamic and thermal losses are determined. The given calculations are governed by the control strategy, which is the most important simulation aspect, particularly for the plant configurations with thermal energy storage and auxiliary burner. The control strategy ensures that the system components operate within specified limitations and determines how and when each component is dispatched.

There is a large amount of research on modeling of CSP plant and its components according to the general literature reviews [14, 140]. The examples of the full system simulations for parabolic trough and central receiver technologies can be found in [71, 83, 87, 100, 114, 131] and [6, 55, 143, 154, 163], respectively. It is observed that researchers usually:

- prefer to develop their own models to gain freedom and flexibility in usage. The programming in this case is facilitated by the thermodynamics and heat transfer oriented software tools such as TRNSYS [150] and Engineering Equation Solver (EES) [49].
- focus on CSP plant operating on a simple Rankine cycle with the solar-driven strategy (i. e. producing whenever the thermal energy from the solar field or storage is available), though other controls approaches are also studied [52, 156]
- substitute full analytical models for individual components and processes with simplified regression functions and correlations to reduce the computational cost. How and to which extent these simplifications are applied depends on the study objectives and personal judgment.

Validations of CSP plant models with the actual operating data in [52, 71, 87, 113, 123] show that the prediction deviations tend to be higher during the transition periods (e. g. due to start-up, shutdown and clouds) with the daily average of up to 10%.

CSP system complexity makes it difficult to create universal tool which would suit all research purposes. And yet, as shown in [21, 45, 51, 61] there are a number of useful programs developed for performance analysis of the plant or its individual components and processes. Among the free software tools are: Tonatiuh [26] from the National Renewable Energy Center of Spain and SolTrace [111] from NREL for the solar field optical calculations; DNA [46] from Technical University of Denmark for thermodynamic power cycle simulation; and finally, Greenius [40] from DLR and SAM [109] from NREL for the total system performance analysis.

7.1.3 *Solar power modeling in generation system adequacy studies*

The number of studies on generation system adequacy with solar plants is limited as the share of solar power, particularly of CSP, in today's electricity supply is still low. The selected works and their main features on GSA evaluation and solar production modeling are summarized in Table 7.1. A major part of the research focuses on the GSA-based estimation of the capacity contributions from solar power plants. The required reliability indices are usually calculated by using traditional analytical methods and only few studies employ the sequential Monte Carlo technique. Solar power generation values are normally simulated, except for some exceptional cases as in [137] when the actual production series is available.

Study	GSA evaluation method	Solar resource data	Solar plant model
		photovoltaic power	
[54]	analytical	satellite-derived	PVWatts
[162]	analytical	satellite-derived	SAM, PVWatts
[119, 120]	analytical	satellite-derived	PVForm
[115]	analytical	ground measured	Watsun-PV
[90]	analytical	NSRDB	SAM
[74]	analytical	synthetic	simple
[132]	analytical	satellite-derived, TMY	SAM
[137]	analytical	actual monthly operating data	
[80]	analytical	ground measured	simple
[133]	analytical	synthetic	simple
[17]	SMC	synthetic	Watsun-PV
[98, 157]	SMC	synthetic	simple
[42]	non-sequential Monte Carlo	synthetic	simple
		concentrated solar power	
[54, 162]	analytical	satellite-derived	SAM
[89, 91]	analytical	NSRDB	SAM
[152]	SMC	synthetic	simple
[112]	non-sequential Monte Carlo	satellite-derived	SAM

Table 7.1: Selected studies of generation system adequacy with solar power

The input solar radiation for PV and CSP simulations comprises historical, synthetic or typical meteorological year (TMY) data. The historical series, in turn, may originate from various sources. The best approach is, of course, to use direct ground measurements as in the studies for Toronto [115] and Singapore [80]. Since such ground measurements are not always complete or available, it is more common to turn to solar radiation datasets obtained by surface- or satellite-based method. With the surface-based approach the corresponding radiation is calculated from the ground weather measurements by applying meteorological-statistical models. This technique is adopted, for example, in development of the US National Solar Radiation Data Base (NSRDB), which is used in [89–91]. With the satellite-based method, on the other hand, solar radiation is derived from geostationary weather satellites according to the inverse relation between the solar radiation reflected by clouds and atmosphere back to space and the radiation received at the Earth's surface [145, 153]. The advantage of the given approach is more precise representation of the spatial correlation of solar radiation. The satellite-derived radiation data are chosen in [54, 119, 120, 132, 162].

When historical solar radiation values are absent or relatively longer time series is required, researchers turn to synthetic data generation[1]. Among the observed approaches are: addition of random noise to the average values as in [98, 133]; stochastic generation with empirical probability density function as in [157]; and application of the Graham and Aguiar statistical algorithms as in [17, 74] and [152], respectively. Neither of the given methods incorporate the spatial correlation of solar radiation thus limiting the corresponding studies to a single site.

Another option is to use simply the annual solar radiation sequence from TMY which is done, for example, in [132]. TMY represents the concatenation of the data for 12 typical meteorological months selected from the long-term measurements. Its shortcoming is that it characterizes the 'average' local climate and does not include extreme conditions, which are of interest for GSA evaluations.

Conversion of the solar radiation time series to the corresponding power production series is performed with either a detailed simulation tool or a reduced model. In reliability analyses with PV systems both approaches are common as shown in Table 7.1. The simple modeling in this case involves expressing PV power as an entirely linear [80, 133] or partly linear and partly quadratic [74, 98] function of the global solar radiation with the additional ambient temperature correction [157].

In the GSA studies including CSP plants the preference is given to the proper code, namely SAM. A simplified approach is found only in [152], where the production from parabolic trough plant is calculated based on a set of basic equations.

1 See Section 4.1.1 for more details.

7.2 OBJECTIVES AND METHODOLOGY OF PART III

The objective of Part III of the thesis is to develop and validate moderately simplified models of PV, parabolic trough and central receiver based power plants suitable for generation system adequacy studies using the sequential Monte Carlo simulations.

Besides decreasing the overall computational time, the model simplification assumes its generalization, that is, possibility to employ the model with minimum amount of specific knowledge and input data. This aspect is essential as it enables power system planners to evaluate the impact of solar energy without substantial expertise in the underlying physics by focusing only on the key design parameters. In addition, the reduction of input data allows lowering uncertainty of the simulation results and facilitates modeling of future (non-existing) plants for which the technical design details are still unknown.

Considering that the intention is not to improve, but simply adapt the existing approaches, the chosen methodology consists in: (a) review of the most common and detailed techniques available, (b) identification of the factors with negligible or moderate impact on the overall model precision, and (c) application of the selected technique with the simplifications when possible.

The new solar power plant models are implemented in Matlab and validated by using simulations in SAM (version 2013.1.15) as a reference.

8 MODEL OF PHOTOVOLTAIC POWER PLANT

8.1 GENERAL DESCRIPTION

A model of photovoltaic (PV) system is developed for translating the hourly solar radiation to the hourly electricity production from the plant. The overall simulation procedure comprises two steps: calculation of solar radiation on a tilted plane and conversion of incident radiation to net power output.

The required input data are reduced to the following:

- Weather parameters – hourly values of beam I_b and diffuse I_d solar radiation on a horizontal plane, monthly average ambient temperatures $\widehat{T}_{amb}$.
- PV system parameters – total module area A_{pv}, module efficiency at reference conditions $\eta_{pv,src}$, normalized temperature coefficient of the open-circuit voltage β_{Voc}, nominal operating cell temperature (NOCT), total parasitic power losses in PV module and auxiliary components (e. g. inverter, wiring) PL_{pv}.

The reference or standard rated conditions are characterized by the incident total solar irradiance I_{src}=1000 W/m^2 and PV cell temperature $T_{pv,src}$= 25°C, whereas NOCT conditions are defined by the solar irradiance I_{NOCT}= 800 W/m^2 and ambient temperature $T_{amb,NOCT}$=20°C [72].

8.2 ESTIMATION OF SOLAR RADIATION ON A TILTED SURFACE

The total radiation on an inclined plane consists of beam $I_{b,T}$, ground-reflected $I_{g,T}$ and diffuse $I_{d,T}$ components. The first two are defined as [41]:

$$I_{b,T} = I_b \frac{\cos\theta}{\sin\alpha_s}, \tag{8.1}$$

$$I_{g,T} = \rho_g I_{tot} (1-\cos\beta)/2, \tag{8.2}$$

where θ is the incidence angle, α_s is the solar altitude angle, β is the tilt angle, I_{tot} is the hourly total radiation on a horizontal plane, and ρ_g is the ground albedo. The latter, if unknown, can be assumed to be 0.2 [124].

In case of the diffuse component, from available empirical correlations the preference is given to the Reindl expression formulated as:

$$I_{d,T} = \frac{I_d\, I_b\, \cos\theta}{I_o\, \sin\alpha_s} + I_d \frac{1+\cos\beta}{2}\left(1-\frac{I_b}{I_o}\right)\left(1+\sqrt{\frac{I_b}{I_{tot}}}\,\sin^3\frac{\beta}{2}\right) \tag{8.3}$$

where I_o is the extraterrestrial solar radiation on a horizontal plane.

Equations (8.1)–(8.3) together form the Hays-Davies-Klucher-Reindl (HDKR) model, which, as noted earlier, provides a good compromise between accuracy and complexity.

The decrease in the incident solar radiation due to shading of PV arrays, particularly near sunrise and sunset hours, is taken into account using the same procedure adopted during modeling of parabolic trough power plant (see Section 9.2.1 for details). In general, however, the shading loss[1] in PV systems tends to be negligible and often can be ignored, as it affects only the beam component of the incident radiation and is significantly reduced by adequate spacing of PV arrays.

8.3 CONVERSION OF INCIDENT RADIATION TO PV POWER

The incident radiation is translated to PV power by using a reduced form of the 5-parameter model [33, 34]. The adopted assumptions are:

- PV module operates at maximum power point.
- The normalized effective (absorbed) irradiance[2] is equal to the normalized total irradiance incident on a PV array, i. e.

$$I_{eff}/I_{eff,src} = I_T/I_{src} \tag{8.4}$$

  The simplification is justified by the results of comparative study performed in [33].

The combination of the current and voltage equations for the maximum power point from the 5-parameter model together with approximation (8.4) allows defining the gross power of PV plant as:

$$P_{pv} = P_{pv,src}\,\frac{I_T}{I_{src}}\,[1 + \beta_{Voc}(T_{pv} - T_{pv,src})], \tag{8.5}$$

where $P_{pv,src} = A_{pv}\, I_{src}\, \eta_{pv,src}$ is the system gross power output at reference conditions, and T_{pv} is the PV cell temperature. The latter is calculated based on the simplified heat balance according to [72]:

$$T_{pv} = T_{amb} + (NOCT - T_{amb,NOCT})(1 - \eta_{pv,src}/0.9)\frac{I_T}{I_{NOCT}} \tag{8.6}$$

The hourly values of the ambient temperature T_{amb} required for (8.6) are difficult to generate, especially if their correlation with the solar radiation time series has to be taken into account. Considering this, the same daily profile of the ambient temperature is used for each month and it is determined by the following correlation from [47]:

$$\begin{aligned} T_{amb,h} = {} & \widehat{T}_{amb,m} + \Delta\widehat{T}_{amb,m}\,[0.4632\cos(h' - 3.805) \\ & + 0.0984\cos(2h' - 0.360) + 0.0168\cos(3h' - 0.822) \\ & + 0.0138\cos(4h' - 3.513)], \end{aligned} \tag{8.7}$$

1 It should not be confused with the parasitic loss caused by negative electrical effects of partial shadings on a PV array.

2 The radiation absorbed by PV array depends on the incident radiation, air mass, incident angle and PV panel properties. For details of calculation procedure one is referred to [41].

where $h' = 2\pi(h-1)/24$, h is the hour, m is the month, $\widehat{T}_{amb}$ is the monthly mean air temperature, and $\Delta\widehat{T}_{amb}$ is the monthly mean thermal amplitude, i. e. difference between the monthly mean maximum and minimum air temperature values. If not available from weather statistics, the $\Delta\widehat{T}_{amb}$ values are estimated based on the monthly average clearness index $\widehat{KT}_{month}$ according to [47]:

$$\Delta\widehat{T}_{amb} = 25.8\,\widehat{KT}_{month} - 5.21 \tag{8.8}$$

And finally, the net power from PV system is determined by subtracting the parasitic losses, which are assumed to be a fixed percentage of the gross output:

$$P_{pv,net} = P_{pv} - PL_{pv} \tag{8.9}$$

As one can see, the adopted procedure requires only a small amount of readily available input data and a set of simple formulas for predicting PV plant energy output. For comparison, it uses approximately 20 input parameters and 7 equations less than the original 5-parameter model.

The three of the reduced equations are exponential and interrelated [33], which means that they would have to be solved numerically each time the P_{pv} value is evaluated. Considering that during Monte Carlo simulations millions of such calculations are performed, this implies a significant saving in computational effort.

8.4 MODEL VALIDATION

The proposed PV power plant model is implemented in Matlab and validated by using *Sandia PV Array Performance Model* from SAM (version 2013.1.15) as a reference. The simulations are performed for a fictitious PV system at the following 8 locations: Madrid, Seville (Spain), Phoenix (USA), New Delhi (India), Adelaide, Geraldton (Australia), Johannesburg (South Africa) and Antofagasta (Chile). The given sites are chosen to have certain variation in the weather conditions and geographic position. The corresponding climate data are obtained from [151]. For comparison purposes the shading and soiling effects are ignored.

The selected PV cell technologies are single-crystalline (c-Si), poly-crystalline (mc-Si), silicon thin film (Si-film) and triple-junction amorphous (3-a-Si), which are represented by the same brands as in [33]. The required input parameters for each type of PV module are given in Table 8.1. NOCT values are taken from [33] and the remaining parameters are the same as in the corresponding SAM simulation.

The general configuration of the fictitious PV plant is as follows:

- Nameplate capacity – 100 MW
- Array orientation – towards the Equator
- Array tilt angle – equal to latitude
- Parasitic losses – 9.2%

Cell type	Siemens SP-75 (c-Si)	Solarex MSX-64 (mc-Si)	AstroPower APX-90 (Si-film)	Uni-Solar US-64 (3-a-Si)
NOCT [°C]	43.7	43.3	43.0	37.9
$\eta_{pv,src}$ [%]	11.29	10.76	8.34	6.32
β_{Voc} [1/°C]	–0.004158	–0.003774	–0.004384	–0.004131
A_{pv} [m^2]	887470	932426	1202120	1582520

Table 8.1: Input parameters of PV system used in validation study

The simulations are performed on a workstation (Intel Xeon W3503, 12 GB RAM, 2.4 GHz). The average time taken for one-year simulation of individual site is 0.23 seconds, and if needed, it can be reduced further with the code optimization. The comparison with the computational effort required by the reference PV model from SAM could not be done due to rather low execution times and the inherent differences in the code implementation.

Examples of the predicted and reference daily profiles of the incident total radiation and net production in PV plant are given in Fig. 8.1.

The simulation results reveal that the deviations in the monthly and annual values of the incident radiation I_T are less than 0.5%, which allows assuming that the first step of the simulation procedure, estimation of the incident solar radiation, is performed correctly. Considering this, the second calculation step, conversion of I_T to $P_{pv,net}$, is validated by comparing directly the predictions of the plant net production, i. e. by ignoring the difference (if any) between the calculated and reference values of I_T.

The relative deviations in the plant output on an annual and monthly basis are summarized in Table 8.2, which includes the results for the additional simulation series performed by using only the monthly or annual average values of the ambient temperature. The variations of the relative monthly errors for all selected locations are given in Fig. 8.2. The qualitative comparisons of the predictions through cumulative distribution plots are presented in Figs. 8.3–8.6. From these data one can observe that:

- The predictions of the net power are rather close to the reference values in both quantitative and qualitative terms. The average monthly error is in the range of 2–7%, which is comparable to the margin of error of the SAM calculations [20].
- The accuracy of the proposed model reduces with the nominal efficiency of PV cell $\eta_{pv,src}$. One might infer that the precision of the given approach is invariant to the cell technology and is determined mainly by the parameter $\eta_{pv,src}$.
- The deviations on the average exhibit seasonal variation leading to underestimation of the plant production in winter and/or its overestimation in summer for Siemens, Solarex and AstroPower arrays. For Uni-Solar PV cell the trend is inverse.
- The exclusion of the daily and seasonal variations of the ambient temperature reduces the model precision for Siemens, Solarex and AstroPower arrays. The opposite effect is observed in case of Uni-Solar module, which is explained by the partial compensation of individual errors from the adopted modeling simplifications.

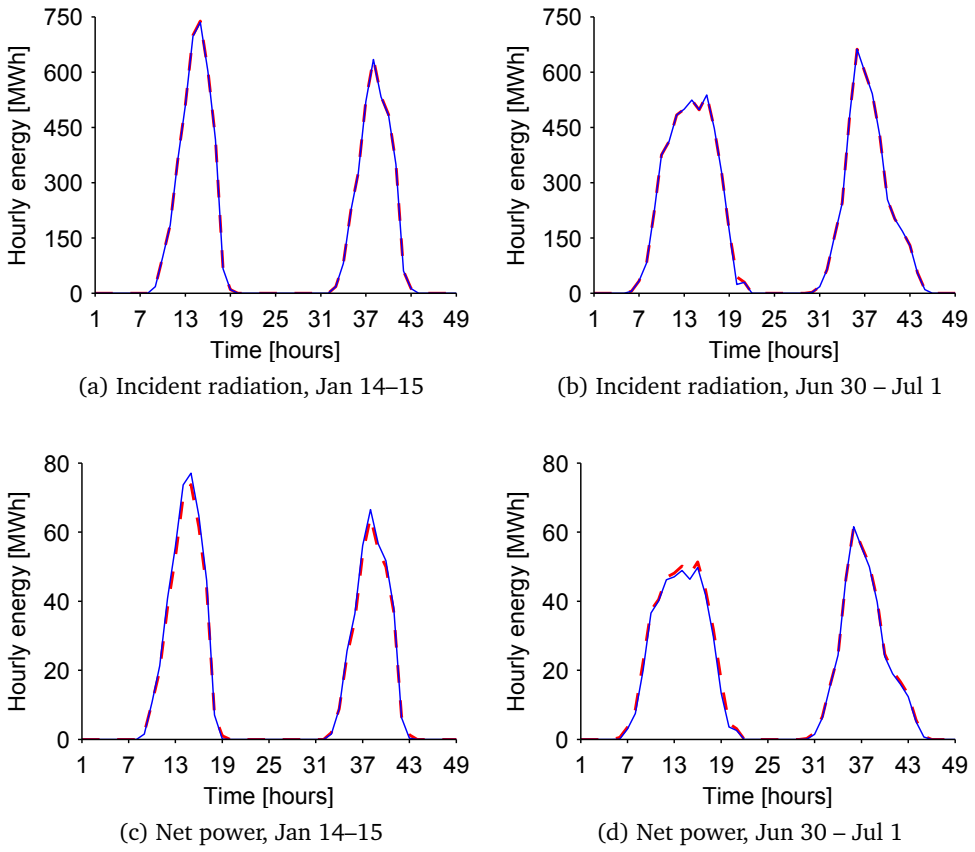

(a) Incident radiation, Jan 14–15

(b) Incident radiation, Jun 30 – Jul 1

(c) Net power, Jan 14–15

(d) Net power, Jun 30 – Jul 1

Figure 8.1: Example of hourly values of the incident radiation and net power of PV plant for selected days (Madrid, Siemens modules)

	Minimum	Maximum	Abs. mean
Annual deviations			
Siemens	–0.8 (+1.0/+1.1)	+5.1 (+7.0/+7.5)	2.0 (3.4/3.7)
Solarex	+0.9 (+2.5/+2.6)	+6.2 (+7.9/+8.3)	3.5 (5.0/5.2)
AstroPower	+1.9 (+3.7/+3.9)	+7.6 (+9.7/+10.2)	5.2 (6.9/7.2)
Uni-Solar	–7.8 (–6.3/–6.3)	–5.0 (–3.3/–2.9)	6.5 (5.1/4.8)
Monthly deviations			
Siemens	–4.1 (–3.1/–6.2)	+7.6 (+9.7/+14.6)	2.6 (3.6/4.6)
Solarex	–1.9 (–1.0/–3.9)	+8.8 (+10.7/+15.3)	3.5 (4.8/5.4)
AstroPower	+1.0 (+2.9/+0.3)	+9.9 (+11.9/+17.4)	5.1 (6.8/6.9)
Uni-Solar	–11.4 (–10.4/–7.9)	+1.0 (+2.4/–0.6)	6.2 (5.0/4.7)

Note: The results in brackets correspond to the additional two simulations. The first is performed by using fixed ambient temperature for each month, and the second simulation is run with the annual average ambient temperature.

Table 8.2: Minimum, maximum and absolute mean deviations (%) in the predicted net production of PV plant

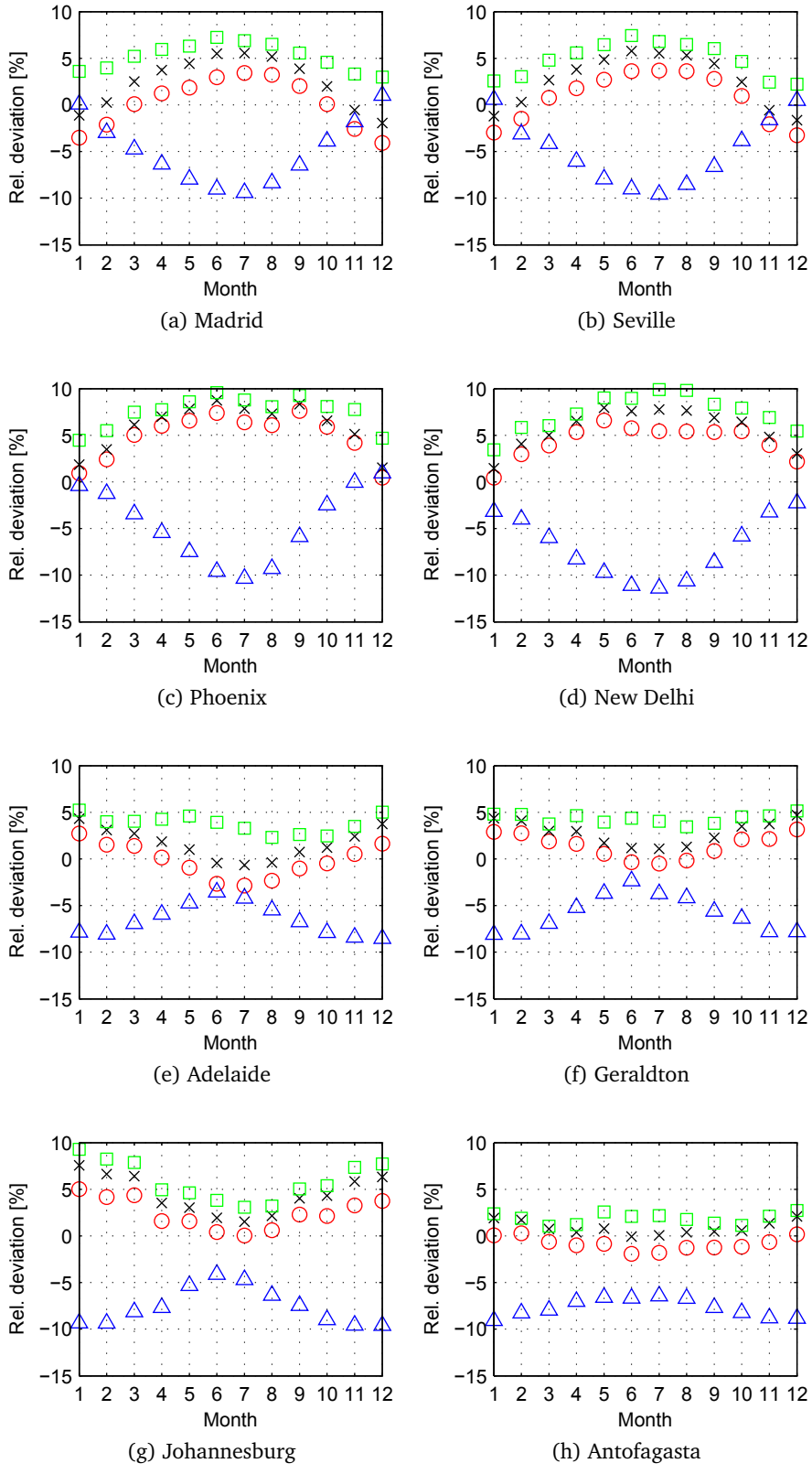

(a) Madrid (b) Seville

(c) Phoenix (d) New Delhi

(e) Adelaide (f) Geraldton

(g) Johannesburg (h) Antofagasta

Figure 8.2: Deviations in predicted monthly net production of PV system at selected sites

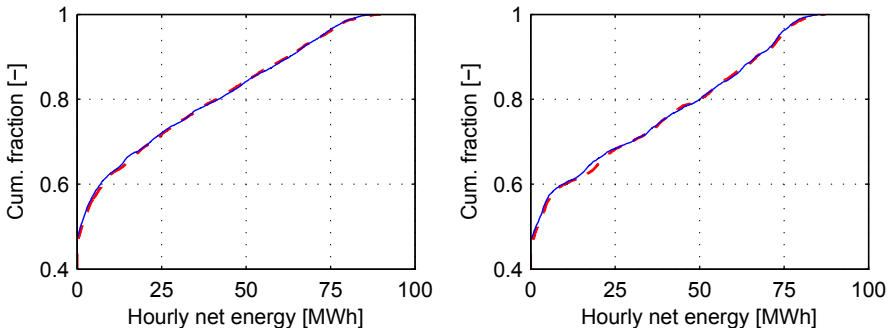

(a) Madrid

(b) Seville

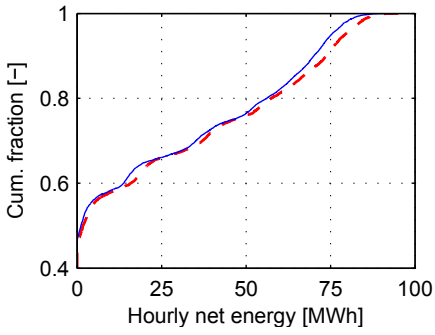

(c) Phoenix

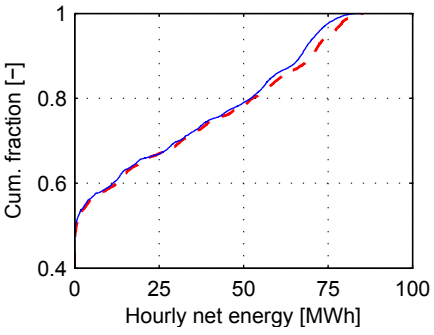

(d) New Delhi

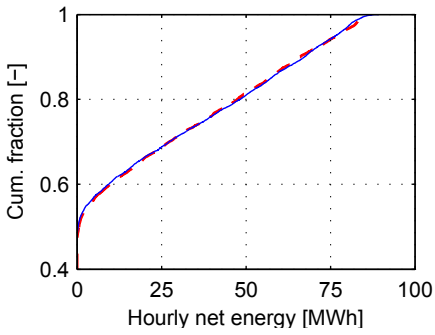

(e) Adelaide

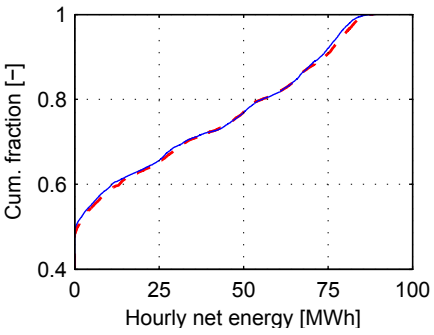

(f) Geraldton

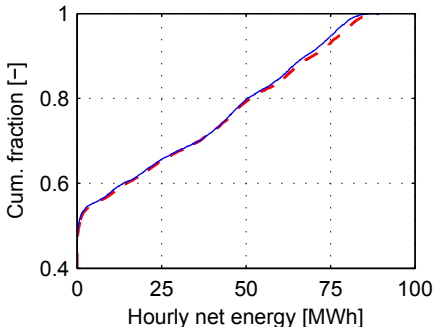

(g) Johannesburg

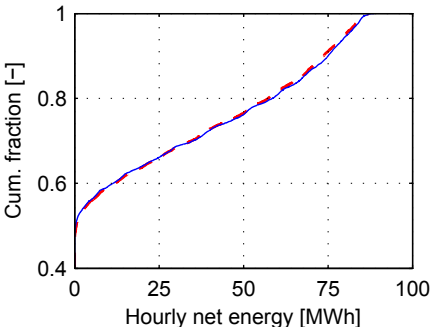

(h) Antofagasta

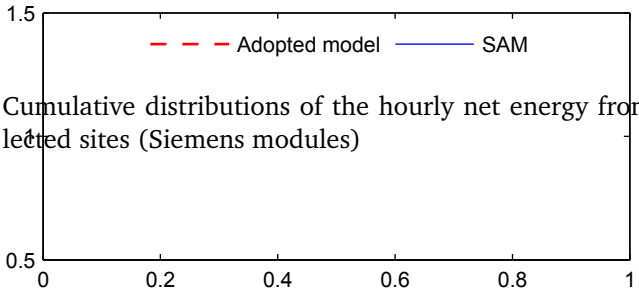

Figure 8.3: Cumulative distributions of the hourly net energy from PV system at selected sites (Siemens modules)

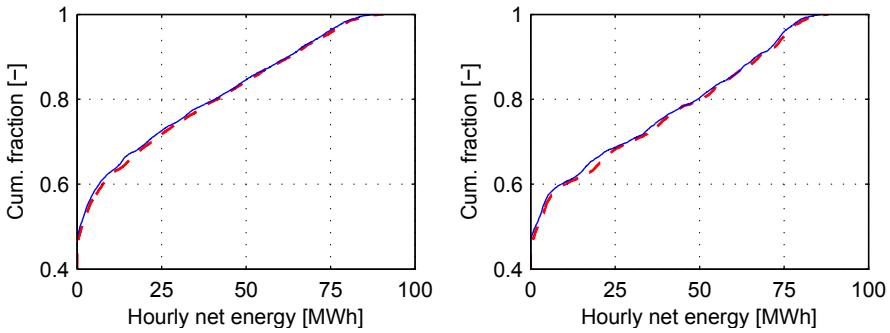

(a) Madrid

(b) Seville

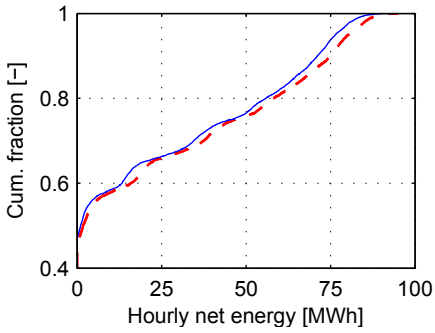

(c) Phoenix

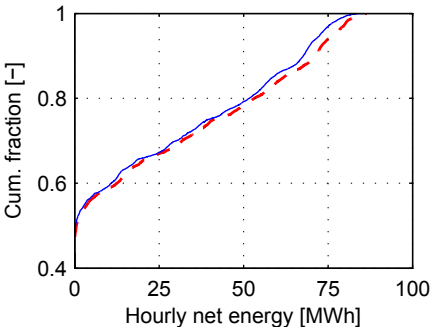

(d) New Delhi

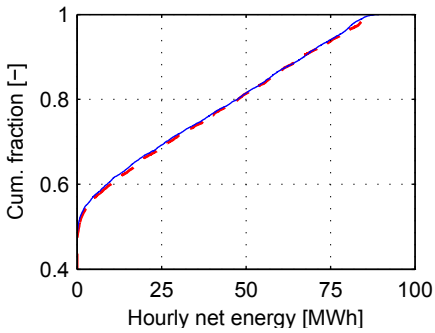

(e) Adelaide

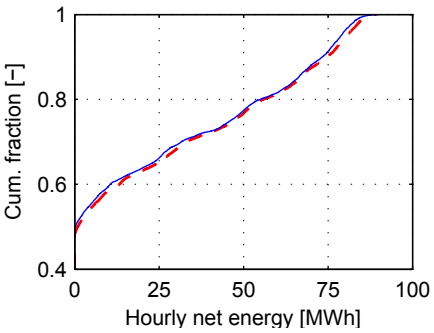

(f) Geraldton

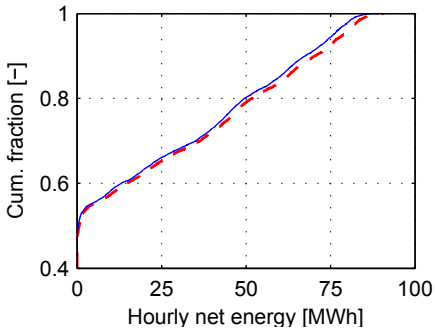

(g) Johannesburg

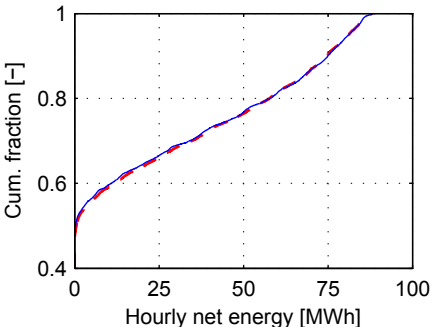

(h) Antofagasta

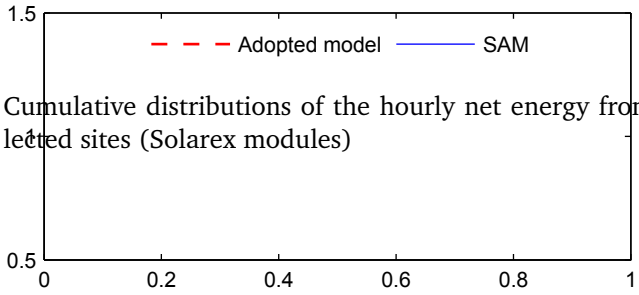

Figure 8.4: Cumulative distributions of the hourly net energy from PV system at selected sites (Solarex modules)

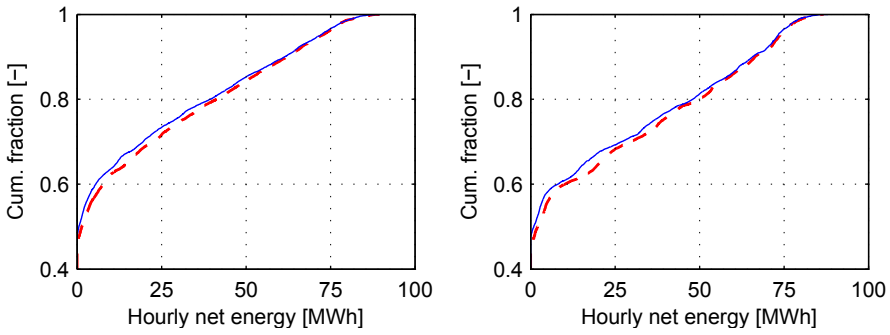

(a) Madrid (b) Seville

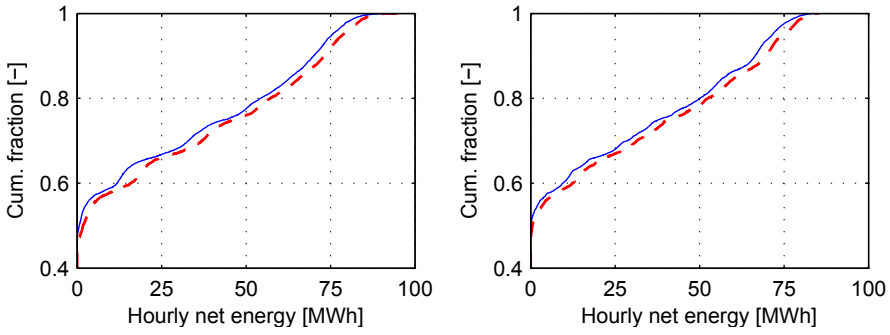

(c) Phoenix (d) New Delhi

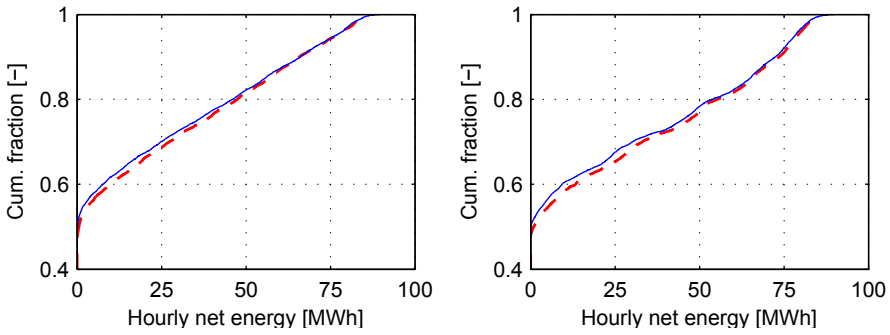

(e) Adelaide (f) Geraldton

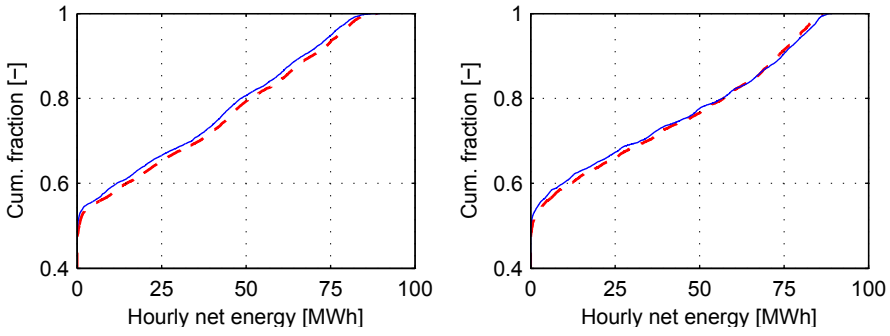

(g) Johannesburg (h) Antofagasta

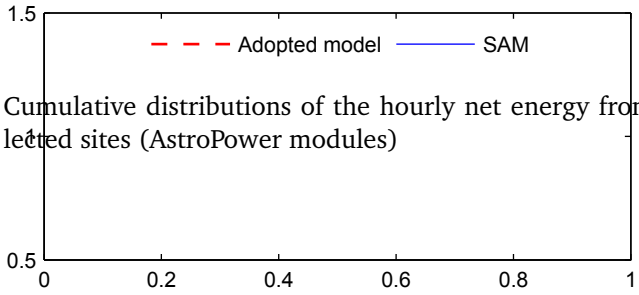

Figure 8.5: Cumulative distributions of the hourly net energy from PV system at selected sites (AstroPower modules)

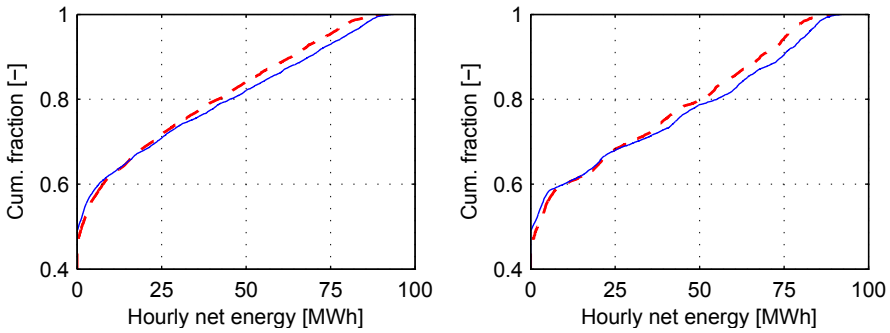

(a) Madrid

(b) Seville

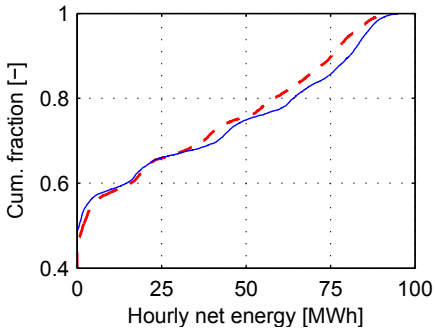

(c) Phoenix

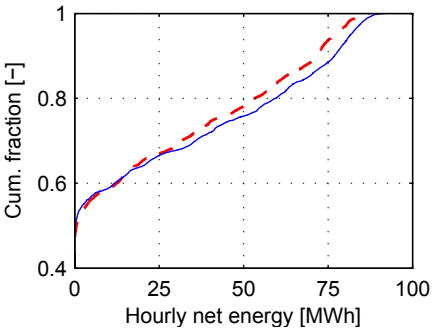

(d) New Delhi

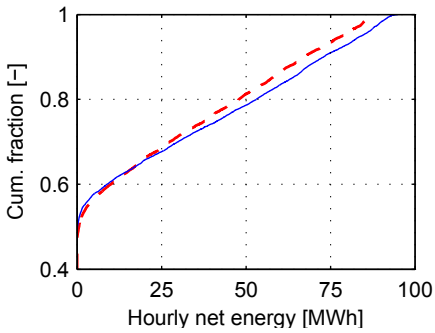

(e) Adelaide

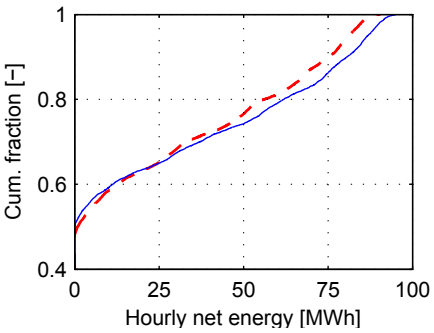

(f) Geraldton

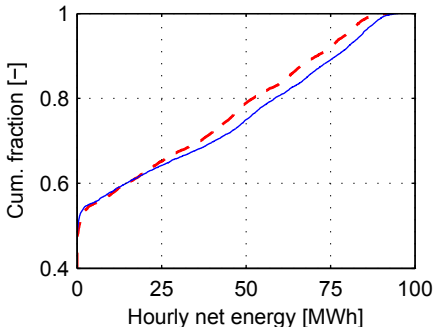

(g) Johannesburg

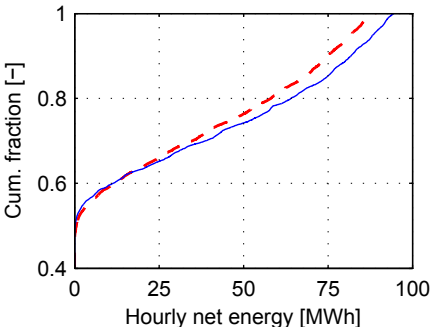

(h) Antofagasta

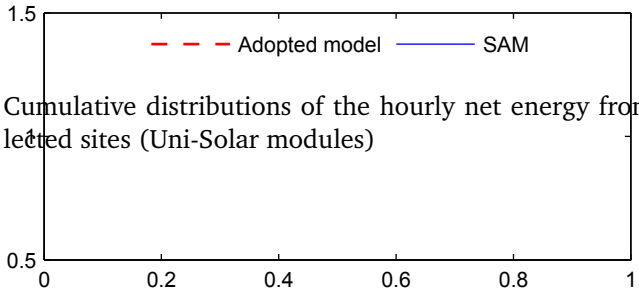

Figure 8.6: Cumulative distributions of the hourly net energy from PV system at selected sites (Uni-Solar modules)

8.5 CONCLUDING REMARKS

A simplified model of PV system was proposed for the application in generation system adequacy studies based on the sequential Monte Carlo technique. The simulation procedure combines the long-established HDKR correlation for calculating solar radiation on a tilted surface and a reduced version of the 5-parameter model for converting the incident radiation to net power output. In comparison, the reduced PV array performance model uses approximately 20 input parameters and 7 equations less than the original 5-parameter model.

The precision of the developed PV system model was validated for multiple case scenarios by using SAM simulations as a reference. The obtained results demonstrated the adequacy of the adopted PV array performance model. In particular, it was shown that:

- The average total deviations in the predicted annual and monthly net production from PV plant are in the range of 2–7%, which is comparable to the margin of error of the SAM calculations.
- The performance of the proposed model to a certain extent is independent of the PV cell technology and is determined mainly by the nominal efficiency of the cell $\eta_{\mathrm{pv,src}}$; the lower is the parameter, the lower is the model precision.
- The exclusion of the daily and seasonal variations of the ambient temperature reduces the model precision, though in some cases the opposite effect is observed as a result of the partial compensation of individual errors from the modeling simplifications.

9 MODEL OF CONCENTRATED SOLAR POWER PLANT

9.1 GENERAL DESCRIPTION

Models of parabolic trough (PTR) and central receiver (tower) systems are developed for translating the hourly direct normal solar radiation to the hourly electricity production. The assumed scheme of concentrated solar power (CSP) plant is shown in Fig. 9.1.

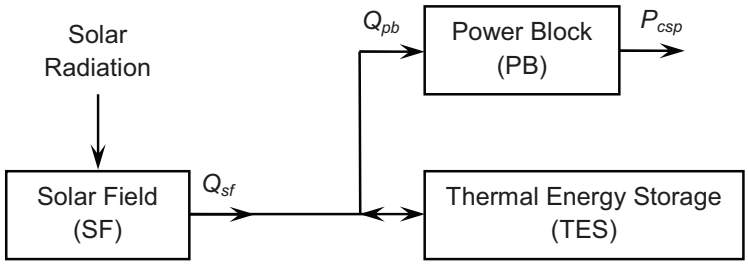

Figure 9.1: Simplified scheme of CSP plant

The overall simulation procedure is divided into three steps: (a) calculation of SF thermal output, (b) PB/TES dispatch and conversion of useful thermal energy to gross power, and (c) estimation of parasitic losses and net production.

The required input data are reduced to the following:

- Common parameters – normal beam radiation $I_{b,n}$; design value of solar radiation $I_{b,des}$; solar field aperture/mirror area A_{sf} or solar multiple SM_{csp} (the ratio of SF and PB thermal outputs at design conditions); solar field warm-up energy $Q_{sf,warm}$; total thermal energy loss in receiver $Q_{rec,loss}$; adjustment for other energy losses in solar field $\eta_{sf,other}$; power block nominal gross output $P_{csp,nom}$, efficiency $\eta_{pb,nom}$ and required thermal start-up power $Q_{pb,start}$; TES round-trip efficiency η_{tes} and capacity defined by the equivalent full load hours T_{tes}; plant nominal parasitic power losses; plant dispatch limits.
- Parabolic trough system – collector maximum optical efficiency $\eta_{ptr,max}$ and solar field density (the ratio of the collector aperture area to the field land area).
- Central receiver system – tower height h_{tower}; maximum d_{hel}^{max} and minimum d_{hel}^{min} heliostat distance to tower; heliostat mirror width w_{hel} and height h_{hel}; the additional parameter describing the North-South asymmetry of the heliostat field ΔY_{ab}; heliostat reflectivity $\eta_{hel,refl}$; receiver efficiency based on absorptivity $\eta_{rec,abs}$ and spillage $\eta_{rec,spill}$.

The details of the calculations and underlying simplifications are described below.

9.2 SOLAR FIELD

Solar field in CSP plant converts the incident direct radiation to the useful thermal energy. In PTR system SF is the field of parabolic troughs and in tower plant it represents central receiver and heliostat field surrounding it.

Before initiating the SF thermal production in the morning, heat transfer fluid (HTF) first has to be warmed up to the operating temperature. In the adopted model the SF warm-up process is simulated simply by counting the warm-up energy absorbed by HTF (and dissipated to the ambient) at subsequent intervals until, in total, the required fixed value $Q_{sf,warm}$ is reached. Compared to tower plant, the warm-up stage in PTR system tends to be longer and may have notable impact on the power production level, especially in winter. This is explained, firstly, by higher value of $Q_{sf,warm}$ as a result of larger ambient heat losses from parabolic troughs dispersed around SF; and secondly, by less efficient collection of the solar energy with the single-axis solar tracking at low sun elevations [41].

Once the warm-up is completed, SF starts delivering thermal power which is defined as:

$$Q_{sf} = \eta_{sf} A_{sf} I_{b,n} \tag{9.1}$$

The accurate evaluation of the missing SF efficiency η_{sf} is rather difficult task as it requires detailed heat transfer and optical calculations. In this work by assuming constant HTF temperature, negligible variation in the ambient temperature and thus assuming constant thermal losses in the receiver $Q_{rec,loss}$, the following simplified formula is applied [144]:

$$\eta_{sf} = \left(\eta_{sf,opt} - \frac{Q_{rec,loss}}{A_{sf} I_{b,n}}\right) \eta_{sf,other}, \tag{9.2}$$

where $\eta_{sf,opt}$ is the SF optical efficiency and it is calculated differently depending on the concentrating technology employed.

The use of (9.2) is justified because: (a) it is not uncommon practice in the CSP plant control to keep the solar fluid outlet temperature constant [100, 109], and (b) the operating temperatures in the concentrating collectors tend to be significantly higher than the ambient air temperatures. It can be argued, however, that the given approximation is less suitable for PTR system with its relatively low HTF temperatures [72, 144]. Considering this, an additional study has been performed by modeling thermal loss in the trough field as a function of the HTF and ambient temperatures, and according to the results the alternative approach showed negligible impact on the overall prediction accuracy (see Appendix A).

One should note that (9.2) ignores the variations in other weather parameters besides the ambient temperature (e. g. wind velocity and direction). Even though this aspect has not been investigated directly, the results from the validation study imply that such simplification is acceptable.

9.2.1 *Optical efficiency for parabolic trough system*

SF performance in PTR system can be considered homogeneous as a result of even distribution of the troughs and identical conversion process of solar radiation to thermal energy throughout the field. This allows modeling SF as one equivalent PTR and define its optical efficiency as follows:

$$\eta_{sf,opt} = \eta_{ptr,max} \times \cos\theta \times \text{IAM} \times \eta_{shbl}, \tag{9.3}$$

where θ is the incidence angle and it depends on the sun tracking mechanism employed; IAM is the incidence angle modifier taking into account additional degradation of the collector optical performance with non-zero incidence angle; and η_{shbl} is the efficiency due to mutual shadowing and blocking of the collectors.

IAM is usually defined by empirical correlations. For example, for collectors Luz-2, Luz-3 and EuroTrough-150 it can be expressed as [109, 155]:

$$\text{IAM} = 1 + 0.000884\,\frac{\theta}{\cos\theta} - 0.0000536\,\frac{\theta^2}{\cos\theta} \tag{9.4}$$

The efficiency due to the collector shadowing is of importance at early and late hours of the day and is estimated according to [144]:

$$\eta_{shbl} = \frac{\sin\alpha_s}{\text{SF density} \times \cos\theta}, \tag{9.5}$$

where α_s is the solar altitude angle. Interestingly, (9.5) gives the expression proposed in [155], if the SF density is approximated by the ratio of collector aperture width to spacing between troughs and certain trigonometric manipulations are carried out.

9.2.2 *Optical efficiency for tower system*

In central receiver systems the optical performance varies with the heliostat position and therefore the evaluation of $\eta_{sf,opt}$ requires taking into account the layout of heliostat field.

Owing to large number of heliostats the calculations normally are performed only for a set of field points, which are assumed to represent the average performance in a surrounding zone of heliostats. In DELSOL code [78], which is used by SAM for heliostat field calculations, these zones are specified by splitting the field around the tower in radial and tangential directions as shown in Fig. 9.2a. Note that the first and the last radial steps in the field zoning are twice less than the others. The heliostat field absolute boundaries are two concentric circles with radii d_{hel}^{max} and d_{hel}^{min}. The main parameters of individual field zone are the number of heliostats within its boundaries $N_{hel,z}$ and the centre position defined by the Cartesian coordinates (x_{hel}, y_{hel}) according to Fig. 9.2b.

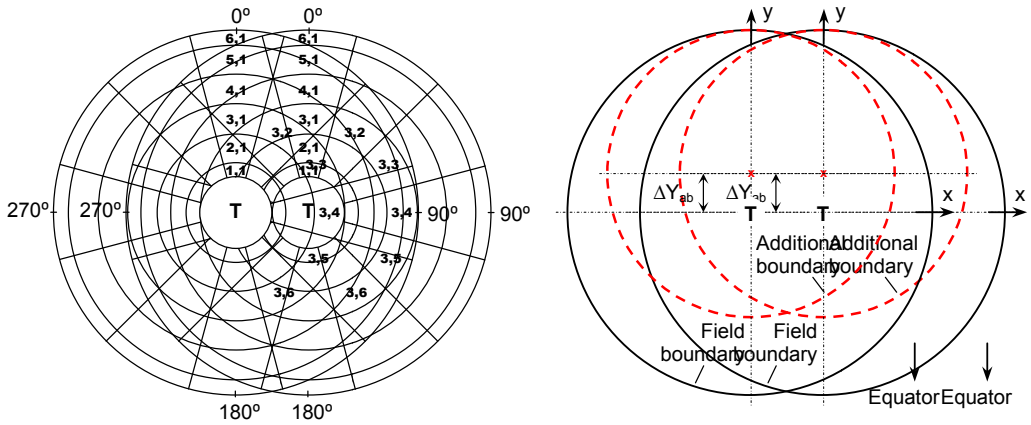

(a) Field zoning (based on [78])

(b) Modeling field asymmetry

Figure 9.2: Heliostat field layout

In this work the same approach for heliostat field zoning is adopted, but the heliostat numbers are expressed in normalized terms by $N^*_{hel,z}$, which directly reflects the relative contribution of individual segment to the SF optical performance. A simplified procedure for creating the heliostat field layout and calculating $N^*_{hel,z}$ will be described as follows.

Once the relative distribution of heliostats is known, the average optical efficiency of central receiver system can be determined by considering the main losses according to [144, 154]:

$$\eta_{sf,opt} = \sum_{z}^{*} \left(\cos\theta_{hel} \times \eta_{hel,atm} \times N^*_{hel,z} \right) \times \eta_{hel,refl} \times \eta_{rec,refl} \times \eta_{rec,spill} \times \eta_{shbl}, \tag{9.6}$$

where

θ_{hel} is the heliostat incidence angle varying with the solar altitude α_s and solar azimuth γ_s angles as

$$\cos 2\theta_{hel} = \left[(h_{tower} - h_{hel}) \sin\alpha_s - x_{hel} \cos\alpha_s \sin(\gamma_s + 180) - y_{hel} \cos\alpha_s \cos(\gamma_s + 180) \right] / d_{hel}, \tag{9.7}$$

$\eta_{hel,atm}$ is the heliostat efficiency due to atmospheric attenuation that is usually approximated by a polynomial of d_{hel}, the distance in km between the given heliostat and receiver. For example, for a visibility of 23-km one of the correlations is

$$\eta_{hel,atm} = 1 - 0.01\,(0.6739 + 10.46\,d_{hel} - 1.7\,d^2_{hel} + 0.2845\,d^3_{hel}) \tag{9.8}$$

$\eta_{rec,refl}$ is the receiver surface reflectivity, which in turn can be expressed as $\eta_{rec,refl} = 0.957\,\eta_{rec,abs}$. The value 0.957 represents the assumed average attenuation of the receiver absorptivity with non-zero incidence angle of the radiation striking the surface [154].

Similar to PTR system, the efficiency due to shadowing and blocking in heliostat field is of high importance at early and late hours of the day. As its estimation in general requires rather complex geometric calculations and detailed description of the field layout, the following simplified correlation is proposed instead:

$$\eta_{shbl} = 5.52 \sin \alpha_s - 12.66 \sin^2 \alpha_s + 15.13 \sin^3 \alpha_s - 9.46 \sin^4 \alpha_s + 2.47 \sin^5 \alpha_s \quad (9.9)$$

The polynomial (9.9) is obtained based on the SAM predictions. Since in the SAM simulation results the average shadowing efficiency is not available, the reference values are estimated as:

$$\eta'_{shbl} = \frac{[\eta_{sf,opt}]^*_{SAM}}{[\eta_{sf,opt}/\eta_{shbl}]^*}, \quad (9.10)$$

where $[\eta_{sf,opt}]^*_{SAM}$ is the normalized SF optical efficiency predicted by SAM and $[\eta_{sf,opt}/\eta_{shbl}]^*$ is the corresponding value, but with zero shadowing losses obtained from the developed model. The normalization in this case is required for comparability reasons.

Interestingly, the values of η'_{shbl} and $\sin \alpha_s$ from all simulated case scenarios exhibit a piecewise-linear pattern as shown in Fig. 9.3. The approximation (9.9) has been derived by fitting a polynomial with zero intercept to the breakpoints of the data segments and by additional manual adjustments to achieve monotonic increase in the range of 0 to 1. The goodness-of-fit of the chosen correlation is considered acceptable. For example, for the reference data presented in Fig. 9.3 the coefficient of determination R^2 is 0.98 and the root-mean squared error is 0.018.

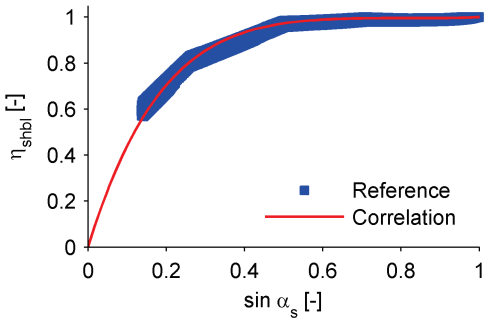

Figure 9.3: Shadowing and blocking efficiency of heliostat field versus solar altitude angle. The reference data (> 60.000 points) are from 16 case scenarios used in the validation study.

Generation of heliostat field layout

The layout of heliostat field is basically characterized by relative distribution of heliostats throughout the specified field zones, i.e. by $N^*_{hel,z}$, the missing parameter in (9.6). The existing methods and codes for creating heliostat field layouts usually require rather detailed description of the field and involve complex iterative calculations. Considering this, an alternative simplified procedure is proposed to determine $N^*_{hel,z}$ which consists of the following steps:

1. The optimal radial ΔR_{hel} and azimuthal ΔA_{hel} spacing (m) of heliostats is calculated for each zone according to [144]

$$\alpha_{hel} = \tan^{-1} \frac{h_{tower} - h_{hel}}{(x_{hel}^2 + y_{hel}^2)^{0.5}} \quad \text{(radians)} \tag{9.11}$$

$$\Delta R_{hel} = h_{hel} \left(1.44 \cot \alpha_{hel} - 1.094 + 3.068\, \alpha_{hel} - 1.1256\, \alpha_{hel}^2\right) \tag{9.12}$$

$$\Delta A_{hel} = w_{hel} \left(1.749 + 0.6396\, \alpha_{hel}\right) + \frac{0.2873}{\alpha_{hel} - 0.04902} \tag{9.13}$$

2. The corresponding values of the solar field density are estimated

$$\text{SF density} = \frac{2\, h_{hel}\, w_{hel}}{\Delta R_{hel}\, \Delta A_{hel}} \quad (-) \tag{9.14}$$

3. The number of heliostats in each zone z is determined based on the zone area A_{fzone} and heliostat mirror dimensions

$$N_{hel,z} = \frac{\text{SF density} \times A_{fzone}}{h_{hel}\, w_{hel}} \tag{9.15}$$

   If the north-south asymmetry is required, then an additional boundary is applied as shown in Fig. 9.2b. The field segments lying outside the given boundary are ignored, i. e. $N_{hel,z} = 0$.

4. And finally, the normalization is applied

$$N_{hel,z}^{*} = \frac{N_{hel,z}}{\sum_z N_{hel,z}} \tag{9.16}$$

The given approach in relative terms allows creating the field layout of reasonable quality. This is demonstrated in Fig. 9.4 comparing the calculated relative distribution of heliostats in radial[1] direction with that obtained from SAM.

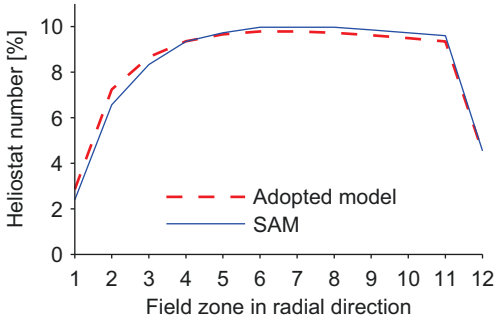

Figure 9.4: Radial distribution of heliostats obtained with 12 radial and azimuthal field zones. Data from the validation study (SM_{csp}=2.5).

1 The tangential spacing of the heliostats obtained by (9.13) is almost uniform.

9.3 POWER BLOCK AND THERMAL STORAGE

Power block in CSP plant uses the conventional Rankine cycle to generate electricity. Full simulation of the cycle consists of rather involved thermodynamic and heat transfer calculations. In order to reduce the computational effort the related simulation tools often employ a regression model, as for example in SAM [155], which provides adequate accuracy but still requires definition of certain design parameters.

In this study a basic heat-to-power model is employed and PB input data are reduced to minimum: the block nominal power $P_{csp,nom}$, efficiency $\eta_{pb,nom}$, the required thermal start-up power $Q_{pb,start}$ and the loading limits. PB start-up is assumed to be completed within an hour and consume the fixed amount of thermal energy equal to $Q_{pb,start}$. Once PB is started the conversion of the thermal energy Q_{pb} supplied by SF/TES to the gross power is done as follows:

$$P_{csp} = \eta_{pb,nom} \times \eta^*_{pb} \times Q_{pb}, \tag{9.17}$$

where η^*_{pb} is the PB normalized efficiency, which based on the results from [100] is approximated by the polynomial of the relative loading L_{pb} (the ratio of the PB thermal power input Q_{pb} to its nominal value $Q_{pb,nom}$)

$$\eta^*_{pb} = 0.5492 + 1.1273\, L_{pb} - 1.0463\, L^2_{pb} + 0.3705\, L^3_{pb} \tag{9.18}$$

Thermal energy storage, an optional component of CSP system, has a significant influence on the plant operation. Here it is represented simply as a single volume tank with the capacity T_{tes} and round-trip efficiency η_{tes}. The (dis)charge limit is determined by the PB nominal thermal power $Q_{pb,nom}$.

9.4 PLANT CONTROL

The control strategy is the most important aspect in CSP plant simulation. It ensures that the system components operate within specified limitations and determines how and when each component is dispatched.

The hourly control logic implemented in the new CSP models is similar to that described in [154, 155], though certain modifications are applied considering the adopted modeling and programming approach. The general dispatch scheme depending on the on/off state of SF and PB is shown in Fig. 9.5. As one can see the control is performed in terms of power and energy, whereas in the actual CSP plant the control parameters would also include mass flow rates and temperatures of the working fluids. The main aspects of the selected dispatch strategy are summarized below:

- The SF warm-up and normal operation requires beam radiation larger than $I_{sf,min}$, which is estimated based on the minimum allowed thermal output of solar field:

$$I_{sf,min} = \frac{Q_{sf,min}}{\eta_{sf} A_{sf}} \tag{9.19}$$

  If at any timestep the radiation falls below the allowed minimum, SF is shut down and/or the warm-up starts from the beginning.

- The SF warm-up can take more than one hour and it is completed once the required thermal energy $Q_{sf,warm}$ is delivered.

- PB can be started only when SF is on. The start-up is accomplished always within one hour and consumes $Q_{pb,start}$ thermal power from SF/TES. If PB cannot be started, SF charges TES.

- When PB is on, it is supplied first by SF (if operating) and then TES. If the available SF/TES power is less than the required minimum $Q_{pb,min}$, PB is shut down.

- The SF thermal power that could not be delivered to PB/TES is considered as a spilled power.

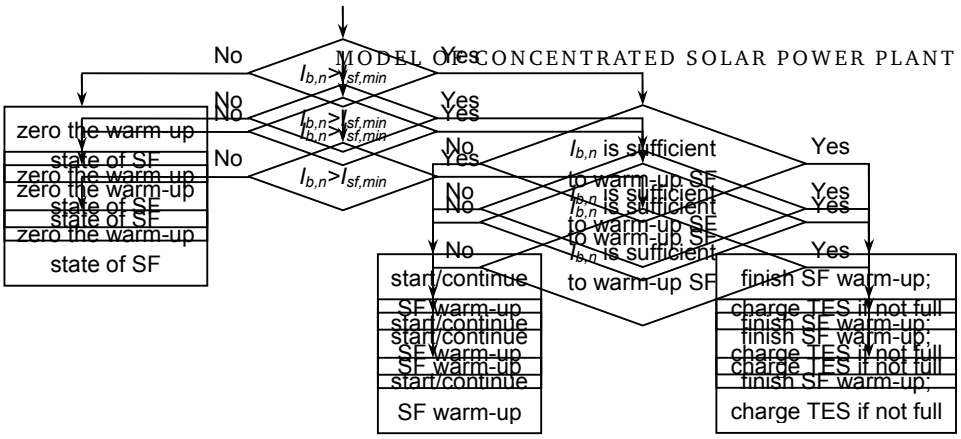

(a) SF – off, PB – off

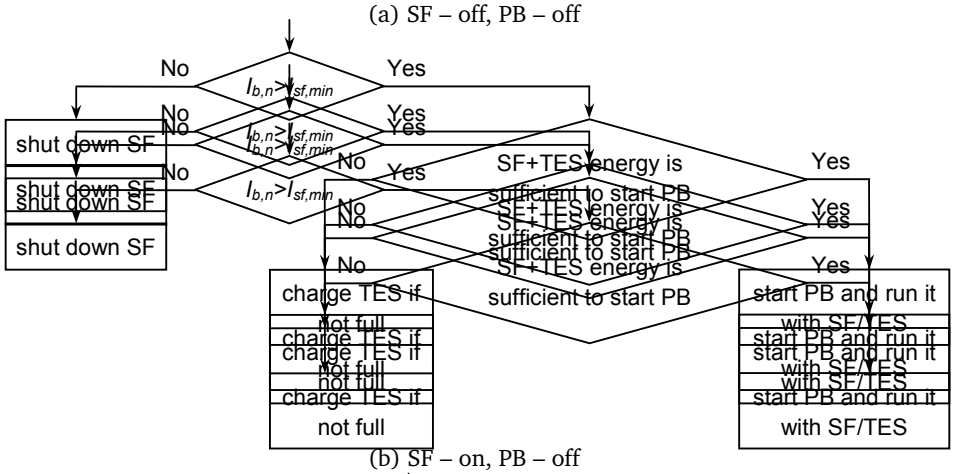

(b) SF – on, PB – off

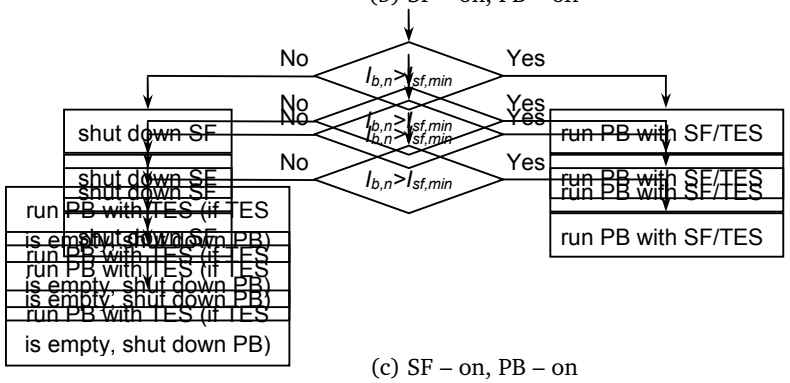

(c) SF – on, PB – on

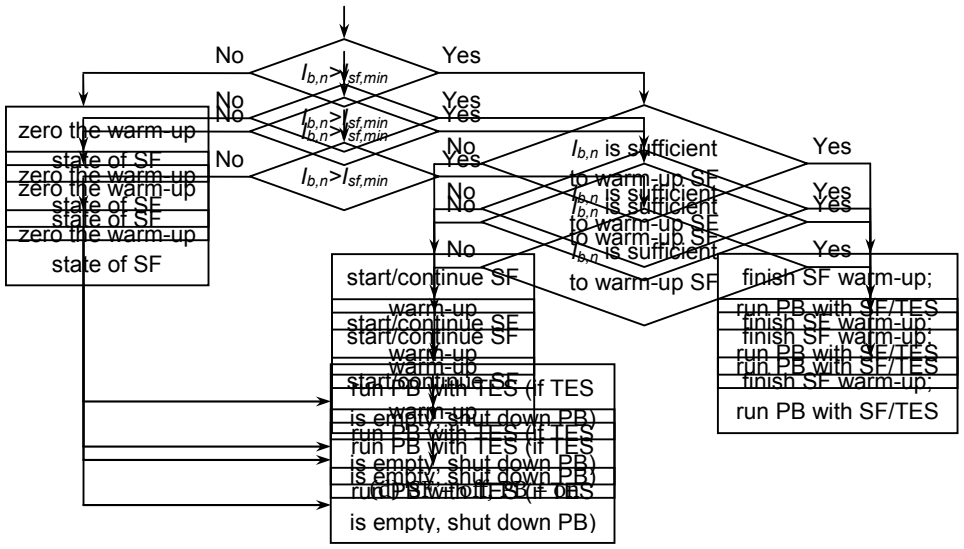

Figure 9.5: Dispatch strategy of CSP plant at various scenarios

9.5 PARASITIC LOSSES AND NET POWER

Parasitic losses in CSP plant PL_{csp} refer to the fraction of the gross power consumed by the plant for its own use, which on average can be up to 10–15% [155]. In this work the total parasitic losses at each time interval are estimated as:

$$\begin{aligned} PL_{csp} =& PL_{csp,fix} + PL_{csp,track} + PL_{csp,night} \\ &+ PL_{csp,p1} + PL_{csp,p2} + PL_{csp,other}, \end{aligned} \tag{9.20}$$

where

$PL_{csp,fix}$ is the fixed loss, independent of the system operation

$PL_{csp,track}$ is the fixed loss due to sun tracking applied during the daytime

$PL_{csp,night}$ is the fixed loss applied during the nighttime (e. g. antifreeze protection)

$PL_{csp,p1}$ is the variable loss due to HTF pumping through SF

$$PL_{csp,p1} = PL^{des}_{csp,p1} \left[\frac{Q_{sf}}{Q_{sf,des}} \right]^3 \text{ (PTR)} \tag{9.21}$$

$$PL_{csp,p1} = PL^{des}_{csp,p1} \frac{Q_{sf}}{Q_{sf,des}} \text{ (tower)} \tag{9.22}$$

$PL_{csp,p2}$ is the variable loss due to HTF pumping through PB and TES

$$PL_{csp,p2} = PL^{des}_{csp,p2} \frac{Q_{pb} + |Q_{tes}|}{Q_{sf,des}} \tag{9.23}$$

$PL_{csp,other}$ is the variable loss in other components (e. g. cooling tower) linked to the power production

$$PL_{csp,other} = PL^{des}_{csp,other} \frac{P_{csp}}{P_{csp,nom}} \tag{9.24}$$

As one can see the variable losses are calculated by scaling the parameters which have the highest influence on them: the SF thermal output, total absolute thermal flow within PB/TES and gross power. The input parameters $PL^{des}_{csp,p1}$, $PL^{des}_{csp,p2}$ and $PL^{des}_{csp,other}$ in this case represent the reference values of the given parasitic losses.

The assumed relation of the pumping losses to the corresponding thermal power flows in equations (9.21)-(9.23) has the following explanation. The energy required for pumping the given fluid theoretically is equal to the product of the volumetric flow rate and the pressure drop, where the latter, in turn, varies approximately with square of the flow rate. Thus, when the pressure drop is notable (as in case of PTR field) the pumping work has cubic relation to the flow rate and if the pressure drop is negligible, the relation can be considered linear. Assuming that in CSP plant HTF density and temperature

during the operation is constant, the volumetric flow rate can be substituted by the corresponding thermal power flow.

The net production delivered by CSP system to the grid is determined simply by subtracting the total parasitic losses of the plant from the gross power, i. e.

$$P_{csp,net} = P_{csp} - PL_{csp} \tag{9.25}$$

9.6 MODEL VALIDATION

9.6.1 *Input data*

The proposed CSP plant models are implemented in Matlab and validated by using *physical trough* and *tower molten salt* models from SAM (version 2013.1.15) as a reference. The simulations are performed for a fictitious CSP system at the following 8 locations: Madrid, Seville (Spain), Phoenix (USA), New Delhi (India), Adelaide, Geraldton (Australia), Johannesburg (South Africa) and Antofagasta (Chile). The given sites are chosen to have certain variation in the weather conditions and geographic position. The corresponding climate data are obtained from [151]. In order to test the model performance at various sizes of solar field and thermal storage, the following two scenarios are considered: SM_{csp}=2, T_{tes}=6 and SM_{csp}=2.5, T_{tes}=15.

The selected input parameters of CSP plant are summarized in Table 9.1. For comparability reasons the values of A_{sf} are taken directly from SAM, though in general the SF sizing is done based on the design operating conditions. As a result of the SAM heliostat field optimizations A_{sf} for tower system varies slightly with the site location. In case of PTR plant the site-dependent parameter is the SF warm-up energy $Q_{sf,warm}$ which is obtained by averaging the data from the SAM calculations; the lower and upper limits of the shown range correspond to Phoenix and Geraldton, respectively. The power block start-up time in SAM simulations is taken to be 0.5 hours.

It is important to note that in CSP plant definition SAM employs a large number of additional technical parameters that are not required in the developed simplified models. In this study SAM default values are used for these parameters and the resultant impact (if any) is ignored.

	PTR	Tower
	Common parameters	
$I_{b,des}$	900 W/m^2	950 W/m^2
A_{sf}	909060 m^2 (1137960)	1010479–1046140 m^2 (1296341–1331713)
$Q_{sf,warm}$	247–256 MWh (325–337)	25% $Q_{sf,des}$
$Q_{sf,min}$	—	25% $Q_{sf,des}$
$Q_{rec,loss}$	6% $Q_{sf,des}$	6.5% $Q_{sf,des}$
$\eta_{sf,other}$	100%	100%
$P_{csp,nom}$	111 MW	111 MW
$\eta_{pb,nom}$	37.74%	41.2%
$L_{pb,min}$	25%	25%
$Q_{pb,start}$	20% $Q_{pb,nom}$	50% $Q_{pb,nom}$
η_{tes}	99.7%	99.7%
$PL_{csp,fix}$	0.55% $P_{csp,nom}$	0.55% $P_{csp,nom}$
$PL_{csp,track}$	0.26% $P_{csp,nom}$	0.35% $P_{csp,nom}$
$PL_{csp,night}$	—	—
$PL^{des}_{csp,p1}$	5% $Q_{sf,des}$	1.6% $Q_{sf,des}$
$PL^{des}_{csp,p2}$	0.3% $Q_{sf,des}$	0.13% $Q_{sf,des}$
$PL^{des}_{csp,other}$	1.9% $P_{csp,nom}$	4% $P_{csp,nom}$
	Specific data	
	EuroTrough 150 collector	$h_{hel}=w_{hel}=12.2$ m
	Schott 2008 PTR70 receiver	$h_{tower}=183.3$ m (203.3)
	Horizontal N-S axis	$\Delta Y_{ab}=0$–160 m
	SF density =0.383	$0.75h_{tower} \leqslant d_{hel} \leqslant 7.5h_{tower}$
	$\eta_{ptr,max}=74.2\%$	$\eta_{rec,abs}=94\%$, $\eta_{rec,spill}=98\%$

Note: The values for the case $SM_{csp}=2.5$ are given in brackets.

Table 9.1: Input data of CSP plant used in validation study

9.6.2 *Results and discussion*

The performance of the new CSP models is analyzed primarily based on the annual and monthly prediction deviations and cumulative distributions of the net electrical output. The individual errors for each of the three calculation steps ($I_{b,n} \Rightarrow Q_{sf} \Rightarrow P_{csp} \Rightarrow P_{csp,net}$) are also estimated. In case of the monthly predictions the focus is centered on the summer period when most of the power is produced by CSP system. The execution speed is tested by running the developed codes on a workstation (Intel Xeon W3503, 12 GB RAM, 2.4 GHz); the corresponding simulation time in SAM is estimated by using Windows Performance Monitor.

Examples of the predicted and reference daily profiles of the incident radiation ($A_{sf} \times I_{b,n}$), the SF output and net power are given in Fig. 9.6.

The relative deviations in the predicted SF output, gross and net power production on an annual and monthly basis are summarized in Tables 9.2 and 9.3. The variations in the relative monthly errors for the main parameters and the selected locations are shown in Figs. 9.7–9.10. The cumulative distributions of the hourly net production values are compared in Figs. 9.11–9.14.

During PTR model validation the calculations were also performed for the case of Luz-3 collector and Solel UVAC3 receiver, and though not presented in this thesis rather similar outcomes were obtained.

When looking at the results it is important to bear in mind that: (a) the prediction deviations are caused not only by the adopted model reductions, but also by inherent differences between the modeling approaches implemented in this work and SAM; (b) the detailed description of CSP system components provided by SAM models is advantageous, yet it also adds more uncertainty to performance predictions [109].

The main observations and conclusions from the validation study are as follows:

- The plant thermal Q_{sf} and electrical P_{csp} outputs estimated by the reduced CSP models deviate from the reference values in an irregular pattern (Figs. 9.7–9.10). And the reason is that the individual errors from the involved multiple modeling simplifications vary depending on the plant configuration, site location and the weather conditions.

- The errors in the first calculation step $I_{b,n} \Rightarrow Q_{sf}$ determine the general trend in the distribution of the monthly deviations, which indicates the importance of the solar field calculations (Figs. 9.7–9.10). The proposed methods for estimating SF production appear to be adequate (Table 9.2). On average, the precision of tower-based SF model is somewhat lower, which can be attributed to simplified heliostat field calculations. Yet, in certain cases trough-based SF model may give larger deviations and it is explained by the use of simplified approach to model SF warm-up process, which may have high impact on PTR field output, particularly in winter.

- The accuracy of the adopted power block model (the conversion step $Q_{sf} \Rightarrow P_{csp}$) is higher than that of the solar field model. For PTR system simulations the corresponding errors are slightly larger as the implemented PB start-up procedure performs worse in this case (Table 9.2).

- The deviations in the estimated parasitic losses (the step $P_{csp} \Rightarrow P_{csp,net}$) are the lowest, and as expected they depend on the precision of the previous calculation steps (Table 9.2, Figs. 9.7–9.10).

- The implemented control logic allows acceptable imitation of the plant hourly dispatch. As expected, relatively larger mismatch is observed during the SF/PB start-up, particularly when solar elevation or radiation is low (Fig. 9.6).

- The final predictions of the plant net production are rather close to the reference values in both quantitative and qualitative terms (Table 9.3, Figs. 9.11–9.14).

- The average daily deviation in the net power production during the summer is 8.5% and 9.7% for PTR and tower models respectively. Considering that the detailed numerical simulations of SEGS-VI, Andasol-2 trough-based CSP plants performed in the studies [71, 87] resulted in the average daily errors of up to 8–10%, this additionally demonstrates that the proposed CSP models despite the applied simplifications still provide reasonable accuracy.

- Finally, the average time per one-year simulation is almost the same for PTR and tower models and approximately equal to 0.4 seconds. The major computational effort is required by the complex dispatch logic, which has to be followed at each simulation step. The calculation time in general is considered acceptable, however if needed it can be reduced further with the code optimization. In comparison, the corresponding execution times required by the PTR and tower models in SAM are approximately 9 and 16 seconds, respectively.

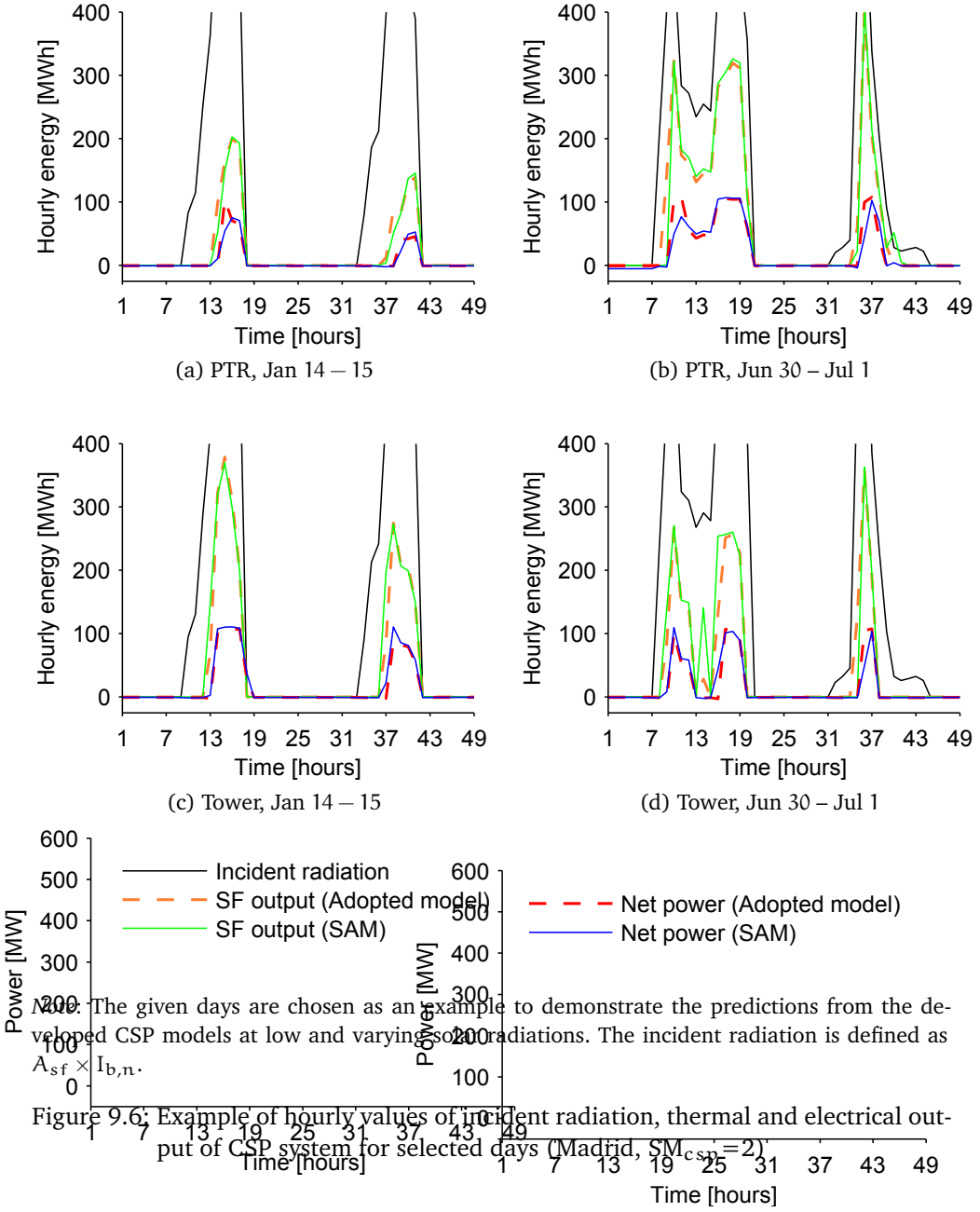

(a) PTR, Jan 14 – 15

(b) PTR, Jun 30 – Jul 1

(c) Tower, Jan 14 – 15

(d) Tower, Jun 30 – Jul 1

Note: The given days are chosen as an example to demonstrate the predictions from the developed CSP models at low and varying solar radiations. The incident radiation is defined as $A_{sf} \times I_{b,n}$.

Figure 9.6: Example of hourly values of incident radiation, thermal and electrical output of CSP system for selected days (Madrid, $SM_{csp}=2$)

Calculation step		Minimum	Maximum	Abs. mean
		Annual deviations		
$I_{b,n} \Rightarrow Q_{sf}$	PTR	–1.4	+3.9	1.5
	Tower	–3.7	+3.8	1.6
$Q_{sf} \Rightarrow P_{csp}$	PTR	–0.9	+3.0	1.2
	Tower	–1.2	+1.8	0.7
$P_{csp} \Rightarrow P_{csp,net}$	PTR	–1.3	–0.1	0.7
	Tower	–1.4	+0.4	0.7
		Monthly deviations for summer		
$I_{b,n} \Rightarrow Q_{sf}$	PTR	–2.8	+7.1	2.3 (1.8)
	Tower	–7.0	+6.0	2.7 (2.1)
$Q_{sf} \Rightarrow P_{csp}$	PTR	–4.0	+4.6	2.1 (2.3)
	Tower	–2.3	+4.4	1.4 (1.0)
$P_{csp} \Rightarrow P_{csp,net}$	PTR	–1.6	+0.9	0.6 (1.3)
	Tower	–1.3	+1.0	0.5 (0.9)

Note: The errors for the steps $Q_{sf} \Rightarrow P_{csp}$ and $P_{csp} \Rightarrow P_{csp,net}$ are estimated through separate simulations using the same values for the corresponding input parameters Q_{sf} and P_{csp}. The values in brackets represent the corresponding absolute mean monthly deviations obtained by averaging across the whole year.

Table 9.2: Annual and monthly prediction errors (%) at individual calculation steps

	Minimum	Maximum	Abs. mean
	Annual deviations		
PTR	–0.9	+3.8	1.1
Tower	–2.9	+4.1	1.6
	Monthly deviations for summer		
PTR	–3.5	+6.6	2.0 (3.8)
Tower	–7.6	+6.1	2.4 (2.3)

Note: The values in brackets represent the corresponding absolute mean monthly deviations obtained by averaging across the whole year.

Table 9.3: Overall annual and monthly prediction deviations (%)

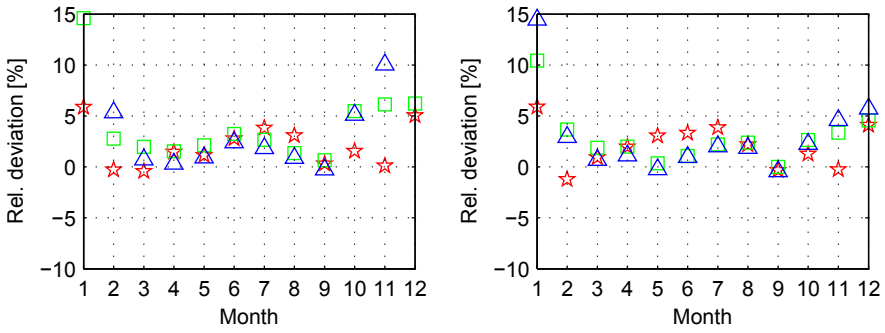

(a) Madrid

(b) Seville

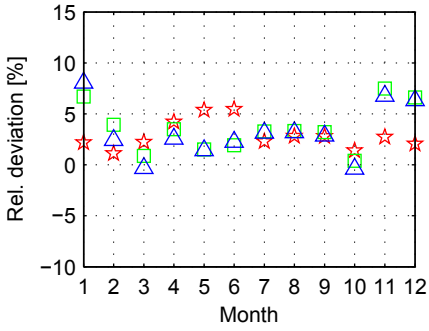

(c) Phoenix

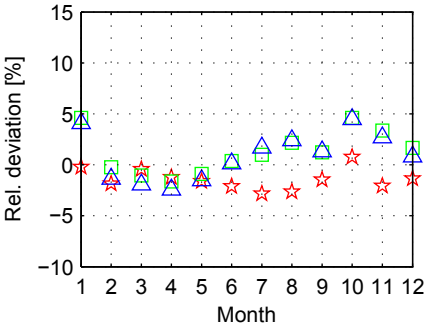

(d) New Delhi

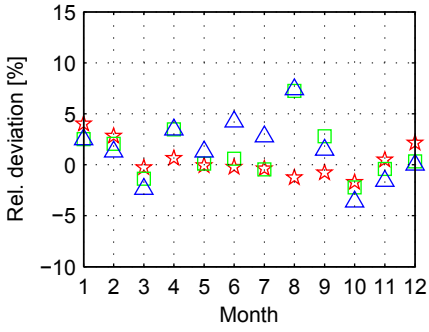

(e) Adelaide

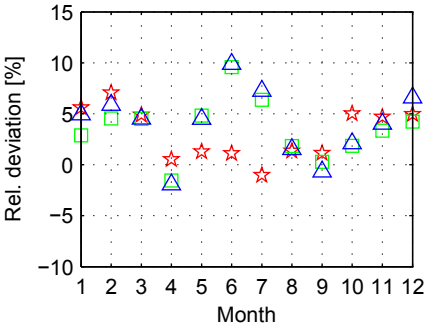

(f) Geraldton

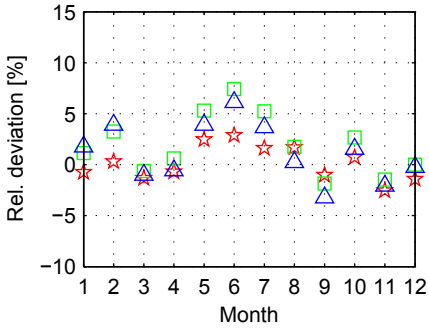

(g) Johannesburg

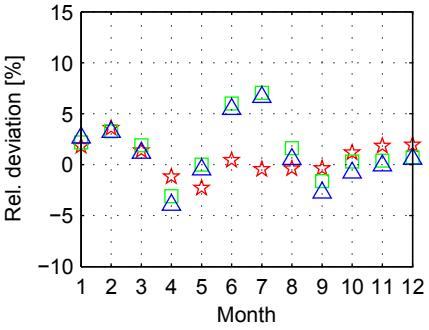

(h) Antofagasta

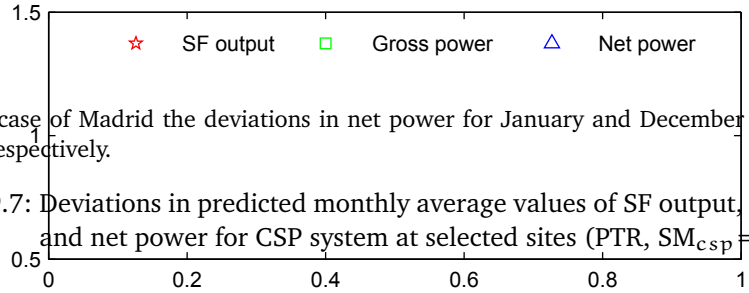

Note: In case of Madrid the deviations in net power for January and December are 40% and 30.5%, respectively.

Figure 9.7: Deviations in predicted monthly average values of SF output, gross power and net power for CSP system at selected sites (PTR, $SM_{csp}=2$)

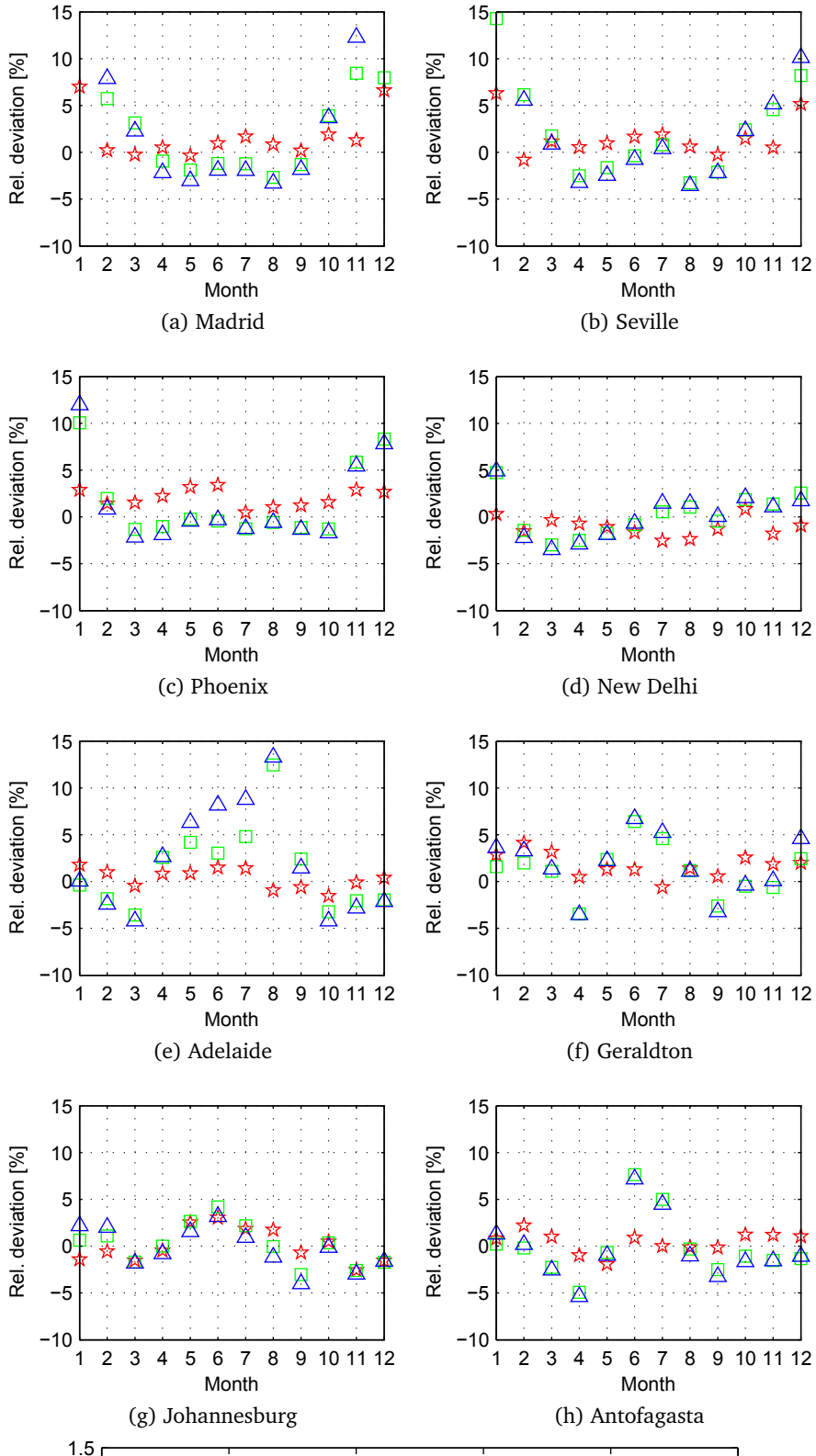

(a) Madrid (b) Seville

(c) Phoenix (d) New Delhi

(e) Adelaide (f) Geraldton

(g) Johannesburg (h) Antofagasta

Note: In case of Madrid the deviation in gross power for January is 25.9%, and the deviations in net power for January and December are 57.3% and 28.8%, respectively. In case of Seville the deviation in net power for January is 19.9%.

Figure 9.8: Deviations in predicted monthly average values of SF output, gross power and net power for CSP system at selected sites (PTR, $SM_{csp}=2.5$)

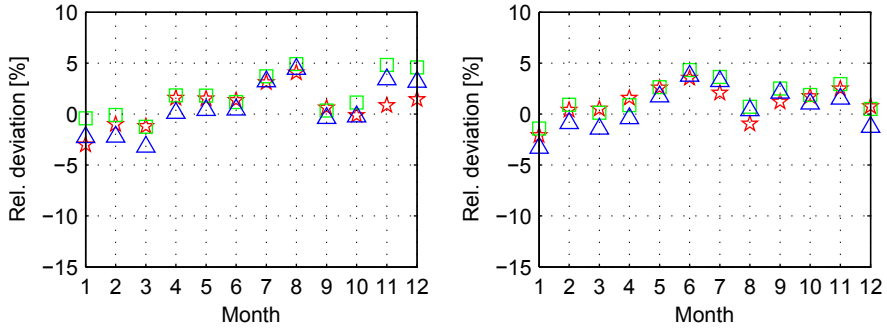

(a) Madrid

(b) Seville

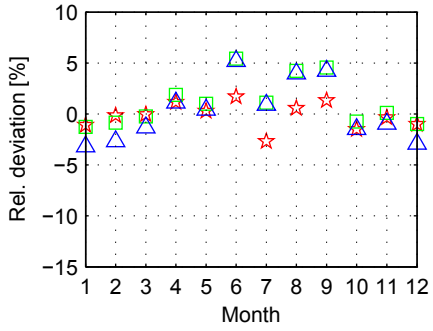

(c) Phoenix

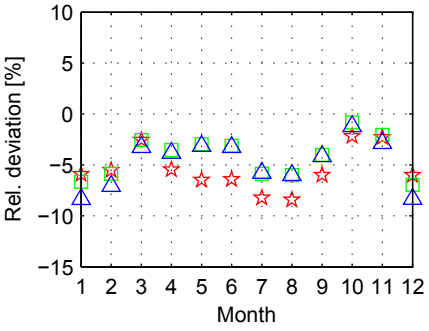

(d) New Delhi

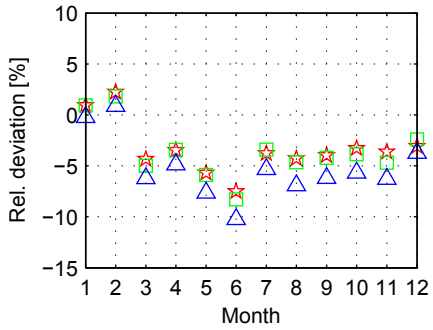

(e) Adelaide

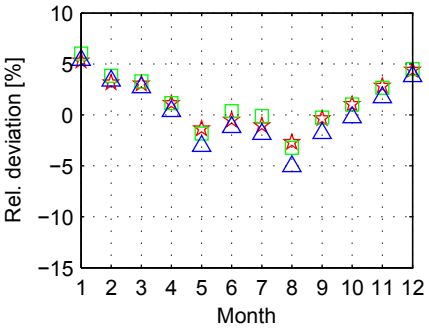

(f) Geraldton

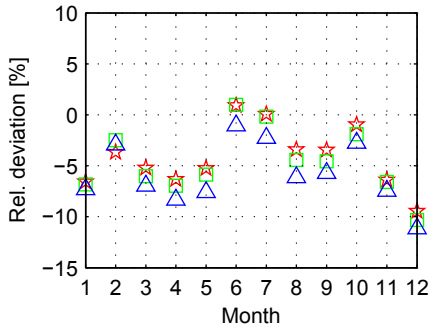

(g) Johannesburg

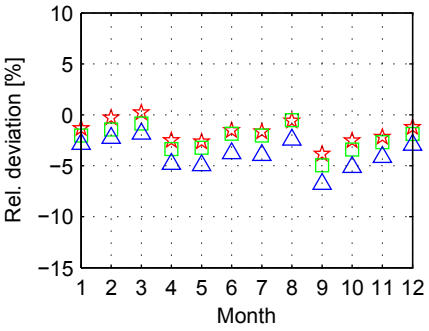

(h) Antofagasta

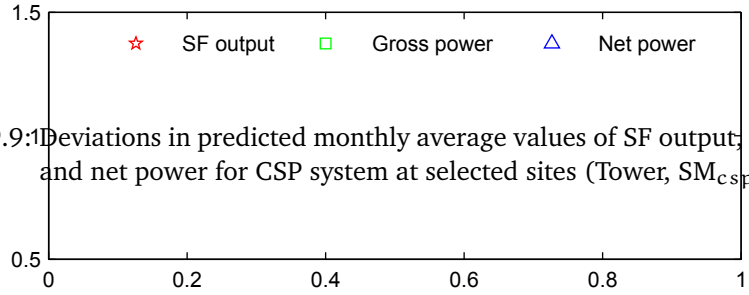

Figure 9.9:1 Deviations in predicted monthly average values of SF output, gross power and net power for CSP system at selected sites (Tower, $SM_{csp}=2$)

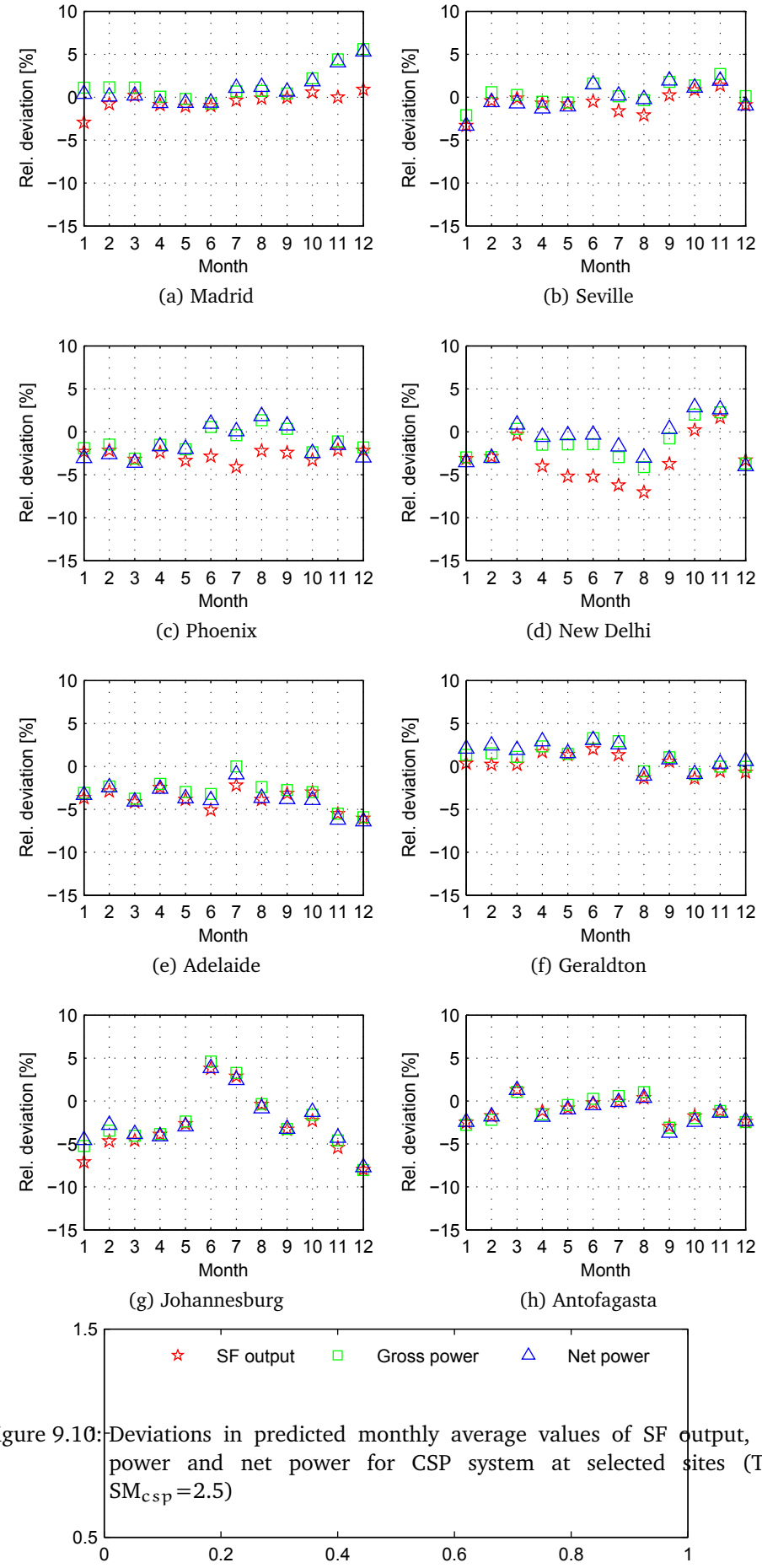

Figure 9.10: Deviations in predicted monthly average values of SF output, gross power and net power for CSP system at selected sites (Tower, $SM_{csp}=2.5$)

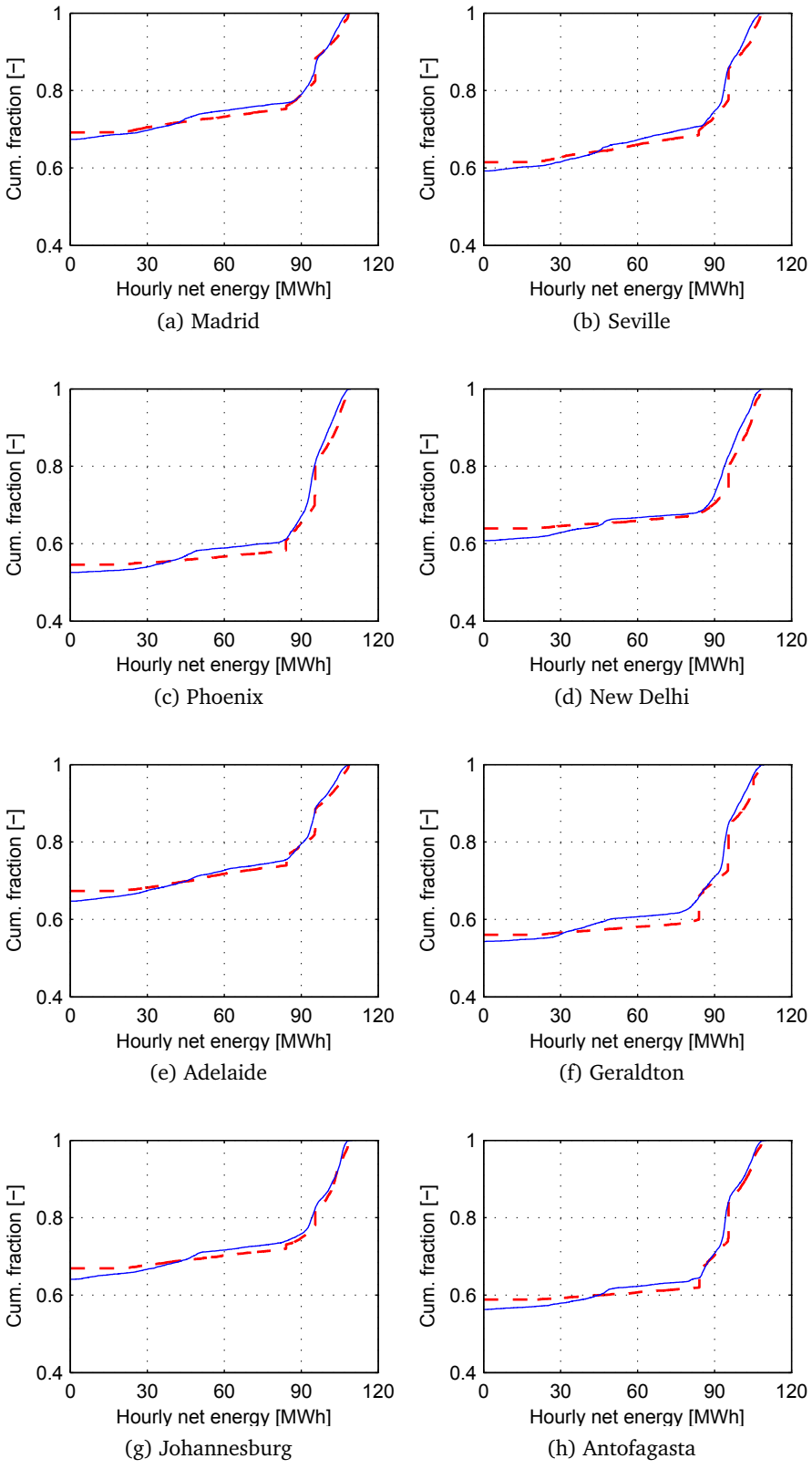

Figure 9.11: Cumulative distributions of the hourly net energy from CSP system at selected sites (PTR, $SM_{csp}=2$)

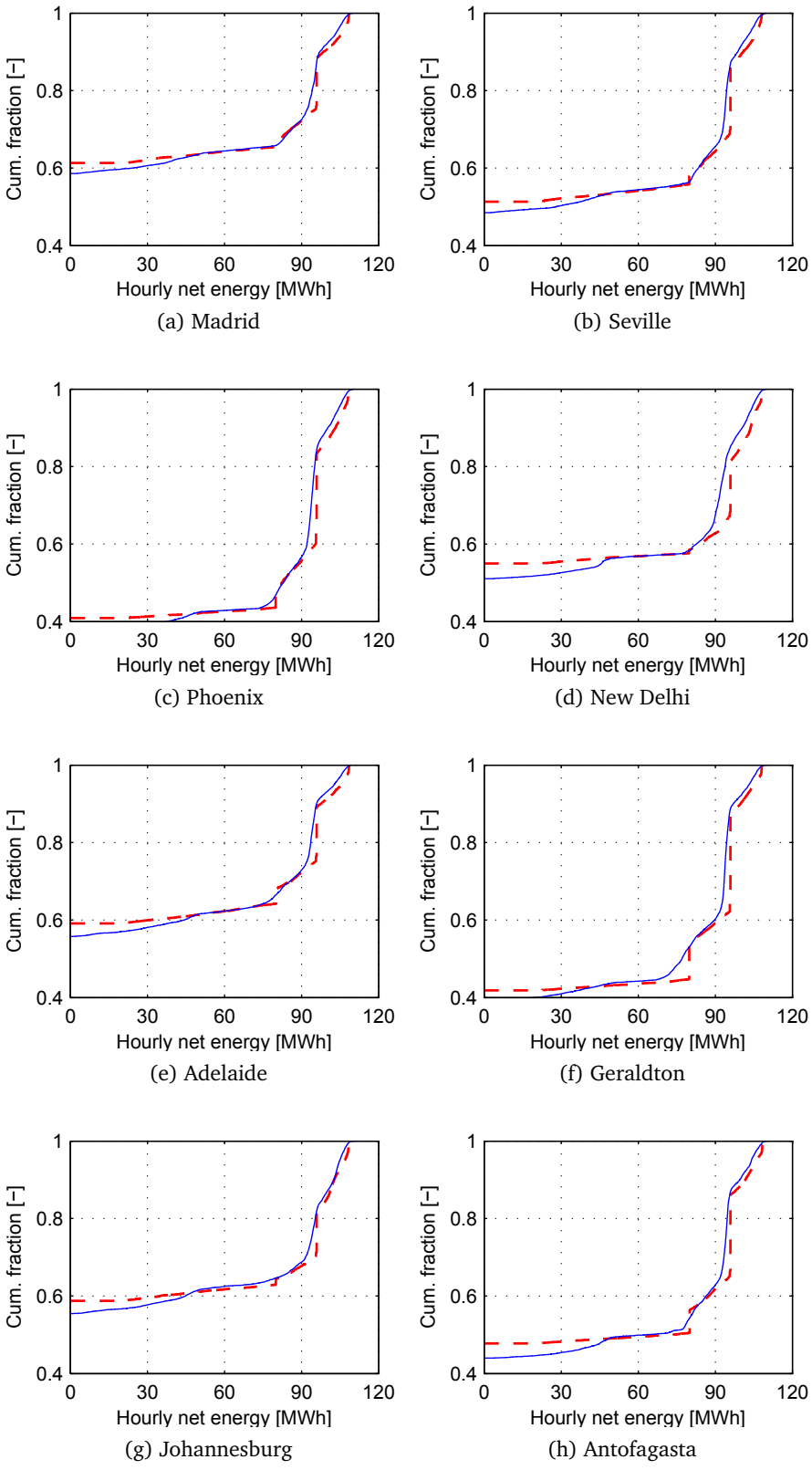

(a) Madrid (b) Seville

(c) Phoenix (d) New Delhi

(e) Adelaide (f) Geraldton

(g) Johannesburg (h) Antofagasta

Figure 9.12: Cumulative distributions of the hourly net energy from CSP system at selected sites (PTR, $SM_{csp}=2.5$)

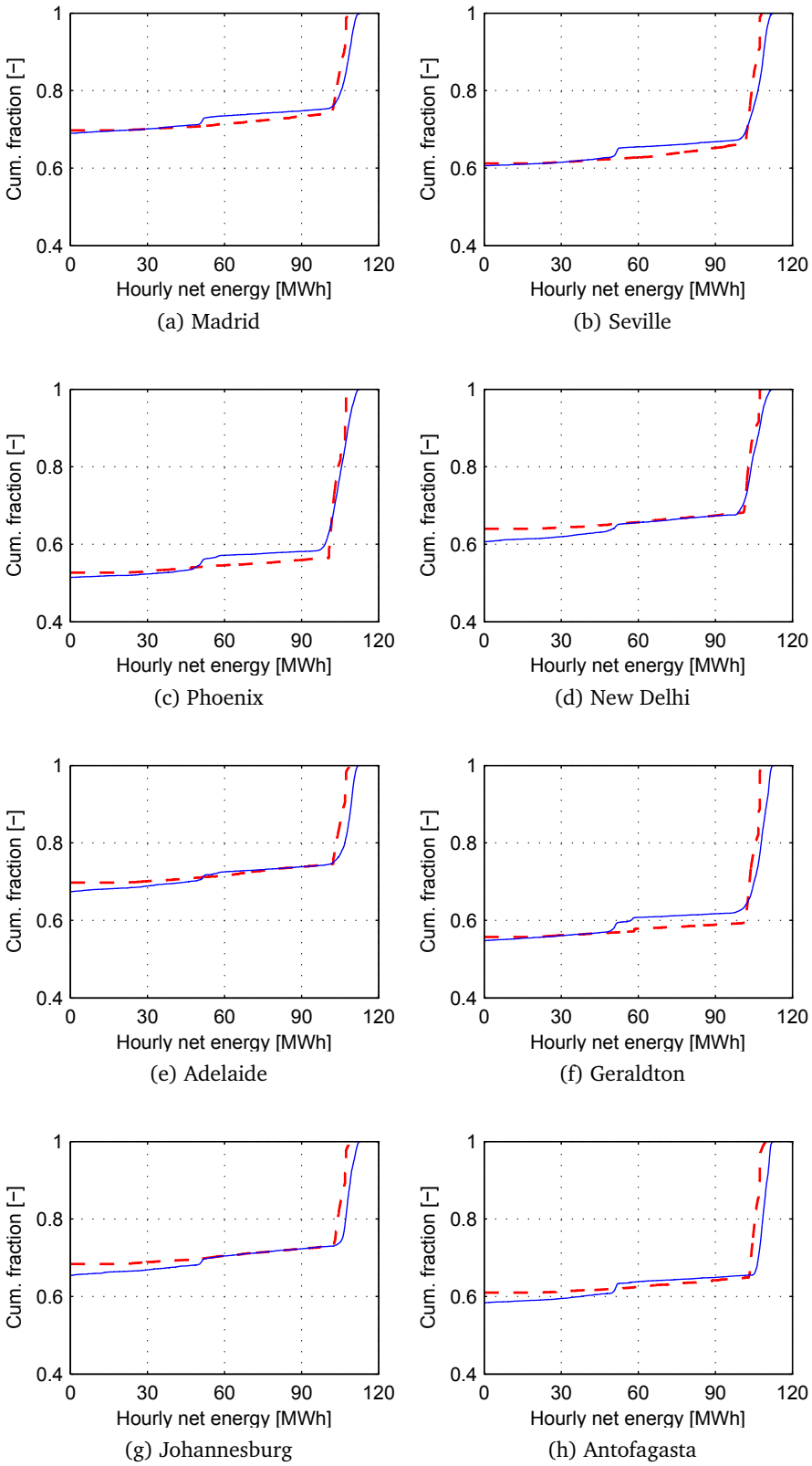

(a) Madrid (b) Seville

(c) Phoenix (d) New Delhi

(e) Adelaide (f) Geraldton

(g) Johannesburg (h) Antofagasta

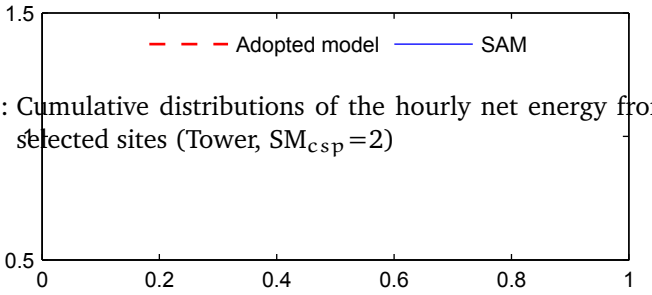

Figure 9.13: Cumulative distributions of the hourly net energy from CSP system at selected sites (Tower, $SM_{csp}=2$)

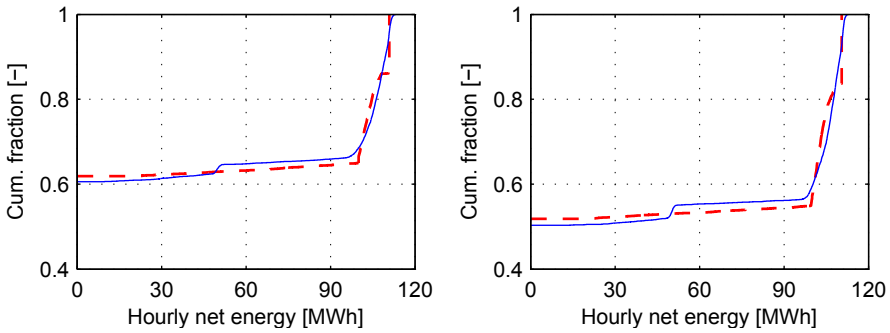

(a) Madrid (b) Seville

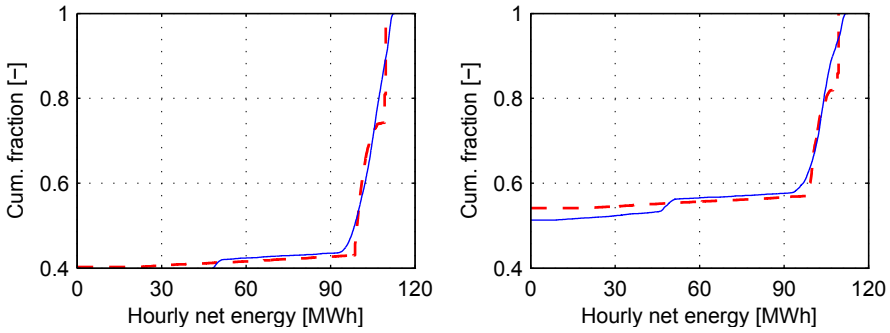

(c) Phoenix (d) New Delhi

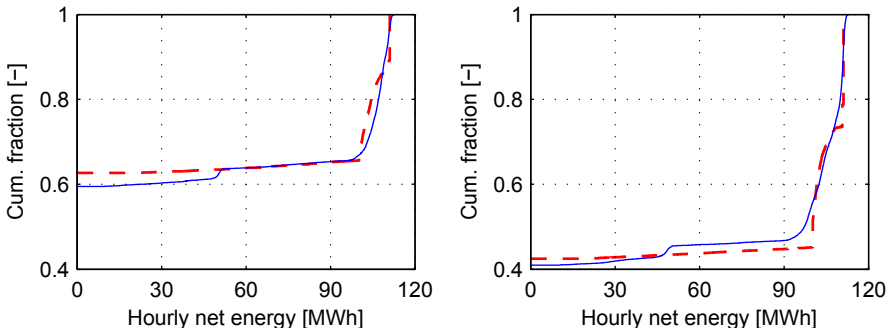

(e) Adelaide (f) Geraldton

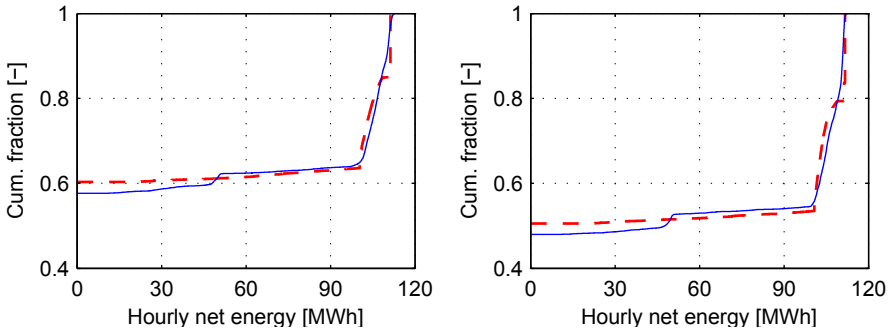

(g) Johannesburg (h) Antofagasta

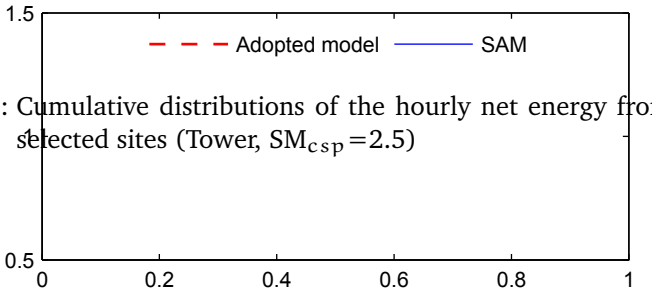

Figure 9.14: Cumulative distributions of the hourly net energy from CSP system at selected sites (Tower, SM_{csp}=2.5)

9.7 CONCLUDING REMARKS

Moderately simplified models of parabolic trough and central receiver systems were proposed for the application in generation system adequacy studies based on the sequential Monte Carlo technique.

The overall simulation procedure is divided into three steps: (a) calculation of the solar field thermal output, (b) plant dispatch and conversion of useful thermal energy to gross power, and (c) estimation of parasitic losses and net production.

The total number of input parameters and equations required for predicting CSP plant production was reduced approximately down to 25 and 20, respectively.

The performance of the developed CSP models was validated for multiple case scenarios by using SAM simulations as a reference. The obtained results demonstrated the adequacy of the adopted approaches to model reduction. In particular, it was shown that:

- The solar field output can be estimated with the average monthly deviation of up to 3% during the summer period even by ignoring the ambient temperature and assuming the constant thermal energy losses.
- The proposed procedure for creating the heliostat field layout and the correlation for shadowing and blocking efficiency can significantly simplify the optical performance estimation for tower system.
- The Rankine cycle calculations can be performed with the mean monthly error of up to 2% (summer) by modeling the power block efficiency simply as a polynomial of the relative loading.
- The plant parasitic losses can be determined with the average monthly deviation of less than 1% (summer) by scaling the parameters that have the highest influence on them.
- The average total deviations in the predicted net production from PTR/-tower plant are: 1.1/1.6% (annual), 2.0/2.4% (summer month) and 8.5/9.7% (summer day).
- The overall calculation time when using the simplified CSP models is reduced by approximately 20–40 times.

Part IV

ENERGY STORAGE DISPATCH MODELING

10 INTRODUCTION

Energy storage dispatch model proposed in Part IV of the thesis is intended for determining the amount of electricity supplied or absorbed by energy storage system (ESS) at each timestep by taking into account the internal and external conditions. As the model is to be used for generation system adequacy (GSA) assessments based on the sequential Monte Carlo (SMC) simulations, the research is centered on the model simplification and input data reduction. The focus on the dispatch modeling is explained by the fact that the given aspect represents the main difficulty when integrating energy storage into GSA evaluation.

10.1 LITERATURE REVIEW

Energy storage system is defined as a combination of energy storage and conversion units that allows storing and reusing energy from the power grid and/or other external (normally renewable) sources. ESS model is aimed to represent the involved energy conversion and storage processes; and to mimic the component behavior with respect to other power sources and system load. While the existing analytical calculation techniques are well developed for certain specific tasks, it is the simulation-based approach that allows high precision and flexibility in general purpose ESS modeling. As noted in previous chapters, this is one of the motivations for using the sequential Monte Carlo method in generation system adequacy assessment of power systems with high share of time-dependent sources, such as energy storage and solar power.

ESS simulation model comprises two equally important aspects: (a) the physics/chemistry of energy storage and conversion, and (b) dispatch strategy. The former is determined by the technology deployed and the corresponding mathematical formulation is usually available and can be adapted depending on the desired precision and complexity level. The dispatch strategy, on the other hand, depends on the ESS application during the power system operation and its incorporation into simulations in GSA studies is not straightforward. The difficulty comes from the fact that such analyses normally focus on static conditions of generation system and ignore the operating details required for correct implementation of the dispatch logic.

A literature review reveals a limited number of GSA studies involving energy storage, that can be explained by still low usage of the latter in today's electricity supply. The selected works and their main features are summarized in Table 10.1. As one can see, chronological simulations of ESS are combined with different GSA evaluation methods. Dispatchable generation (DPG), corresponding to thermal power units, traditionally is represented by the series of available firm capacity defined at each time interval as the total installed capacity minus the forced outages (static model) [18]. Some studies take into account also DPG operation by applying a simplified merit-order dispatch

Study	GSA evaluation method	DPG model	RES type	ESS type	ESS dispatch criterion
[4]	SMC	operating	–	HPP, PSP	Economic, Load balancing
[85]	SMC	operating	wind	HPP	Mixed
[5]	SMC	operating	–	PSP	Economic, Load balancing
[63]	SMC	static	wind	General	RES coordination
[73]	SMC	–	wind	HPP	RES coordination
[12]	SMC	static	wind, PV	Battery	Pure reliability
[164]	SMC	static	wind	General	Pure reliability
[101, 158]	state sampling Monte Carlo	static	wind	HPP	RES coordination
[43]	1-year simulation	–	hydro, PV	PSP	Load balancing
[88]	1-year simulation	–	wind, PV	PSP	Load balancing
[139]	8-year simulation	static	–	General	Load leveling
[50]	analytical	static	wind	General	Pure reliability
[24]	analytical	static	wind	PSP	Load leveling
[29]	mixed	operating	–	HPP	Load balancing
[15]	mixed	static	wind	Battery	Load balancing

Table 10.1: Selected studies of generation system adequacy with energy storage

and a set of heuristic rules [4, 5, 29, 85]. The common renewable energy source (RES) included in the analyses is wind and the typical ESS are conventional hydro power plant (HPP) and pumped storage plant (PSP). The main criteria adopted for ESS dispatch are:

- Pure reliability – charging at excess of production and discharging only at emergency conditions, i. e. at shortage of generation capacity
- Load balancing – compensating the resultant power imbalances after the dispatch of all other power units (in case of 100% renewable supply the criterion is the same as 'pure reliability')
- Economic dispatch – operation of all power sources including ESS is optimized to reduce the total costs and maintain the required level of reliability
- RES coordination – compensation of renewable power variations aimed at keeping the production from RES-ESS pair at the specified level (in absolute or relative terms) and thus improving the capacity credit of renewable energy and reducing its spillage
- Load leveling – valley filling and peak shaving of the system load

Interestingly, among the reviewed works only [63, 73] focus on ESS dispatch modeling in GSA analysis using SMC simulations. Both studies analyze how the system adequacy is affected with deployment of ESS to support wind production. In [63] general storage is considered and its dispatch is coordinated with wind power to cover a fixed fraction of the system load. Whereas [73] combines a HPP with a wind farm to maintain their total power output close to a specified percentage of the installed wind capacity.

From GSA perspective the main shortcomings of the existing approaches to ESS dispatch modeling are as follows:

Limitations of the dispatch criteria. For example, 'pure reliability' ignores ESS operation under normal conditions when generation capacity is sufficient; 'load balancing' is applicable if DPG participation in the power regulation is taken into account; 'economic dispatch' requires detailed data on the system operation and costs; 'RES following' assumes constant requirements in the firm capacity; and 'load leveling' excludes the impact of RES production.

Inadequate simulation of storage level variation. Most of the reviewed simulation strategies are based on simple fixed rules with the storage level control limited to checking the lower and upper bounds, which leads to unrealistic operating cycles (e. g. long periods with minimum or maximum charge). If the expected storage variation profiles are known from historical data for some scenarios (e.g. wet, dry and normal hydrological years in case of HPP), they can be reinforced by applying additional operating constraints as in [4, 29]. The problem however is that (a) the changes among the resultant operating cycles are limited by the scenarios and (b) according to [27] with higher penetrations of renewables the existing ESS may have to alter dramatically their operation which makes irrelevant in this case the reference storage profiles from historical data. There is of course an option to obtain more precise and realistic results by applying dynamic programming optimization [5, 139], but it might not be suitable due to high computational cost and increased input data requirement.

Lack of general framework applicable to GSA assessment with different types and mix of RES, ESS and DPG. Among other things this concerns possibility of incorporating multiple dependent storage systems (e. g. cascade of water reservoirs) and also dealing simultaneously with various operating timescales (e. g. annual, weekly or daily).

10.2 OBJECTIVES AND METHODOLOGY OF PART IV

The objective of Part IV of the thesis is to develop a general dispatch model of energy storage suitable for generation system adequacy studies using the sequential Monte Carlo method. The model should allow determining at each simulation step the power absorbed or produced by ESS depending on the internal and external conditions.

By taking into account the drawbacks of the existing approaches and inherent characteristics of the Monte Carlo-based GSA estimations, the following requirements are defined:

- Consistent dispatch criterion
- Adequate simulation of ESS normal operation, particularly of the storage level variations
- General applicability independent of ESS type/number and the total generation mix
- Moderate complexity
- Reduced input information

It is important to note that the model optimization to reduce the overall computational effort has not been considered in this research.

11 DISPATCH MODEL OF ENERGY STORAGE

A new dispatch model of energy storage system (ESS) is developed for generation system adequacy (GSA) assessments based on the sequential Monte Carlo (SMC) simulations. The overall calculation procedure is shown in Fig. 11.1. The proposed ESS dispatch model in this case is employed to determine the amount of electricity supplied or absorbed by ESS at each timestep by taking into account the storage level (state of charge), forced outages and intermittency of demand and renewable generation. The model requires a set of control parameters which are estimated by simulating ESS with the same dispatch procedure but under simplified operating conditions. The details of the new dispatch technique are given in the following sections.

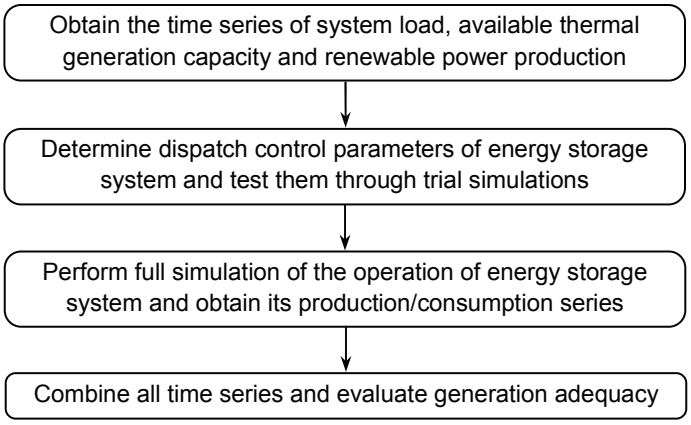

Figure 11.1: Main steps of GSA study including renewable sources and energy storage

11.1 GENERAL FORMULATION OF ENERGY STORAGE AND CONVERSION

In order to provide a framework for modeling ESS dispatch, a generalized description of energy storage, conversion and irregular in-/outflows is required. In this work the adopted formulation is based on the scheme shown in Fig. 11.2.

In analogy with hydroelectric system, the key parameters are storage level V, power extracted from or delivered to the grid P, rate of energy (carrier) flows from storage to conversion unit Q, from conversion unit to primary sink Q_{sink}, from primary source to storage W_{in}, from storage to sink W_{out} (known part) and S (unknown part), and finally, energy (carrier) loss from storage W_{loss}. The flows P, Q, Q_{sink} when leaving ESS are considered positive. The plant capacity factor, an important performance indicator, is calculated separately for production and consumption modes:

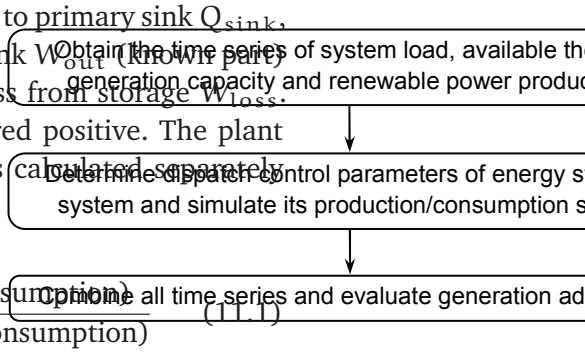

$$\mathrm{CapFac}_{\mathrm{out(in)}} = \frac{\text{Mean power in production (consumption)}}{\text{Nominal power in production (consumption)}} \tag{11.1}$$

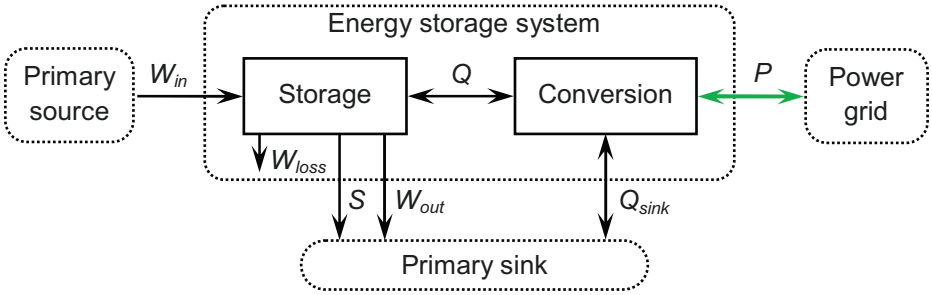

Figure 11.2: General scheme of energy storage system

The use and association of the parameters depend on the type of ESS. For example, for hydroelectric station it can be done as follows: V – reservoir water volume, Q – (dis)charge flow directed to turbine or pump, $Q_{sink}=Q$ – water flow from turbine or pump to downstream side, W_{in} – water inflow into reservoir as a result of precipitation and water release from upstream reservoirs, W_{out} – water use for other purposes besides power generation (e. g. flood control, water supply to public, industry and agriculture), S – spillage and W_{loss} – reservoir water loss by evaporation. By definition, $Q \geqslant 0$ for conventional hydro power plant without charging option (HPP), and $W_{in}=W_{out}=S=0$ for pumped storage plant (PSP). For a single HPP, the primary source and sink are the upstream and downstream parts of a given river basin, respectively. Whereas for a single PSP the primary source is not applicable and the primary sink would be the downstream reservoir of the pumping station. In case of multiple connected reservoirs the corresponding ESS network model can be built by treating individual power plant as a primary source/sink with respect to the downstream/upstream plants.

For compressed air based ESS, the primary source and sink flows could be ignored, with the remaining parameters linked as: V – stored air mass, Q – (dis)charge rate of compressed air, and W_{loss} – leakage of stored air.

Independently of the selected association, all critical parameters and their limits have to be considered together with the following basic constraints

$$V_{min} \leqslant V \leqslant V_{max} \tag{11.2}$$

$$Q_{min} \leqslant |Q| \leqslant Q_{max} \tag{11.3}$$

$$P_{min} \leqslant |P| \leqslant P_{max}, \tag{11.4}$$

where the limits of Q and P in general can vary depending on ESS operation mode.

The governing equations describing the balance within storage component and power conversion are

$$V_j = V_{j-1} + W_{in,j} - W_{out,j} - W_{loss} - Q_j - S_j \tag{11.5}$$

$$\text{if } Q > 0,\ P = f_1(Q,V) \quad \text{and} \quad \text{if } Q < 0,\ P = f_2(Q,V) \tag{11.6}$$

One should note that (11.6) includes the energy conversion losses and the relation of the storage level to the corresponding energy potential (e.g. hydraulic head, compressed air pressure).

11.2 PROPOSED DISPATCH MODEL FOR ENERGY STORAGE SYSTEMS

As noted earlier, the new ESS dispatch model is intended to determine ESS power P at each simulation step depending on the internal and external conditions. Aimed for simplicity and generality, the developed model attempts to mimic both emergency and normal operation by assuming that ESS is employed to reduce renewable energy curtailments and the back-up generation capacity. To achieve a realistic simulation of storage level variations, the model applies dispatch corrections based on the classical proportional integral controller technique.

The main inputs are reduced to:

- System data – series of system load L_{sys}, renewable production P_{RES} and available total thermal (dispatchable) generation capacity CAP_{avail}
- ESS data – dispatch constraints, capacity factor in consumption mode $CapFac_{in}$, long-term average value of the storage level V_{aver} and series of energy (carrier) flow between storage unit and primary source W_{in} or sink W_{out}

As it will be shown, besides these inputs ESS dispatch also requires the following control parameters: power thresholds F_{in}, F_{out}; reference storage level profile $\widehat{V}_{ref}$; and proportional/integral gain constants K_P, K_I. Their identification procedures are presented in Section 11.3.

11.2.1 *Assumptions and definitions*

By taking into account the shortcomings of the existing approaches and inherent characteristics of GSA studies, the following complementary assumptions and definitions are adopted for modeling ESS dispatch.

Operating timescale. Variation of ESS operating parameters (P, Q, V) exhibits a pattern that repeats itself at certain time interval and contains at least one charge and one discharge instance. The length of the given time interval represents the length of ESS operating cycle t_C. For large-scale installations it is typically a day, a week or a year. In case of non-negligible and regular inflow from primary source, t_C is expected to be the same as the period of W_{in} variation profile, which for most renewable-based inflows would be a year.

For calculation purposes, ESS operating cycle length is assumed to be the factor of t_Y, the number of hours in one year. Thus, each year can be considered as a sequence of $N_P = t_Y/t_C$ operating periods. This allows employing multi-dimensional indexing of simulation steps as $[y, p, h]$, where $y = [1, N_Y]$, $p = [1, N_P]$, $h = [1, t_C]$ and N_Y is the total number of simulation years. For example, for ESS with daily operating cycle the power output $P_{[5,200,7]}$ corresponds to year 5, day 200, hour 7.

Dispatch order. The ESS dispatch is performed by taking into account the system load, the power production from renewable energy sources (RES) and the available total capacity of dispatchable generation (DPG).

When the system contains multiple independent ESS with the same operating cycle periods, they are dispatched sequentially according to a selected rule, e. g. from large to small, from less to more flexible units. In case of different operating timescales ESS simulations are run starting from the units with the shortest cycles.

If ESS operations are related, then the simulation order takes into account the dependency between individual plants. For example, for a multi-reservoir hydroelectric system the dispatch would be performed in the water flow direction by considering upstream ESS as a primary source for the downstream ESS. The dispatch procedure in this case is notably simplified since the water discharge for other purposes W_{out} is assumed to be known.

Residual load and its components. Residual load is defined as initial system electricity demand minus (plus) power production (consumption) from the power units that have been committed up to the given moment. Taking into account the previous assumptions residual load prior to ESS dispatch is equal to

$$RL = L_{sys} - P_{RES} - P_{other}, \tag{11.7}$$

where L_{sys} is the system load, P_{RES} is the generation from renewable sources with none or relatively low storage capacity, and P_{other} is the production or consumption from already dispatched ESS units.

The trend component is obtained by averaging RL sequence along each subsequent operating cycle of ESS

$$RL_{trend,[y,p]} = \frac{1}{t_C} \sum_{h=1}^{t_C} RL_{[y,p,h]} \tag{11.8}$$

Finally, the detrended component of residual load is determined as

$$\Delta RL_{[y,p,h]} = RL_{[y,p,h]} - RL_{trend,[y,p]}, \tag{11.9}$$

which means that it contains only variations of residual load within ESS operating timescale and excludes the average changes from one operating cycle to another.

11.2.2 *Formulation of energy storage dispatch*

The proposed dispatch model at each simulation timestep (in this work at each hour), first, determines a preliminary ESS power P_{prel} and then applies the necessary modifications to account for the operating limitations. The calculation procedure is different for emergency and normal conditions, which are distinguished based on the values of residual load and available thermal generation capacity CAP_{avail}.

Emergency situation: $RL > CAP_{avail}$

In emergency conditions ESS is dedicated entirely to reduce the expected capacity shortage. The preliminary power is defined as

$$P_{prel} = RL - CAP_{avail} \tag{11.10}$$

The corresponding storage-conversion flow rate and storage level are obtained from (11.6) and (11.5), respectively. The values of Q and P are adjusted to satisfy the restrictions (11.2)–(11.4).

As one can see, the calculations in this case are straightforward and are similar to the existing approaches.

Normal situation: $RL \leqslant CAP_{avail}$

In normal conditions ESS is employed for leveling detrended residual load ΔRL, in other words, for reducing RES curtailments and DPG capacity within each operating cycle. The leveling is done based on the power thresholds for valley filling F_{in} and peak shaving F_{out} which can be determined according to the procedure described in Section 11.3.2. The given thresholds basically represent the lower and upper limits of ΔRL, below and above which ESS is expected to consume and produce, respectively. Considering this, the preliminary power is estimated as:

$$P_{prel} = \begin{cases} \Delta RL - F_{in}, \text{ if } \Delta RL < F_{in} \\ \Delta RL - F_{out}, \text{ if } \Delta RL > F_{out} \\ 0, \text{ otherwise} \end{cases} \tag{11.11}$$

The corresponding storage-conversion flow rate Q_{prel} is found from (11.6) by making possible adjustments to meet the constraints (11.2)–(11.4).

ESS dispatch strategy based on (11.11) and the corresponding limitations alone cannot guarantee natural variations of the storage level around the expected average value V_{aver}. The reason is that: (a) even a small error in the power thresholds might lead to the imbalance between the amounts of energy carrier attempted to be extracted from ESS and to be delivered in the long term, and (b) limited storage capacity might not allow accommodating all variations in energy carrier in-/outflows. To overcome this problem the clas-

sical proportional-integral control is applied to storage level variations. The dispatch at each timestep is corrected as follows:

$$\Delta Q_{[y,p,h]} = K_P \left(V_{[y,p,h]} - \widehat{V}_{ref,h}\right) + K_I \left(\sum_{k=1}^{y-1}\sum_{j=1}^{N_P}\left(V_{[k,j,h]} - \widehat{V}_{ref,h}\right) + \sum_{j=1}^{p}\left(V_{[y,j,h]} - \widehat{V}_{ref,h}\right)\right) \quad (11.12)$$

$$Q_{corr} = Q_{prel} + \Delta Q, \quad (11.13)$$

where $\widehat{V}_{ref}$ is the reference profile, comprising the storage level values expected, on average, during operating cycle; K_P, K_I are proportional and integral gain constants, respectively; and Q_{prel}, Q_{corr} are the values of storage-conversion flow before and after the correction. Obviously, the use of complete storage variation profile $\widehat{V}_{ref}$ instead of V_{aver} as a reference increases the control complexity, but it allows reduced and more precise dispatch corrections.

To assure that the additional control using (11.12), (11.13) is consistent with the preliminary dispatch aimed at leveling detrended residual load, the following general restriction is included

$$\mathrm{sgn}(Q) = \mathrm{sgn}(\Delta RL) \quad (11.14)$$

Based on the given considerations the new ESS dispatch procedure for normal conditions consists of the following steps:

1. Estimate the preliminary value of power production/consumption for a given timestep according to (11.11) and apply the constraint (11.4).
2. Find from (11.6) the corresponding storage-conversion flow rate by making possible adjustments to satisfy the limitations (11.2)–(11.4).
3. Correct the storage-conversion flow by using (11.12), (11.13).
4. Find the corresponding power production/consumption and storage level from (11.6) and (11.5), respectively. The final values of Q and P again might need to be adjusted according to (11.2)–(11.4), (11.14).

11.3 IDENTIFICATION OF DISPATCH CONTROL PARAMETERS

As one can see, the proposed ESS dispatch model requires the reference storage profile $\widehat{V}_{ref}$, the power thresholds F_{in}, F_{out} and the gain constants K_P, K_I. Possible approaches to estimation of these control parameters are described below and a demonstration of the steps used is provided by the numerical example in Section 11.5.

11.3.1 *Reference storage profile*

Reference storage profile, which is the expected average storage level variation within operating timescale, can be identified by performing ESS dispatch based on (11.11) for the average annual conditions. When the length of operating cycle is less than a year, the dispatch is done separately for each operating period of the year and then averaging is applied to obtain one or several reference storage profiles (e. g. one for weekdays and one for weekends in case of daily cycle).

The underlying assumptions are: (a) ESS production in emergency situation is negligible, (b) storage capacity is sufficient to accommodate the resultant variations in total energy in-/outflows, and (c) the capacity factor in consumption mode $CapFac_{in}$ (if applicable) and the long term average storage level V_{aver} are known.

An important requirement in this case is that all energy in-/outflows during the operating cycle should be balanced, in other words, the storage level at the end points of the cycle should be the same. The given condition together with the values of $CapFac_{in}$ and V_{aver} enables calibration of the missing power thresholds $\widehat{F}_{in}$, $\widehat{F}_{out}$ for the average year[1] through iterative calculations.

The recommended procedure to define the reference storage profile is as follows:

1. Determine the average annual profiles of detrended residual load $\widehat{\Delta RL}$ and energy carrier flows between storage and primary source/sink $\widehat{W}_{in}$, $\widehat{W}_{out}$ based on the general expression

$$\widehat{x}_{[p,h]} = \frac{1}{N_Y} \sum_{y=1}^{N_Y} x_{[y,p,h]} \tag{11.15}$$

   where x is any relevant variable; $y = [1, N_Y]$, $p = [1, N_P]$ and $h = [1, t_C]$ are the indices referring to the given simulation year, operating period and hour, respectively. If not stated otherwise, the hat symbol denotes the parameters for the average annual conditions.

2. Initialize the storage level profiles for each operating period of the year with uniform profile: $\widehat{V}_{[p,h]} = V_{aver}$

1 $\widehat{F}_{in}$, $\widehat{F}_{out}$ should not be confused with the actual power thresholds used for full ESS simulation and identified according to the procedure presented in Section 11.3.2.

3. Initialize the power thresholds for average annual conditions: $\widehat{F}_{in,p} = \mathtt{min}(\widehat{\Delta RL}_{[p]})$, $\widehat{F}_{out,p} = \mathtt{max}(\widehat{\Delta RL}_{[p]})$ and choose a variation step ΔF, which will define the precision of the calculated power thresholds.

4. If charging from the power grid is not applicable, skip to step 7. Otherwise, increase the threshold for valley filling by the specified amount $\widehat{F}_{in,p} = \widehat{F}_{in,p} + \Delta F$

5. Perform normal dispatch for the valley filling timesteps during each operating period ($\widehat{\Delta RL}_{[p]} < \widehat{F}_{in,p}$) without the storage level control, i. e. by using (11.2)–(11.4), (11.6) and (11.11) for the average annual conditions. Based on this obtain the values of power $\widehat{P}_{[p]}$ and storage-conversion flow $\widehat{Q}_{[p]}$ in the consumption mode.

6. Find the value of $\widehat{F}_{in,p}$ by repeating steps 4, 5 until the resultant consumption capacity factor equals to $CapFac_{in}$. Different values of the capacity factor can be used for different operating periods of the year.

7. Reduce the threshold for peak shaving by the specified amount $\widehat{F}_{out,p} = \widehat{F}_{out,p} - \Delta F$

8. Perform normal dispatch for the peak shaving timesteps during each operating period ($\widehat{\Delta RL}_{[p]} > \widehat{F}_{out,p}$) without the storage level control, i. e. by using (11.2)–(11.4), (11.6) and (11.11) for the average annual conditions. Based on this obtain the values of power $\widehat{P}_{[p]}$ and storage-conversion flow $\widehat{Q}_{[p]}$ in the production mode.

9. Find the value of $\widehat{F}_{out,p}$ by repeating steps 7, 8 until the total in-/outflows during the operating period are balanced, i. e.

$$\sum_{h=1}^{t_C} \left(\widehat{W}_{in,[p,h]} - \widehat{W}_{out,[p,h]} - \widehat{W}_{loss,[p,h]} - \widehat{Q}_{[p,h]} \right) = 0 \qquad (11.16)$$

Note that expression (11.16) is an integrated form of (11.5) taking into account the above-mentioned condition that the storage level at the end points of operating cycle should the same.

10. Update the cumulative variation(s) of energy carrier in-/outflows

$$\Delta\widehat{V}_{[p,h]} = \sum_{j=1}^{h} \left(\widehat{W}_{in,[p,j]} - \widehat{W}_{out,[p,j]} - \widehat{W}_{loss,[p,j]} - \widehat{Q}_{[p,j]} \right) \qquad (11.17)$$

and the storage level profile(s)

$$\widehat{V}_{[p,h]} = \Delta\widehat{V}_{[p,h]} + V_{aver} - \frac{1}{t_C} \sum_{h=1}^{t_C} \Delta\widehat{V}_{[p,h]} \qquad (11.18)$$

Repeat steps 3–10 until the changes in $\widehat{V}_{[p]}$ are negligible. The convergence can be monitored, for example, based on the root-mean-squared difference between the storage curves in subsequent iterations.

11. Average the storage level profiles from all operating periods to one

$$\widehat{V}_{ref,h} = \frac{1}{N_P} \sum_{p=1}^{N_P} \widehat{V}_{[p,h]} \tag{11.19}$$

If the variation among individual profiles $\widehat{V}_{[p]}$ is significant, it is possible to apply separate averaging for different periods of the year and thus obtain several reference profiles.

The described calculations allow also estimating the average annual profiles of other parameters such as the ESS power, which in turn can be used for calculating the production capacity factor CapFac_{out} based on (11.1).

It is important to mention again that the thresholds $\widehat{F}_{in}$, $\widehat{F}_{out}$ are valid only for the average annual conditions and strictly cannot be deployed for full ESS simulation.

11.3.2 *Power thresholds*

Identification of the actual power thresholds F_{in}, F_{out} requires the series of detrended residual load and the capacity factor values CapFac_{in}, CapFac_{out}. It is done in the following steps:

1. Initialize the power threshold for each operating period of the year as $F_{in,p} = \texttt{min}(\Delta RL_{[p]})$ and $F_{out,p} = \texttt{max}(\Delta RL_{[p]})$, where $\Delta RL_{[p]}$ corresponds to the detrended residual load values from all simulation years, but only within the given operating period.

2. Choose a variation step ΔF, which will define the precision of the calculated power thresholds.

3. Adjust the threshold by the specified amount $F_{in,p} = F_{in,p} + \Delta F$ and $F_{out,p} = F_{out,p} - \Delta F$

4. Obtain the corresponding ESS power series based on (11.4), (11.11).

5. Find the values of $F_{in,p}$ and $F_{out,p}$ by repeating steps 3, 4 until the desired consumption/production capacity factor is achieved. Different values of the capacity factor can be used for different operating periods of the year.

11.3.3 *Proportional and integral gain constants*

When it comes to the constants K_P, K_I, they should be selected so that during the simulations the storage charge/discharge cycles in the long term are maintained close to the reference profile with the minimum total dispatch corrections. Strict solution of the given optimization problem is complex and goes beyond the scope of this work [9]. A relatively simple approach is to find, by trial and error, the minimum values of K_P, K_I that allow reasonably accurate and stable control of the storage level variations. During the calculations it might be convenient to express the proportional and integral gain constants via non-dimensional multipliers k_p, k_i as follows:

$$K_P = k_p Q_{max}/V_{aver}, \quad K_I = k_i K_P \tag{11.20}$$

The performed tests show that (a) the gain constants increase with imprecision in the power thresholds and reference storage profile, as expected; and (b) the integral control component usually can be ignored in case of pure energy storage.

11.4 ADVANTAGES AND LIMITATIONS

The main advantages of the proposed methodology for modeling ESS dispatch in SMC-based reliability studies are the following:

(a) Generality and flexibility. The approach can be applied to systems with various mix and types of ESS, renewable and conventional generation.

(b) Natural combination of ESS normal and emergency operations. Since ESS is deployed to reduce RES curtailments and DPG capacity within each operating cycle, ESS normal operation is complementary to that in emergency situation, in other words, there is no need in ad-hoc weight coefficient to define the production distribution between normal and emergency conditions.

(c) More realistic simulation of storage level variations achieved by dispatch corrections based on proportional integral controller technique

(d) Reduced data requirements. The initial ESS data comprise main technical parameters and their constraints, long-term average storage level and capacity factor in consumption mode (if applicable), which are usually available. The model control parameters – power thresholds, reference storage profile and storage level control constants – are determined according to the proposed special procedures.

(e) Other possible applications. Despite the adopted simplifications, simulations using the new dispatch model provide important insights on expected operation of ESS. This could be useful at initial feasibility studies, particularity, for generation mix optimization, storage sizing and control design.

The new ESS dispatch model also has a number of shortcomings, which can be the focus of future research. The main limitations are related to:

- Dispatch of more complex types of ESS, such as multi-reservoir hydroelectric systems used not only for power generation, but also for water supply to public, industry and agriculture. The challenge in this case is to determine the dispatch for other purposes W_{out}.
- Emergency dispatch of a long sequence of ESS, such as hydro power cascade. The problem is that the emergency situation is defined by comparing the available thermal generation capacity and residual load without taking into account the firm capacity provided by downstream ESS, and as a result, the emergency loading of upstream ESS becomes overestimated.
- Simultaneous dispatch of several ESS with the same operating cycle length
- Lack of a standard procedure for identification of proportional and integral gain constants used in storage level control

11.5 NUMERICAL EXAMPLE

A simple GSA study based on SMC simulations has been performed to demonstrate the new ESS dispatch model. The study focuses on a generation system comprising thermal power plants and a single hydroelectric ESS. The selected case scenarios combine different ESS types (HPP, PSP), operating time frames (annual and daily) and control strategies (proposed, pure reliability). The simulations are done in Matlab.

11.5.1 *Data and methodology*

System load and DPG. The annual load profile from the IEEE reliability test system [146], comprising $t_Y = 8736$ hourly[2] values with the peak of 2700 MW, is assumed to represent the average annual profile (Fig. 11.3). The actual load sequence L_{sys} is generated by adding to this average profile Gaussian noise with a 672-hour and 2-hour time resolutions, which allows simulating monthly and intraday random variations in demand. The standard deviation of both Gaussian noise components is set to 5%.

Thermal generation data based on [146] are presented in Table 11.1. The total DPG capacity is 2705 MW. When creating the sequence of available capacity CAP_{avail} the forced outages and repairs of thermal units are simulated by using a two-state model as described in [18].

Energy storage. The analysis includes one HPP with an annual (ESS1, $t_C = 8736$) and one PSP with a daily (ESS2, $t_C = 24$) operating cycle. The data and methods adopted to model the given hydroelectric ESS are largely based on [4].

The general equation for power conversion (11.6) is substituted by:

$$V = A + B\,H_h + C\,H_h^2 \tag{11.21}$$

$$P = \eta_h\,\rho\,g\,H_h\,Q \text{ (if } Q > 0), \quad P = \frac{\rho\,g\,H_h\,Q}{\eta_h} \text{ (if } Q < 0), \tag{11.22}$$

where A, B, C are the constant describing the reservoir geometry; H_h is the net hydraulic head; η_h is the head-to-power efficiency (same in pumping mode); ρ is the water density; and g is the gravitational constant. The values of the main design parameters are summarized in Table 11.2.

The water inflow series W_{in} for ESS1 is generated on a monthly basis by applying Gaussian perturbations with standard deviation of 5% to one of the three randomly selected (with equal probability) average annual profiles given in Table 11.3. The hourly inflows, assumed to be the same within each month, are obtained simply by dividing the monthly value by 672. To fit the output capacity factor $CapFac_{out}$ to the required 10%, the original values of the mean water inflows from [4] are multiplied by 40. In case of PSP this is achieved by setting $CapFac_{in} = CapFac_{out}/\eta_h^2 = 10/0.9^2 = 12.3\%$[3]. The water loss W_{loss} and usage for other purposes W_{out} are ignored.

2 The IEEE reliability test system defines a year as 8736 hours, 364 days or 13 months.

3 The simplified relation $CapFac_{in} = CapFac_{out}/\eta_h^2$ is obtained based on (11.1) and (11.22) by assuming that the hydraulic head H_h is constant.

The additional cases with pure reliability based control strategy are simulated by setting $F_{out}=\infty$ and $k_p=k_i=0$, which assures that the storage is discharged only in emergency situation.

GSA assessment. Monte Carlo simulations are performed with $N_Y=500$ sampling years. GSA is analyzed simply by combining the series of residual load, available generation capacity and the resultant ESS production/consumption. For comparability reasons the same sequences of L_{sys}, W_{in} and CAP_{avail} are used during the simulations, which means that in all scenarios the emergency situation periods are expected to be the same. The selected reliability indices are: loss of load expectation (LOLE), loss of energy expectation (LOEE) and loss of load frequency (LOLF).

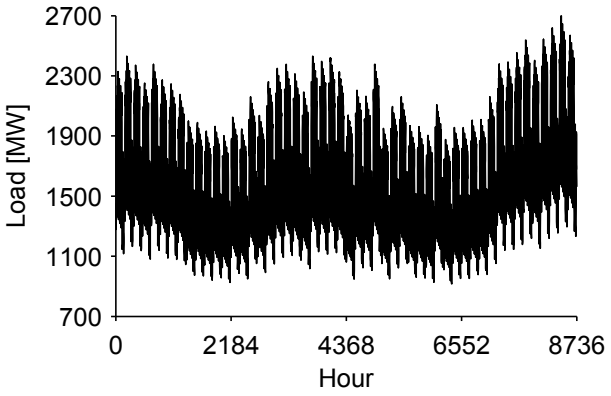

Figure 11.3: Average annual load profile

Unit size [MW]	Number of units [–]	Time to failure [hour]	Time to repair [hour]
12	5	2940	60
20	4	450	50
76	4	1960	40
100	3	1200	50
155	4	960	40
197	3	950	50
350	1	1150	100
400	2	1100	150

Table 11.1: Thermal generation reliability data

Parameter	ESS1/ESS2
P_{max} [MW]	300
P_{min} [MW]	0
Q_{max} [m^3/s]	318
Q_{min} [m^3/s]	0
η_h [−]	0.9
A	40/0.2
B	2.22/0.0111
$C \times 10^6$	48200/241
V_{max} [hm^3]	2000/10
V_{min}	$0.05 \times V_{max}$
V_{aver}	$0.5 \times V_{max}$
$CapFac_{out}$	10%

Table 11.2: Assumed data for hydroelectric ESS

Month	Wet	Dry	Normal
1	82	48	50
2	136	58	78
3	184	94	120
4	228	116	168
5	124	56	80
6	96	44	64
7	72	32	48
8	48	20	32
9	48	20	32
10	48	16	28
11	72	32	40
12	72	40	64
13	112	48	72

Table 11.3: Monthly precipitation-based water inflows in hm^3 for ESS1 (HPP)

11.5.2 *Simulation results*

The calculations are performed using Matlab on a workstation (Intel Xeon W3503, 12 GB RAM, 2.4 GHz) with the execution time per sampling year of up to 0.6 seconds.

To simulate ESS operation sequence for GSA assessment, first, residual load RL and its components are calculated. Since renewable production is excluded and only one ESS is considered at a time, according to (11.7) the system load and RL are the same. The trend and detrended components of the residual load are found from (11.8) and (11.9). As shown in Fig. 11.4 the resultant profiles vary significantly depending on the length of ESS operating cycle.

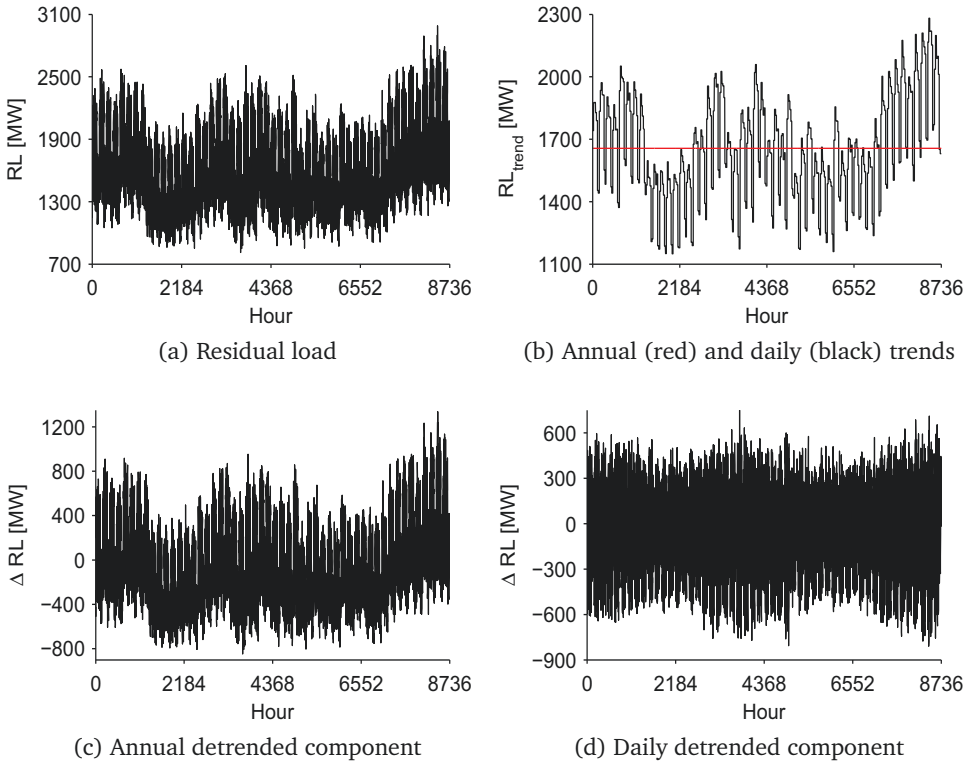

(a) Residual load

(b) Annual (red) and daily (black) trends

(c) Annual detrended component

(d) Daily detrended component

Figure 11.4: Residual load and its components for simulation year 1

In the next step the control parameters are determined. The reference storage profiles $\widehat{V}_{ref}$ are found based on ESS dispatch for average annual conditions as described in Section 11.3.1. For ESS1 (HPP) the selected intermediate and final results of the given procedure are presented in Fig. 11.5. The analysis is performed directly for the whole year, which is the operating period ($N_P = 1$). The power threshold in this case characterizes to which extent $\widehat{\Delta RL}$ profile is leveled by the plant production (Fig. 11.5a) and it is determined by gradually lowering $\widehat{F}_{out}$ from the maximum until the resultant total water outflows balance with the precipitation-based water inflows (Fig. 11.5b). Finally, by using (11.17), (11.18) the cumulative net water inflows and the reference storage levels are calculated (Fig. 11.5c). No averaging is required, as there is only one operating period and thus one storage profile (Fig. 11.5d).

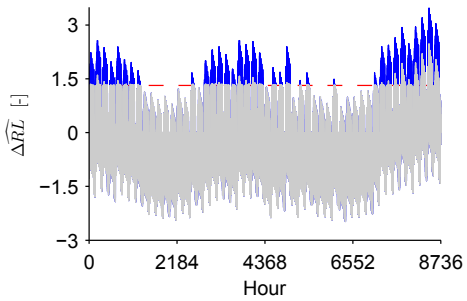

(a) Leveling of the average detrended residual load (threshold $\widehat{\mathrm{F}}_{\mathrm{out}}$ is shown in dashed red)

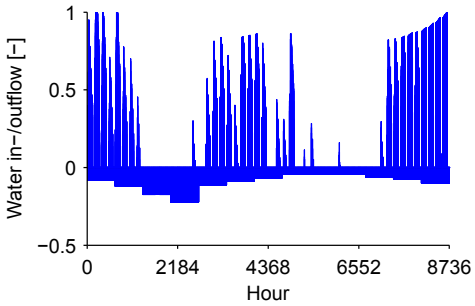

(b) Expected average annual variation of water in-/outflow

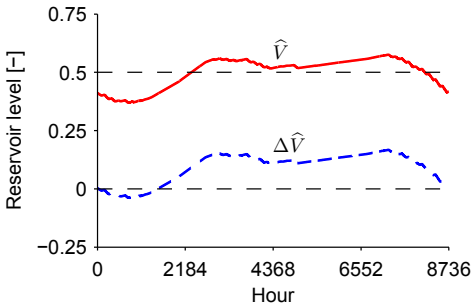

(c) Cumulative variation of water inflow (dashed blue) and the reference storage profile (red)

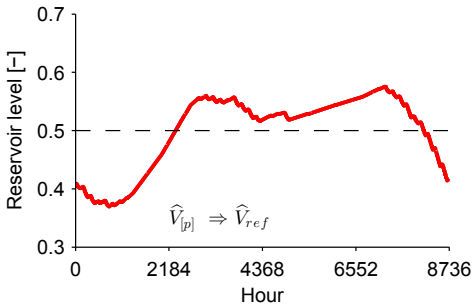

(d) Reference storage profile (averaging is not required in this case)

Note: The parameters are normalized by $\mathrm{P}_{\mathrm{max}}$, $\mathrm{Q}_{\mathrm{max}}$ and $\mathrm{V}_{\mathrm{max}}$, respectively.

Figure 11.5: Identification of reference storage profile for ESS1 (HPP)

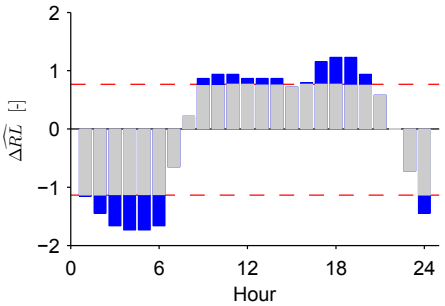

(a) Leveling of the average detrended residual load for day 1 (thresholds $\widehat{\mathrm{F}}_{\mathrm{in}}$, $\widehat{\mathrm{F}}_{\mathrm{out}}$ are shown in dashed red)

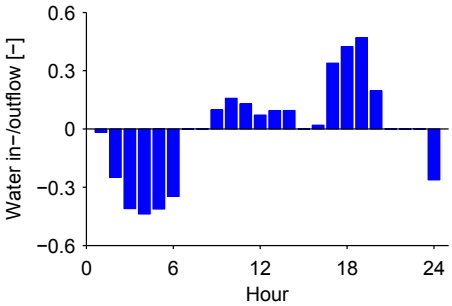

(b) Expected average variation of water in-/outflow for day 1

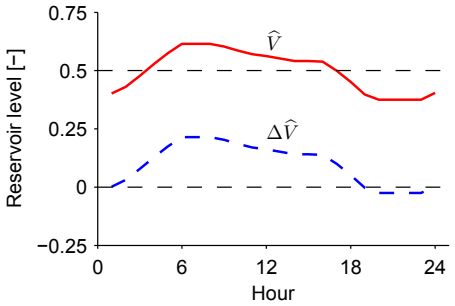

(c) Cumulative variation of water inflow (dashed blue) and the reference storage profile (red) for day 1

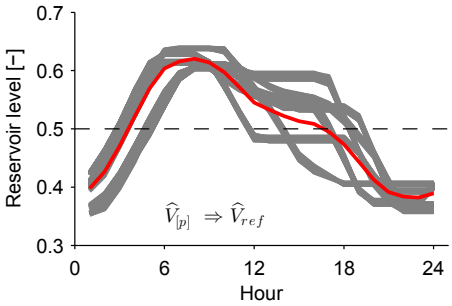

(d) Reference storage profiles for all days (grey) and their average (red)

Note: The parameters are normalized by $\mathrm{P}_{\mathrm{max}}$, $\mathrm{Q}_{\mathrm{max}}$ and $\mathrm{V}_{\mathrm{max}}$, respectively.

Figure 11.6: Identification of reference storage profile for ESS2 (PSP)

The corresponding results from the identification of reference storage profile for ESS2 (PSP) are presented in Fig. 11.6. The difference is that the procedure now is repeated for each day of the year. The power thresholds define the valley filling and peak shaving of $\widehat{\Delta RL}$ profile segment for the given day (Fig. 11.6a). First, $\widehat{F}_{in}$ is determined by gradually increasing it from the minimum until the capacity factor in consumption mode equals to the specified value and then $\widehat{F}_{out}$ is calibrated by balancing the resultant water in-/outflows (Fig. 11.6b). By integrating the latter, the reference storage profile is obtained (Fig. 11.6c), which afterwards together with the remaining daily profiles is averaged to give $\widehat{V}_{ref}$ (Fig. 11.6d). In this case there are six distinct groups among the resultant individual reference storage profiles. And the reason is that the original annual demand profile from IEEE reliability test system is based on six daily load distributions [146].

As noted earlier, $\widehat{F}_{in}$ and $\widehat{F}_{out}$ strictly are valid only for the average annual operating conditions. The actual power thresholds F_{in}, F_{out} are estimated based on the complete sequence of detrended residual load by following the calculation steps in Section 11.3.2. For ESS1 (HPP) only F_{out} is applicable and it is equal to 410 MW, whereas for ESS2 (PSP) the thresholds have separate values for each day (operating period) of the year and capture the seasonality of the residual load as shown in Fig. 11.7.

Compared to the power thresholds used at the average annual conditions, the actual thresholds are larger in magnitude. For ESS1 the difference is 15 MW (peak shaving) and for ESS2, on average, it is 27 MW (peak shaving) and 5 MW (valley filling).

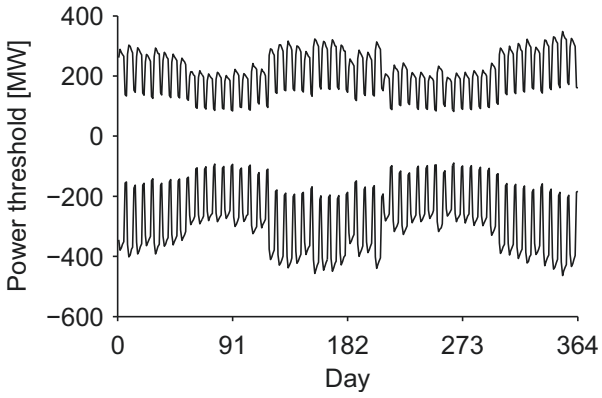

Figure 11.7: Power thresholds for ESS2 (PSP)

The remaining control parameters for ESS dispatch model, the multipliers k_p, k_i in (11.20), are determined through trial and error by keeping the deviation between the simulated average reservoir level and V_{aver} within 3%. The trial simulations are run for the period of 50 years, which is found to be sufficient. The obtained, not necessarily optimal, values of the multipliers are:

$$k_p = 0.8,\ k_i = 0.1 \text{ for ESS1 and } k_p = 0.4,\ k_i = 0 \text{ for ESS2}$$

Once all dispatch control parameters are defined, full simulations of ESS operation are performed. The resultant average cycles of simulated storage level and power are compared with the expected profiles in Fig. 11.8. The reservoir level and power variations during the selected periods including capacity shortages are presented in Fig. 11.9. The results clearly demonstrate the effectiveness of the new model in integrating ESS dispatch for both normal and emergency conditions and achieving realistic simulation of the storage level variations. One can also observe that the impact of the capacity shortages on ESS operation reduces with increased storage volume.

Finally, in the last step all production and consumption series are combined and GSA is evaluated. The calculated reliability indices are summarized in Table 11.4. The initial system configuration ('no ESS') comprises only the system load and the dispatchable generation. The reliability indices in this case, of course, differ from the values corresponding to the IEEE reliability test system [146] due to the applied modifications. The results show that the system adequacy improved with the aggregated daily pumped storage. The reliability gain was even higher with the conventional hydro plant what can be explained by the increased reservoir capacity and the precipitation-based inflows. As expected, the adequacy predictions obtained with the proposed dispatch model were more conservative compared to that from the pure reliability based approach.

	LOLE [hour/year]	LOEE [MWh/year]	LOLF [occ./year]
ESS1 (HPP)	15.5 (6.7)	914 (823)	5.0 (2.4)
ESS2 (PSP)	44.8 (42.9)	2940 (2284)	13.0 (12.4)
no ESS	47.9	7311	13.8

Note: The reliability indices corresponding to pure reliability based dispatch model are given in brackets.

Table 11.4: Reliability indices for the system configurations with and without ESS

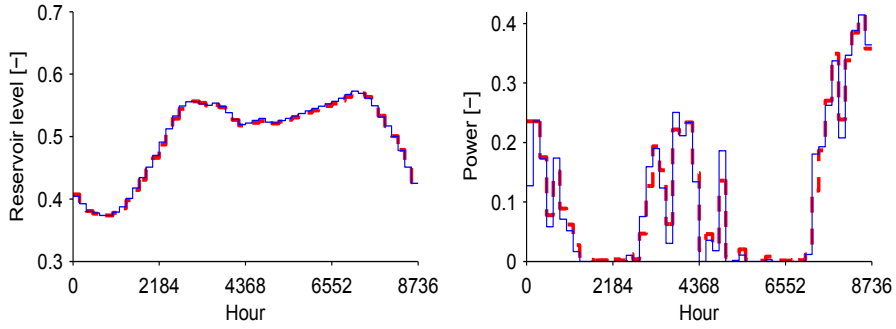

(a) ESS1, storage level (b) ESS1, power

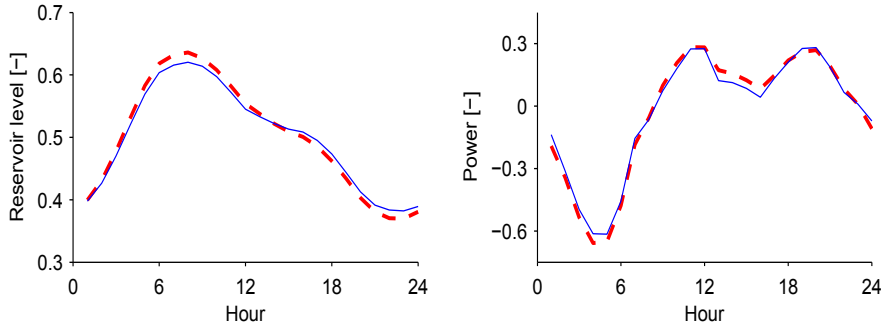

(c) ESS2, storage level (d) ESS2, power

Note: In case of ESS1 weekly average values are shown for improved visibility.

Figure 11.8: Average profiles of simulated reservoir level and power (dashed red) versus the expected profiles (blue)

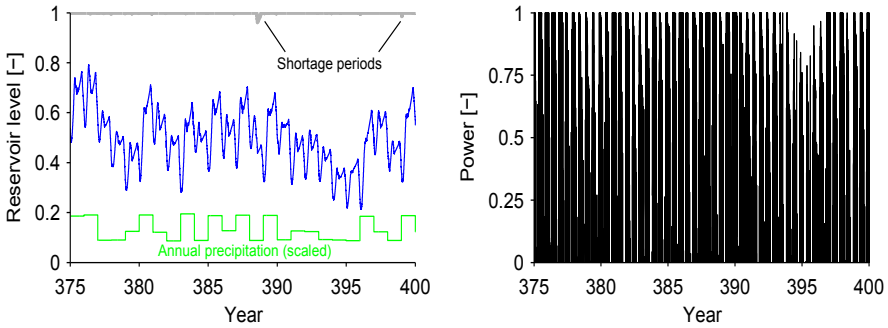

(a) ESS1, storage level (b) ESS1, power

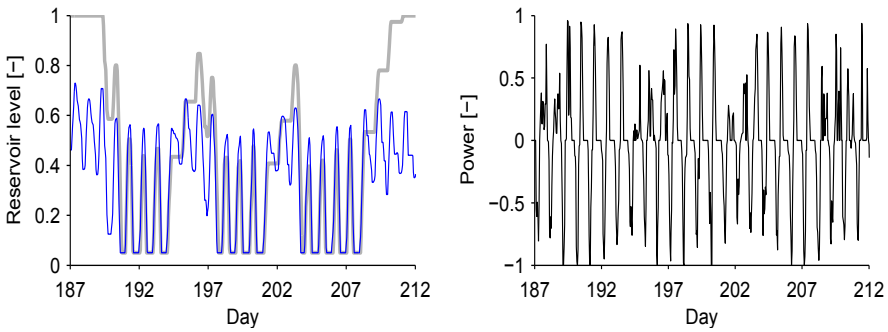

(c) ESS2, storage level (year 389) (d) ESS2, power (year 389)

Note: The storage level variations obtained with the proposed and pure reliability based dispatch controls are shown in blue and grey, respectively.

Figure 11.9: Simulated reservoir level and power during selected time interval

11.6 CONCLUDING REMARKS

A new methodology was proposed for modeling energy storage dispatch in generation system adequacy evaluations based on the sequential Monte Carlo simulations. Aimed for generality and flexibility, the methodology can be applied to the systems with various mix and types of ESS, renewable and conventional generation. The required input data for ESS are easily available and include: main technical parameters and their constraints, long-term average storage level and capacity factor in consumption mode.

According to the developed approach, energy storage is deployed to reduce RES curtailments and DPG capacity, which allows natural combination of its normal and emergency operations. The main novelties in this case are: (a) the use of detrended residual load during ESS control to be able to consider renewable power production and distinguish between different operating timescales, and (b) the correction of ESS dispatch based on the classical proportional integral controller technique to achieve a realistic representation of storage level variations.

The individual calculation steps of the proposed methodology were demonstrated through a simple adequacy analysis of a generation system comprising thermal power plants and hydroelectric ESS with annual and daily operating cycles.

The proposed modeling methodology also opens up possibilities for other applications beyond the reliability assessment studies as the new dispatch model provides an important insight on the expected operation of ESS. It is important to note that certain aspects of the work presented in this thesis require further investigation and development. The main challenge of future research is related to dispatch of more complex types of ESS, such as multi-reservoir hydroelectric systems used not only for power generation.

Part V

CASE STUDY

12 CASE STUDY

In Part V of the thesis the previously proposed solar energy models and energy storage dispatch model are applied to a case study of generation system adequacy (GSA) in peninsular Spain.

12.1 OBJECTIVES

The objective of this case study is, first, to demonstrate how the new solar power and energy storage models can be used for GSA assessment based on the sequential Monte Carlo (SMC) simulations, and second, to obtain knowledge on generation adequacy in peninsular Spain. Considering inherently high computational cost of SMC simulations, the scope of the study has been limited. The chosen focus areas are: (a) adequacy of the existing Spanish generation system and the level of redundancy; (b) capacity credit[1] of time-dependent power sources, i. e. renewables and energy storage; and (c) sensitivity of the final results to certain modeling aspects.

12.2 DATA AND METHODOLOGY

12.2.1 *General description*

To evaluate GSA, the following elements of the Spanish power system are considered:

- System load
- Thermal generation
- Renewable energy sources (RES) comprising wind, solar and run-off-the-river (ROR) hydro power production
- Energy storage systems (ESS) formed by reservoir-based hydro power

Solar power is represented by photovoltaic (PV) and concentrated solar power (CSP) plants. The latter employs parabolic trough and central tower technologies.

To simplify the data collection and the subsequent simulations, the hydroelectric system in the Spanish peninsula is substituted by one equivalent ROR, one conventional hydro power (HPP) and three pumped storage (PSP) plants with annual, weekly and daily operating cycles. ROR is treated as a part of non-dispatchable renewable generation, whereas HPP and PSP – as energy storage. To allow PSP with a weekly cycle, the year is assumed to consist of 52 full weeks, 364 days or 8736 hours.

1 In this work the terms 'capacity credit', 'capacity value' and 'capacity contribution' are used interchangeably.

The reference production and capacity values for RES and ESS are taken from [64] and summarized in Table 12.1. As one can see, the present (2013) and future (2020) time scenarios are considered for wind and solar energy, whereas hydro power is assumed to remain the same. The installed wind and solar capacity values from [64] are not used in the calculations and are shown only for comparison purposes.

Scenario		Wind	PV	CSP	ROR	HPP	PSP
2013	[GWh]	49666	8202	6375	5866	26681	6592
	[GW]	24.50 (23.8)	4.89 (5.1)	2.47 (2.5)	1.95	11.5	5.36
2020	[GWh]	73485	12356	14379			
	[GW]	35.76 (35.2)	7.25 (7.7)	4.80 (5.4)			

Note: The actual capacity values after calibration of the corresponding data series are shown in brackets.

Table 12.1: Reference values for wind, solar and hydro power in Spain [64]

Each adequacy analysis based on the sequential Monte Carlo technique involves three general steps: (a) preparation of the sequences for the system load, RES production and available thermal capacity; (b) simulation of ESS operation to obtain the corresponding production/consumption sequences; and (c) superimposition of all time series and calculation of reliability indices, namely, loss of load expectation (LOLE), loss of energy expectation (LOEE) and loss of load frequency (LOLF). The number of sampling years is chosen so that the final variance of the reliability indices is less than 0.5%. Naturally, the higher adequacy of the system, the more sampling years are required to achieve the given precision.

The excess of thermal generation and the capacity contributions of the time-dependent sources are expressed by the effective load carrying capability (ELCC). According to the procedure described in Section 2.2, ELCC is determined through repetitive GSA calculations for a given scenario by gradually increasing the system load across all hours until the resultant adequacy level approaches the target value. The matching is done with an error of less than 0.5%. For comparability reasons during the iterations the same time series are used for system load, available thermal generation capacity, RES production and reservoir water inflows.

All scenarios are named based on the types of ESS and RES considered. If relevant, the system load increment ΔL_{sys} is also mentioned.

The following subsections describe in detail the modeling of system load, thermal generation, wind, solar and hydro power.

12.2.2 *System demand*

The study deploys four annual load profiles based on the actual values of the Spanish system demand for the period of January 4, 2010 (Monday) – December 29, 2013 (Sunday) [126]. The load sequence during the simulations is created by randomly choosing for each year one of the given profiles. The peak load is 44.12 GW and the average annual demand is 252,540 GWh. As shown in Fig. 12.1 the system load exhibits strong seasonal, weekly and daily trends, which justifies the use of energy storage at the corresponding timescales.

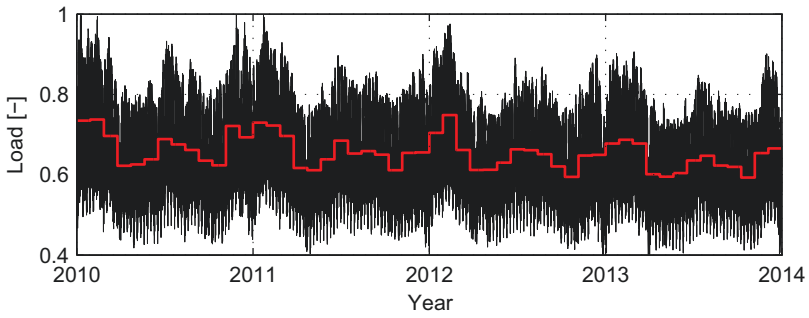

(a) Hourly (black) and monthly (red) values for 2010-2013 period

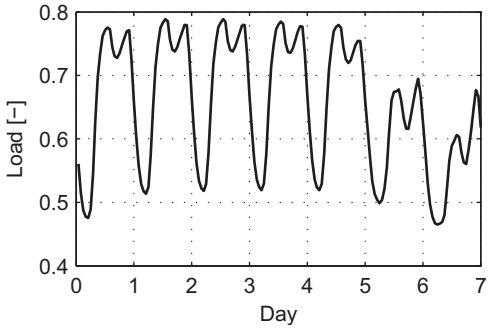

(b) Weekly average profile

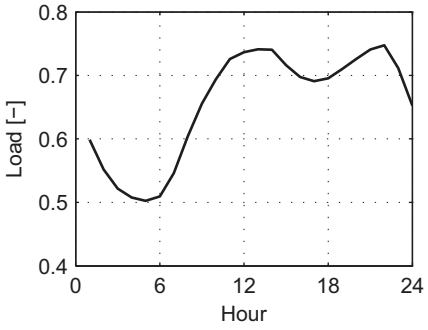

(c) Daily average profile

Figure 12.1: Historical system load values

12.2.3 *Thermal generation*

Thermal generation in Spain is approximated by 35 coal-based (total of 11.2 GW), 50 combined cycle (total of 25 GW) and 8 nuclear (total of 7.8 GW) power units according to the data from [126]. The total capacity is 44 GW. The units of each category are assumed to be of the same size equal to the average. The corresponding reliability data are taken from [105] and summarized in Table 12.2.

The forced outages and repairs of thermal generation units are simulated by using a two-state model and then combined to obtain the final sequence of the available system capacity as described in Section 2.1.

Plant type	Unit size [MW]	Number of units [–]	Outage rate [%]	Time to failure [hour]	Time to repair [hour]
Coal	320	35	4.95	845	44
Comb. cycle	500	50	5.05	672	36
Nuclear	975	8	3.93	6251	256

Table 12.2: Thermal generation reliability data

12.2.4 *Wind power*

The initial data for wind production in Spain are based on the normalized and detrended (to account for the growing installed capacity) historical series covering the period of 2007–2010 [126]. As shown in Fig. 12.2 the wind generation has a seasonal pattern correlated with the system demand. The trends over shorter timescales are negligible.

The wind power sequence during the simulations is created by randomly choosing for each year one of the given annual profiles and then by scaling the whole series to the required production level (Table 12.1).

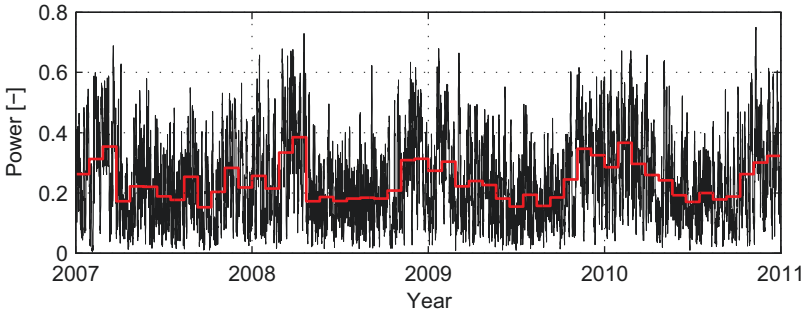

Figure 12.2: Historical hourly (black) and monthly (red) wind power values

12.2.5 *Solar power*

The solar power production sequences are created in four steps. First, by using the models presented in Part II synthetic solar radiation data are generated for 52 locations distributed evenly across peninsular Spain with grid spacing of 0.5° as shown in Fig. 12.3. The required monthly average radiation values are taken from [102]. The length of the time series is reduced to 8736 hours per year simply by excluding the 365th day of the year from the initially created solar radiation sequence.

Second, based on the models proposed in Part III solar radiation is translated into power production for 52 PV, 12 parabolic trough and 12 central tower plants. The CSP locations are limited simply by applying the annual direct radiation threshold of 2100 kWh. Each PV plant has the capacity of 100 MW and deploys Siemens SP-75 modules, whereas CSP plant is based on solar

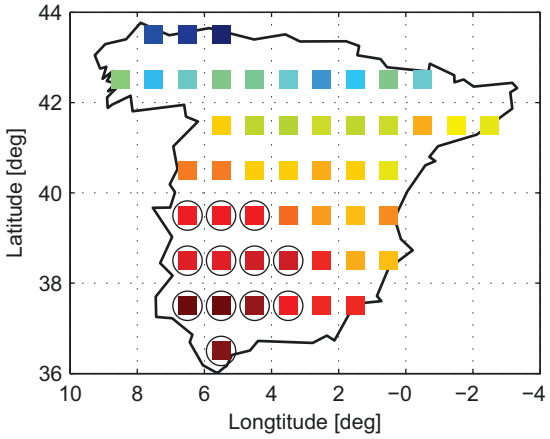

Figure 12.3: Selected locations for PV (square) and CSP (circle) plants

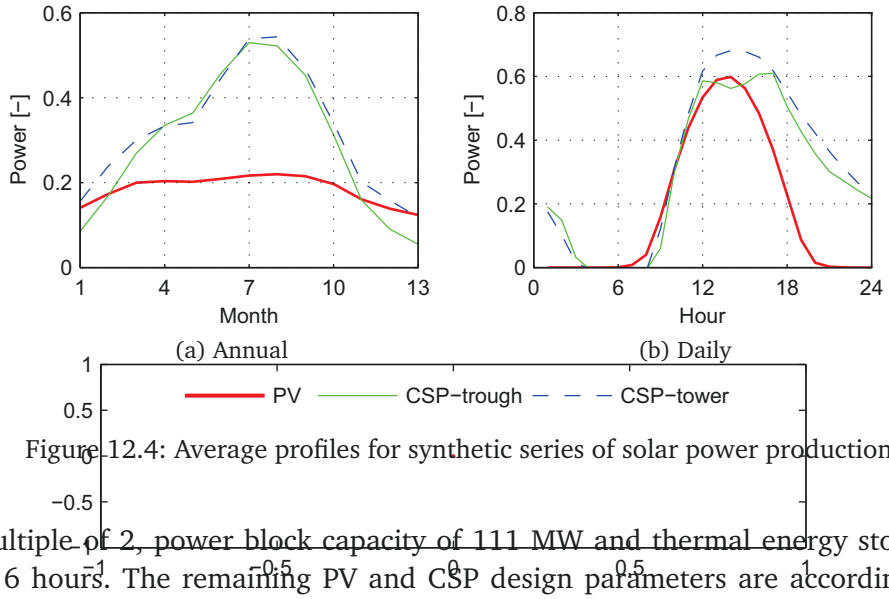

(a) Annual (b) Daily

Figure 12.4: Average profiles for synthetic series of solar power production

multiple of 2, power block capacity of 111 MW and thermal energy storage of 6 hours. The remaining PV and CSP design parameters are according to Sections 8.4 and 9.6, respectively.

Third, the individual production series are combined for each solar technology. To imitate the variation in contribution of different locations the relative weighting is applied based on the mean total (for PV) and direct (for CSP) radiation values. The average annual and daily profiles from the resultant sequences are shown in Fig. 12.4.

And finally, the solar power series is scaled to the required production level (Table 12.1). In this case the share of CSP-trough in 2013 and 2020 scenarios is assumed to be 100% and 60%, respectively.

It is important to note that even though the average annual profile remains the same, incorporation of the monthly and daily spatial correlations of solar radiation (SCSR) affects significantly the ramp rates in the total power production as shown in Table 12.3.

	PV	CSP-trough	CSP-tower
without SCSR	4.4 (9.1)	14.4 (27.5)	17.5 (23.4)
with SCSR	19.1 (11.6)	36.8 (29.4)	45.4 (27.2)

Table 12.3: Mean ramp rates in daily (monthly) solar power production as percentage of the average production value

12.2.6 *Run-of-the river hydro power*

The hydro power calculations begin with defining the precipitation series. In this work the initial data comprise daily precipitation values (in mm) at 0.2° spaced grid points across the Spanish peninsula during the period of 1950–2007; and are taken from the publicly available dataset 'Spain02' [60]. The total daily precipitations are estimated by averaging the corresponding values from the individual locations and multiplying by 494,020 km^2, the area of the peninsula. The intraday distribution of precipitation is assumed to be uniform. The monthly and annual average values from the resultant sequence of the hourly precipitations Z are shown in Fig. 12.5. The overall mean is 34.61 hm^3/hour. During Monte Carlo simulations the given data segment is repeated each 58 years. According to [29] the application of such relatively short precipitation time series should be sufficient for GSA assessment.

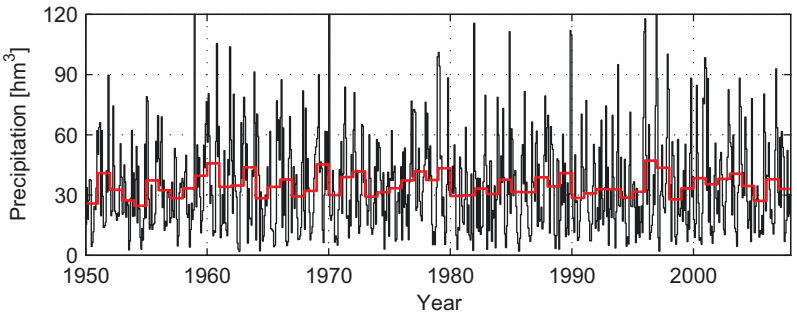

Figure 12.5: Monthly (black) and annual (red) average hourly precipitation for 1950-2007 period

In the next step the ROR power P_{ror} sequence is determined. It is done simply by scaling the corresponding precipitation values considering that at constant head the hydro power is directly proportional to water inflow, which, in turn, is proportional to the received precipitation [96]. The reference annual energy production $AEP_{ror,ref}$ and maximum capacity $P_{ror,nom}$ are taken from Table 12.1. Starting with initialization $P_{ror} = Z$, the scaling is performed by repeating the following steps several times:

1. Adjust the variation of the series as

$$P_{ror} = P_{ror}\, AEP_{ror,ref}/8736/\mathtt{mean}(P_{ror}),$$

   and limit the overshoots by the nominal power $P_{ror,nom}$).

2. Adjust the constant component of the series as

$$P_{ror} = P_{ror} + AEP_{ror,ref}/8736 - \mathtt{mean}(P_{ror}),$$

   and again limit the overshoots by $P_{ror,nom}$. The given step is required because the precipitation sequence used to initialize the calculations reflects only the variation of the ROR power production and ignores its constant component.

The average annual profile for the resultant power series is given in Fig. 12.6.

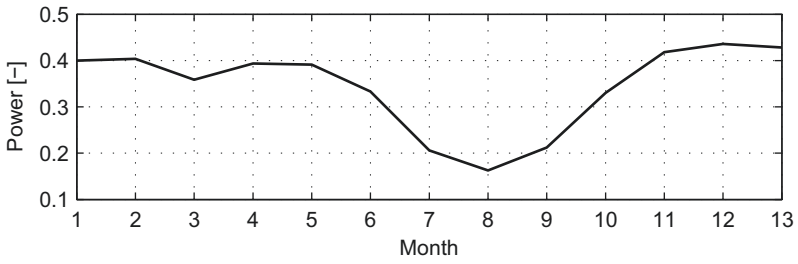

Figure 12.6: Average annual profile of ROR power production

12.2.7 *Reservoir-based hydro power*

Hydroelectric energy storage is represented by one equivalent HPP and three PSP with annual, weekly and daily operating cycles. PSP-year is of mixed type, whereas PSP-week and PSP-day are pure pumped storage. As shown in Table 12.1 the reference annual generation and installed capacity values are 26681 GWh, 11.5 GW for HPP and 6592 GWh, 5.36 GW for PSPs.

The hydroelectric plants are modeled based on the methodology and the numerical example described in Part IV. The power conversion is defined by equations (11.21) and (11.22). The required inputs comprise: the lower and upper limits for water (dis)charge $Q_{min(max)}$, power $P_{min(max)}$ and reservoir water volume $V_{min(max)}$; head-to-power efficiency η_h; reservoir geometry constants A, B, C; capacity factors in consumption $CapFac_{in}$ and production $CapFac_{out}$ modes; long-term average reservoir level V_{aver}; series of natural water inflow into reservoir W_{in}; and dispatch order. The water usage for other purposes and storage losses are ignored $W_{out}=W_{loss}=0$.

Plant parameters

The adopted values of the plant parameters are summarized in Table 12.4. The reservoir capacities V_{max} and nominal powers P_{max} for PSPs are estimated based on [64, 93, 95, 127]. V_{max} for HPP is obtained by subtracting PSP reservoir capacities from the expected total of 22000 hm^3 [64].

The values of C, P_{min}, Q_{min}, V_{min} and η_h are selected based on the author's judgment. Note that $C=0$ implies linear relation between the reservoir water volume and the hydraulic head.

Parameter	HPP	PSP-year	PSP-week	PSP-day
P_{max} [GW]	11.5	2.66	1.16	1.54
Q_{max} [m^3/s]	2085	482	733	7856
V_{max} [hm^3]	15224	6275	198	303
$A \times 10^{-6}$	−11418	−4706	−149	−227
$B \times 10^{-6}$	40.29	16.60	1.82	22.57
$CapFac_{in}/CapFac_{out}$	–/10%	8.7/22%	8.7/6.3%	8.7/6.3%
$P_{min}=Q_{min}=C=0$; $\eta_h=0.85$; $V_{min}=0.3V_{max}$; $V_{aver}=0.69V_{max}$				

Table 12.4: Assumed data for reservoir-based hydro power plants

The parameters A, B, Q_{max}, V_{aver} are determined according to the procedure described in Appendix B. The additional inputs in this case are the ratio between the minimum and maximum head λ_H, reservoir maximum E_{max} and average E_{aver} energy capacity. λ_H for all plants is assumed to be 60%. The total E_{max} is 18500 GWh and E_{aver} is approximately 50% [126]. For PSP-week and PSP-day E_{max} is taken to be equivalent to 42- and 6-hour (25% of operating cycle) full discharge. The remaining reservoir energy capacity is divided between HPP and PSP-year in proportion to their reservoir volumes.

Finally, the capacity factors are estimated as follows. For HPP the expected value is

$$26681/(11.5\times 8736)=0.266,$$

which during the preliminary simulations is found to be too large for load leveling. Considering this, $CapFac_{out}$ is set to 10% based on the author's judgment and the remaining 16.6% is treated as a base production. The latter is incorporated into ESS dispatch model simply by using an additional calculation step where the last value of Q is increased by a given fixed amount and the related parameters are updated with possible adjustments according to (11.2)–(11.4).

Taking into account that the average annual power consumption due to pumping is 4059 GWh [126], $CapFac_{in}$ for all PSPs becomes

$$4059/(5.36\times 8736)=0.087.$$

By multiplying the given value by the square of the conversion efficiency one obtains $CapFac_{out}$ for PSP-week and PSP-day: $0.087\times 0.85^2=0.063$.

The combined annual generation from pure storage plants equals to

$$2.7\times 8736\times 0.063=1486 \text{ GWh},$$

based on which $CapFac_{out}$ for PSP-year is calculated as

$$(6592-1486)/(2.66\times 8736)=0.22.$$

Natural water inflow into reservoir

Since, as noted earlier, the water inflow and precipitation are linearly related, the inflows into reservoirs W_{in} can be approximated as:

$$W_{in} = C_w \times Z \tag{12.1}$$

where Z is the hourly precipitation, and C_w is the constant. The latter is tuned during the simulations to obtain the required capacity factor in production mode[2]. The values of the constant for HPP and PSP-year are 0.0712 and 0.0099, respectively.

Interestingly, the division of C_w by the runoff coefficient (ratio of water inflow to precipitation) approximately indicates the fraction of water resources used in reservoir-based hydro power production. For Spain with the runoff coefficient of 32% [96] this share equals to $(7.12+0.99)/0.32=25.3\%$.

2 For HPP the total capacity factor value 26.6% is used.

Dispatch order, control parameters and emergency loading

The operation of the hydroelectric plants is assumed to be independent. Based on the considerations in Section 11.2.1 the dispatch order is: PSP-day, PSP-week, HPP and PSP-year.

The control parameters required for ESS dispatch, namely, reference storage profile $\widehat{V}_{ref}$, power thresholds F_{in}, F_{out} and multipliers k_p, k_i, are obtained according to the procedures described in Section 11.3. The calculated values/profiles of $\widehat{V}_{ref}$, F_{in}, F_{out} vary with the simulation scenarios, whereas the chosen multipliers k_p, k_i are the same in all cases and equal to:

	HPP	PSP-year	PSP-week	PSP-day
k_p	0.8	0.8	0.6	0.4
k_i	0.1	0.1	0.0	0.0

As mentioned in Section 11.4, the developed ESS dispatch model when applied to a sequence of ESS units may result in the overestimation of the emergency loading and thus the disturbance of normal operation of the units that are dispatched first. The reason is that the emergency situation is defined by comparing the available thermal generation capacity CAP_{avail} and residual load RL without taking into account the firm capacity provided by the ESS units dispatched in the subsequent steps.

In this study the excessive emergency loading was observed during trial simulations in case of PSP-day, PSP-week and HPP. To avoid this problem two ad-hoc measures are adopted: (a) direct limitation of the emergency operating periods, and (b) adjustment of the CAP_{avail} time series. The first measure is used only for PSP-week and PSP-day by limiting the emergency situations to the capacity shortages occurring during the usual peak shaving time intervals. The second measure is applied for all the three hydro plants. The emergency loading in this case is reduced simply by adding a constant to the CAP_{avail} time series. The constant value at each scenario is determined by decreasing the relative fraction of the emergency hours seen by PSP-day, PSP-week and HPP to 3.5%, 4.5% and 14%, respectively. The maximum limits of the emergency hours, in turn, are estimated approximately by increasing them until the deviation between the simulated and expected average reservoir level increments by 2–3%.

12.3 RESULTS AND DISCUSSION

The calculations are performed on a workstation (Intel Xeon W3503, 12 GB RAM, 2.4 GHz) with the execution time of up to 0.6 seconds per sampling year and per reservoir-based hydro plant. The obtained results for each of the selected focus areas are summarized below.

12.3.1 *Adequacy and redundancy of the existing generation system*

The SMC-based adequacy assessment of the generation system in peninsular Spain for the year 2013 (scenario 'all ESS, RES-2013') by using 90,000 sampling years has given zero reliability indices. Consistent with the previous studies [84, 92, 128], this result confirms that currently the Spanish generation system is over-dimensioned.

The redundant capacity is determined simply by using the first step of the ELCC procedure (see Section 2.2), according to which the GSA calculations are repeated by gradually increasing the system load time series until the reliability level for the given scenario is matched to the target value. In other words, the generation excess is approximated by the maximum increment in the system load that would still allow a specified minimum adequacy level with the existing generation facilities. By applying this approach with 2500 sampling years per iteration and with the target adequacy level set to the traditional LOLE=2.4 hours/year [106], the redundant capacity is estimated to be 13.8 GW or 31.4% of the total thermal generation. The reliability indices in the final iteration (i. e. with the load increment of ΔL_{sys}=13.8 GW) are: LOLE=2.3 hours/year, LOEE=2540 MWh/year and LOLF=0.9 occ./year.

12.3.2 *Capacity contributions of time-dependent sources*

The capacity values of wind, solar and hydro power in the Spanish power system are evaluated by using the ELCC method (see Section 2.2) with 500 sampling years per iteration. The reliability indices for the reference scenario ('no ESS, no RES') comprising only system load and thermal generation are: LOLE=28.0 hours/year, LOEE=28365 MWh/year, LOLF=10.5 occ./year. The ELCC tuning is done based on the LOEE index considering its relatively higher stability.

The calculated capacity contributions of various types and combinations of time-dependent power sources are given in Table 12.5. For some cases the corresponding estimations from the previous study [128] are also included for comparison. One can observe that:

- Wind, solar and hydro power facilities in Spain altogether have a significant capacity value, reaching currently 16.65 GW ('all ESS, RES-2013').
- As expected, the capacity credit of intermittent sources decreases in relative terms with the increased penetration levels.

- Compared to wind and hydro, solar energy has lower capacity credit when expressed in relative terms. The reason is poor match between the seasonal and daily variations of the solar energy and system load. As a matter of fact, Figs. 12.1 and 12.4 show that the annual peak in electricity demand takes place in winter months and one of the daily load peaks occurs in the evening hours.

- Despite the use of thermal energy storage the capacity credit of CSP is only 7%, which is the same as that of PV. This shows that the CSP dispatch control aimed at maximizing production at each timestep is ineffective from reliability point of view. To increase the capacity value of CSP plant its dispatch strategy should take into account the hours of the daily peak load.

- The capacity value of ROR and reservoir-based hydro is 32% and 56–84%, respectively, which demonstrates the general utility of energy storage in firming intermittent source. The capacity credit is determined, of course, not only by the storage unit, but also by other factors such as the ESS configuration, the shape of the residual load profile at the given operating timescale and sizing of the components. This might explain the variation of the capacity values among the selected four types of ESS.

- The obtained relative capacity values for CSP ('no ESS, CSP-2013') and PSP-day ('PSP-day, no RES') are significantly lower than the corresponding estimations from [128]. The possible reasons lie in the adopted CSP dispatch strategy (as noted earlier) and the excess of the installed PSP power for leveling daily residual load. The given example demonstrates that the capacity credit of the renewable power source coupled with energy storage reflects the inherent intermittency of the source on the one hand, and the effectiveness of such coupling on the other hand.

Scenario	Capacity value		Scenario	Capacity value	
	[GW]	[%]		[GW]	[%]
no ESS, no RES	*reference*		all ESS, no RES	10.95	65
no ESS, RES-2013	5.00	15	all ESS, RES-2013	16.65	33
no ESS, RES-2020	6.25	12	all ESS, RES-2020	18.30	27
no ESS, Wind-2013	3.64	15 (7)	HPP, no RES	8.00	70 (<50)
no ESS, PV-2013	0.35	7 (0)	PSP-year, no RES	2.22	84
no ESS, CSP-2013	0.17	7 (>30)	PSP-week, no RES	0.90	78
no ESS, ROR	0.63	32	PSP-day, no RES	0.86	56 (80)

Note: The capacity contribution in % is calculated with respect to the total nominal capacity of the corresponding time-dependent power source(s). The capacity value estimates from [128] are given in brackets for selected power sources.

Table 12.5: Capacity values of time-dependent power sources for selected scenarios

The results show a large capacity contribution of 10.95 GW from the existing reservoir-based hydro plants (scenario 'all ESS, no RES'). To provide an insight on their operation with the increased penetration of renewables, the average profiles of the simulated ESS storage level and power are presented in Figs. 12.7 and 12.8 for the main scenarios. As one can see, the largest qualitative change occurs at a daily timescale (PSP-day) primarily due to the solar power. At longer timescales, however, the impact of renewables is relatively small, which implies that the available total water reservoir capacity in Spain is sufficient to accommodate very high share of intermittent electricity.

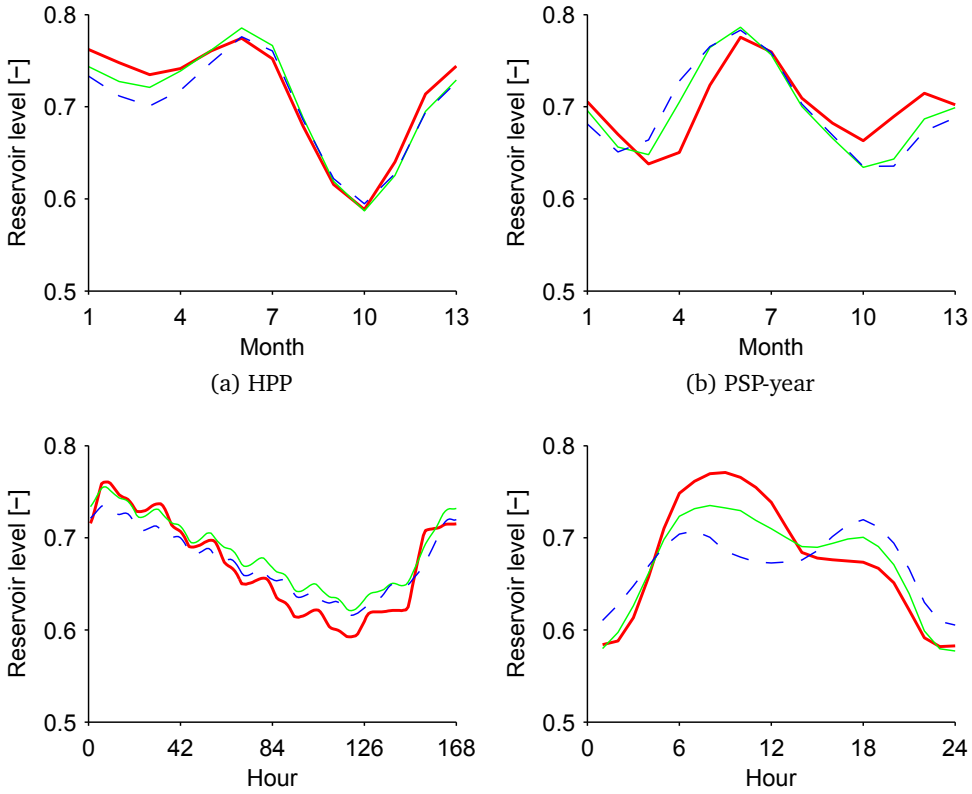

(a) HPP (b) PSP-year

(c) PSP-week (d) PSP-day

Figure 12.7: Average profiles of the simulated ESS storage level: all ESS combined with no RES (red), with RES-2013 (green) and with RES-2020 (dashed blue)

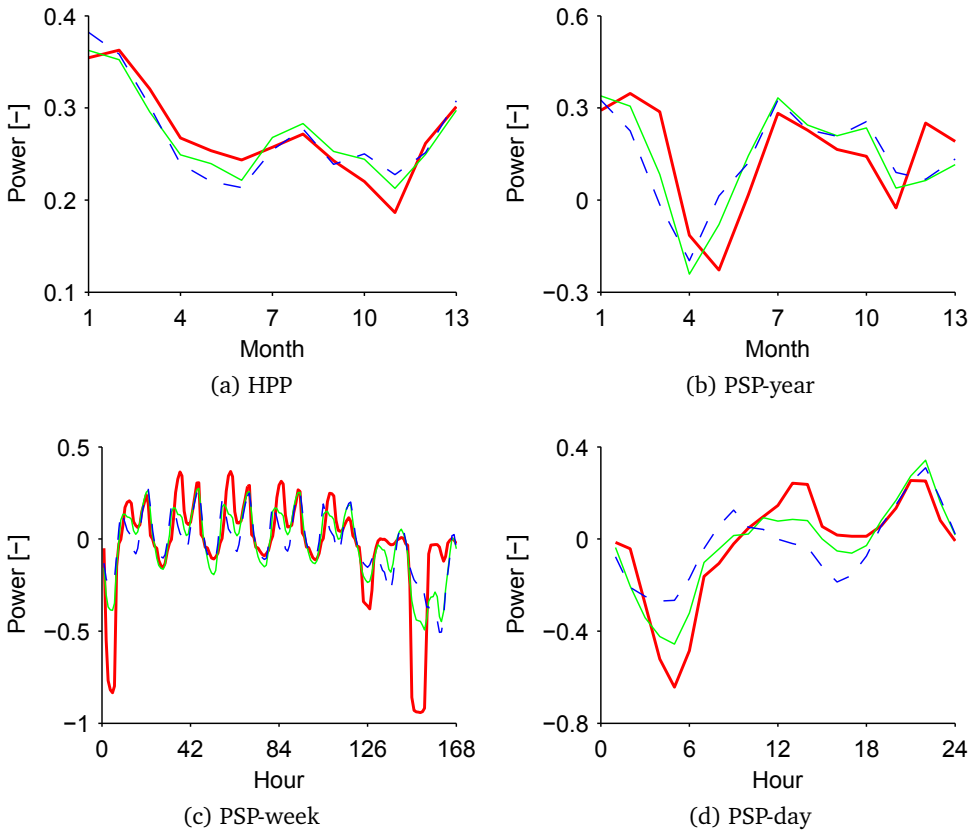

(a) HPP (b) PSP-year

(c) PSP-week (d) PSP-day

Figure 12.8: Average profiles of the simulated ESS power: all ESS combined with no RES (red), with RES-2013 (green) and with RES-2020 (dashed blue)

12.3.3 *Sensitivity analysis*

Finally, a small additional study is performed to check how the reduction of the original (without repetitions) length and the exclusion of the spatial correlation in the solar power production time series affect the capacity credits of PV and CSP plants. This is done by applying necessary modifications to the scenarios 'no ESS, PV-2013' and 'no ESS, CSP-2013', recalculating the PV and CSP capacity contributions and then comparing them to the initial values, which according to Table 12.5 are 0.35 GW and 0.17 GW, respectively. The capacity credits are estimated based on the ELCC technique as described in the previous section.

To imitate the reduced original production sequence, the solar power time series is randomly generated only for 10 years and the given segment is repeated to cover the whole simulation period of 500 years. The calculations show that with the 10-year solar production series the average errors in the ELCC estimations for PV and CSP are 1% and 9%, respectively. The larger value for CSP is explained by lower number of the selected locations (Fig. 12.3) and thereby larger variation in the combined output. Based on these results and also the corresponding findings by Cunha [29] for hydropower series[3], it is concluded that the use of the renewable power production time series with length of only several decades might be sufficient for Monte Carlo based GSA evaluations. This also implies that the historical weather records, if available, could be used directly for reliability studies.

To exclude SCSR from the selected scenarios, the solar production series are substituted with the new ones generated by ignoring the spatial correlation. The results indicate that without SCSR the capacity contributions of PV and CSP are overestimated by 3% and 20%, respectively. The reason for higher capacity value (or GSA) in this case is the increased smoothing effect in the combined power fluctuations and thereby reduced intermittency of the total solar power generation. The larger error for the CSP capacity credit is again due to lower number of the production sites. Overall, the observed impact of the spatial correlation is moderate because the ramp rate limitations are ignored in the calculations. This demonstrates that the conventional GSA studies do not require high precision in the RES modeling. And yet, when the share of renewables is large and the power system operating details are incorporated into GSA assessment (see, for example, [84, 92]), the quality of the RES data could be of significant importance.

3 Cunha [29] performed the simulation-based GSA assessments of Brazilian power system by using the synthetic inflow series for 1000 years and the historical inflows covering only 40 years, and concluded that the historical records still provide acceptable results.

12.4 CONCLUDING REMARKS

A case study of generation system adequacy in peninsular Spain was performed for the present (2013) and future (2020) time scenarios by using the sequential Monte Carlo simulations. The focus areas of the study were limited to: (a) adequacy of the existing Spanish generation system and the level of redundancy, (b) capacity credit of time-dependent power sources, and (c) sensitivity of the final results to certain modeling aspects.

The Spanish power system was represented by system load, thermal generation, renewable energy sources (wind, PV, CSP and run-off-the-river hydro) and energy storage systems (reservoir-based hydro with annual, weekly and daily operating cycles). The excess of thermal generation and the capacity credits of the time-dependent power sources were estimated by using the traditional ELCC technique.

By the given study two tasks were accomplished. First, it was demonstrated how the previously proposed solar power and energy storage dispatch models could be applied to the Monte Carlo based GSA assessments. And second, additional knowledge was obtained on generation adequacy in peninsular Spain. In case of the latter the main findings are as follows:

- The Spanish generation system is over-dimensioned. When setting the target reliability to LOLE=2.4 hours/year, the redundant capacity at present is estimated to be 13.8 GW or 31.4% of the total thermal generation.

- Wind, solar and hydro power facilities in Spain altogether have a significant capacity value, reaching currently 16.65 GW. The capacity credits of individual sources are: 15% – wind, 7% – solar (same for PV and CSP), 32% – run-off-the-river hydro and 56–84% – reservoir-based hydro. As expected, the capacity contribution of intermittent sources decreases in relative terms with the increased penetration levels.

- The low capacity credit of the solar power plants is due to poor match between the seasonal and daily variations of the solar radiation and system load. The use of thermal storage in case of CSP does not provide any notable gain in the capacity value, which means that the adopted CSP dispatch control aimed at maximizing production at each timestep is ineffective from reliability point of view. To increase the capacity value of CSP plant its dispatch strategy should take into account the hours of the daily peak load.

- With the increased penetration of renewables, the largest qualitative change in the operation of the reservoir-based hydro occurs at a daily timescale and primarily due to the solar power. At longer timescales, however, the impact of renewables is relatively small, which implies that the available total water reservoir capacity in Spain is sufficient to accommodate very high share of intermittent electricity.

- The use of the renewable power production time series with length of only several decades might be sufficient for the Monte Carlo based GSA evaluations. This also implies that the historical weather records, if available, could be used directly for reliability studies.
- The use of the solar production series ignoring the spatial correlation leads to moderate overestimation of the capacity contributions of PV and CSP plants. This demonstrates that the conventional adequacy studies do not require high precision in the modeling of renewable energy. And yet, when the share of renewables is large and the power system operating details are incorporated into GSA assessment, the quality of the RES data could be of significant importance.

Part VI

CONCLUSIONS

13 CONCLUSIONS

The general objective of this thesis was to develop solar power and energy storage models for generation system adequacy (GSA) studies based on the sequential Monte Carlo technique. The final models had to be reasonably simplified to reduce the overall calculation time. The simplification also concerned the minimization of the required specific knowledge and input data.

To achieve the goal of the thesis, the following four tasks were completed. First, a solar radiation model was developed for creating synthetic values of the hourly radiation. Second, simplified models of photovoltaic and concentrated solar (parabolic trough and central receiver based) power plants were developed for translating solar radiation to the corresponding power production. Third, a general dispatch model of energy storage was developed by taking into account the inherent characteristics of the simulation-based adequacy evaluations. And finally, a case study of GSA in peninsular Spain was performed by applying the developed models.

The main contributions and conclusions of the thesis and future work are presented in the following text.

13.1 THESIS CONTRIBUTIONS

- Regression analysis of extensive historical solar radiation data and derivation of the mathematical expressions that allow quantifying the spatial correlation of solar radiation (SCSR) for any two locations at monthly and daily timescales by using intersite distance and the clearness index long-term statistics (*novel and original contribution*)
- Development of general procedure for incorporating SCSR into the clearness index based single-site stochastic algorithms and thus enabling their use for multisite generation of the synthetic solar radiation data
- Development of moderately simplified and yet precise models for the parabolic trough and central receiver based power plants
- Development of general and flexible dispatch model of energy storage for the simulation-based GSA studies allowing natural combination of the normal and emergency operations and realistic representation of the storage level variations (*novel and original contribution*)
- Assessment of generation adequacy in peninsular Spain by applying the new solar power and energy storage dispatch models, estimation of the capacity credit of time-dependent power sources and the study of its sensitivity to certain modeling aspects

13.2 CONCLUSIONS ON SOLAR RADIATION MODELING

A solar radiation model (SRM) was developed to create synthetic values of the hourly total, beam and diffuse radiation on a horizontal plane for single or multiple locations. SRM basically represents a set of single-site univariate stochastic algorithms which are extended for multisite data generation by using the existing methods of linear algebra and the empirical relations characterizing the spatial correlation of solar radiation. The only required inputs are the long-term monthly average clearness index values $\widehat{\mathrm{KT}}_{month}$ and the site geographic coordinates.

Single-site model of solar radiation

The single-site SRM is based on the traditional techniques which deploy the clearness index KT as a primary predictor variable. The calculation procedure involves determining:

1. the monthly KT time series by adding Gaussian noise to the long-term average values (the Bohlen approach)
2. the daily KT sequence by using a library of Markov transition matrices (the Aguiar daily algorithm)
3. the hourly KT series with the time-dependent, autoregressive Gaussian model (the Aguiar hourly or TAG algorithm)
4. the diffuse and beam components of solar radiation by applying the Boland-Ridley-Lauret (BRL) approximation.

To improve the overall precision, the BRL and the TAG models were adjusted based on the additional investigations.

The single-site SRM was validated as an integrated tool, assuming that the individual adopted methods perform adequately as described in the original references. The validation was done simply by statistical comparison of the synthetic and typical meteorological year data for 8 selected locations. The results showed a good match between the generated total radiation sequence and the reference data. In case of direct normal radiation, relatively larger deviations were observed, with the monthly mean value of 4.1%, which are attributed to inherent limitations of the BRL and other similar approximations for the diffuse solar fraction.

Incorporation of spatial correlation

The task of incorporating the spatial correlation into SRM was accomplished in two steps. In the first step a hypothesis was made that at long timescales simple characterizations of SCSR are possible. To test the hypothesis, the author performed a regression analysis of the satellite-derived monthly and daily ramp rates of the clearness index ΔKT for over 300,000 location pairs in 4 US regions. Based on the given analysis, which is the first original contribution of the thesis, it was found that:

- The adequate response variables are standard deviation of difference (SDD) for the monthly timescale and normalized standard deviation of the difference (NSDD) and Pearson's correlation coefficient (PCC) for the daily timescale.
- In addition to the distance, the relevant explanatory variable is the indicator of intersite dependence defined as $X_{14} = \mathtt{std}(\Delta\widehat{KT}_{\mathtt{month(a)}} - \Delta\widehat{KT}_{\mathtt{month(b)}})$.
- The relation between the selected input and output parameters shows linear and quadratic trends at monthly and daily timescales, respectively.

The cross-validation of the obtained regression functions by using the additional dataset with over 1500 location pairs across Spain and Germany showed reasonable goodness of fit ($R^2 > 0.7 - 0.8$), and thus confirmed the underlying hypothesis.

In the second step, by applying the derived SCSR formulae and the existing methods of linear algebra, a general procedure was introduced for incorporating SCSR into univariate stochastic algorithms. The procedure deploys the common technique of enforcing spatial correlation between output parameters by feeding a given stochastic model with the spatially correlated random number streams. The numerical tests were performed by using two conventional stochastic solar radiation algorithms of different complexities. In both cases a good match was observed between the expected (from the regression models) and simulated values of the spatial correlation, which confirmed the effectiveness of the proposed procedure. The comparisons of the generated and actual solar radiation values also demonstrated that the quality of the synthetic data is reasonable and it improves with integration of SCSR.

It is important to note that on the hourly timescale the SCSR characterization was not possible due to significance of local weather factors. This means that the spatial correlation cannot be incorporated into the hourly stochastic algorithm (e. g. the TAG model) based on the proposed procedure. The resultant impact on the quality of the synthetic solar radiation data, however, is expected to be small. The reasons are that: (a) the spatial correlation at short timescales is relatively low, and (b) the use of the spatially correlated $KT_{\mathtt{day}}$ values to generate the $KT_{\mathtt{hour}}$ time series allows capturing, at least partially, the hourly SCSR.

13.3 CONCLUSIONS ON SOLAR POWER PLANT MODELING

Simplified models of photovoltaic and concentrated solar (parabolic trough and central receiver based) power plants were proposed for the application in generation system adequacy studies based on the sequential Monte Carlo technique.

The precision of the developed models was validated for multiple case scenarios by using the simulations in System Advisor Model (SAM) as a reference.

Model of photovoltaic power plant

The proposed photovoltaic (PV) system model combines the long-established Hay-Davies-Klucher-Reindl correlation for calculating solar radiation on a tilted surface and a reduced version of the 5-parameter model for converting the incident radiation to net power output. In comparison, the reduced PV array performance model uses approximately 20 input parameters and 7 equations less than the original 5-parameter model.

The results from the validation study demonstrated the adequacy of the adopted PV array performance model. In particular, it was shown that:

- The average total deviations in the predicted annual and monthly net production from PV plant are in the range of 2–7%, which is comparable to the margin of error of the SAM calculations.
- The performance of the proposed model to a certain extent is independent of the PV cell technology and is determined mainly by the nominal efficiency of the cell $\eta_{\mathrm{pv,src}}$; the lower is the parameter, the lower is the model precision.
- The exclusion of the daily and seasonal variations of the ambient temperature reduces the model precision, though in some cases the opposite effect is observed as a result of the partial compensation of individual errors from the modeling simplifications.

Model of concentrated solar power plant

The proposed concentrated solar power (CSP) models use the simplified simulation procedure consisting of three steps: (a) calculation of the solar field thermal output, (b) plant dispatch and conversion of useful thermal energy to gross power, and (c) estimation of parasitic losses and net production.

The total number of input parameters and equations required for predicting CSP plant production was reduced approximately down to 25 and 20, respectively.

The results from the validation study demonstrated the adequacy of the adopted approaches to model reduction. In particular, it was shown that:

- The solar field output can be estimated with the average monthly deviation of up to 3% during the summer period even by ignoring the ambient temperature and assuming the constant thermal energy losses.

- The proposed procedure for creating the heliostat field layout and the correlation for shadowing and blocking efficiency can significantly simplify the optical performance estimation for tower system.
- The Rankine cycle calculations can be performed with the mean monthly error of up to 2% (summer) by modeling the power block efficiency simply as a polynomial of the relative loading.
- The plant parasitic losses can be determined with the average monthly deviation of less than 1% (summer) by scaling the parameters that have the highest influence on them.
- The average total deviations in the predicted net production from trough/-tower plant are: 1.1/1.6% (annual), 2.0/2.4% (summer month) and 8.5/9.7% (summer day).
- The overall calculation time when using the simplified CSP models is reduced by approximately 20–40 times.

13.4 CONCLUSIONS ON ENERGY STORAGE DISPATCH MODELING

A new methodology was proposed for modeling energy storage dispatch in generation system adequacy evaluations based on the sequential Monte Carlo simulations. It represents the second original contribution of the thesis. Aimed for generality and flexibility, the methodology can be applied to the systems with various mix and types of ESS, renewable and conventional generation. The required input data for ESS are easily available and include: main technical parameters and their constraints, long-term average storage level and capacity factor in consumption mode.

According to the developed approach, energy storage is deployed to reduce the renewable energy curtailments and thermal generation capacity, which allows natural combination of its normal and emergency operations. The main novelties in this case are: (a) the use of detrended residual load during ESS control to be able to consider renewable power production and distinguish between different operating timescales, and (b) the correction of ESS dispatch based on the classical proportional integral controller technique to achieve a realistic representation of storage level variations.

The individual calculation steps of the proposed methodology were demonstrated through a simple adequacy analysis of a generation system comprising thermal power plants and hydroelectric ESS with annual and daily operating cycles.

The proposed modeling methodology also opens up possibilities for other applications beyond the reliability assessment studies as the new dispatch model provides an important insight on the expected operation of ESS.

13.5 CONCLUSIONS ON CASE STUDY

A case study of generation system adequacy in peninsular Spain was performed for the present (2013) and future (2020) time scenarios by using the sequential Monte Carlo simulations. The focus areas of the study were limited to: (a) adequacy of the existing Spanish generation system and the level of redundancy, (b) capacity credit of time-dependent power sources, and (c) sensitivity of the final results to certain modeling aspects.

The Spanish power system was represented by system load, thermal generation, renewable energy sources (wind, PV, CSP and run-off-the-river hydro) and energy storage systems (reservoir-based hydro with annual, weekly and daily operating cycles). The excess of thermal generation and the capacity credits of the time-dependent power sources were estimated by using the effective load carrying capability as the metric.

By the given study two tasks were accomplished. First, it was demonstrated how the previously proposed solar power and energy storage dispatch models could be applied to the Monte Carlo based GSA assessments. And second, additional knowledge was obtained on generation adequacy in peninsular Spain. In case of the latter the main findings are as follows:

- The Spanish generation system is over-dimensioned. When setting the target reliability to LOLE=2.4 hours/year, the redundant capacity at present is estimated to be 13.8 GW or 31.4% of the total thermal generation.

- Wind, solar and hydro power facilities in Spain altogether have a significant capacity value, reaching currently 16.65 GW. The capacity credits of individual sources are: 15% – wind, 7% – solar (same for PV and CSP), 32% – run-off-the-river hydro and 56–84% – reservoir-based hydro. As expected, the capacity contribution of intermittent sources decreases in relative terms with the increased penetration levels.

- The low capacity credit of the solar power plants is due to poor match between the seasonal and daily variations of the solar radiation and system load. The use of thermal storage in case of CSP does not provide any notable gain in the capacity value, which means that the adopted CSP dispatch control aimed at maximizing production at each timestep is ineffective from reliability point of view. To increase the capacity value of CSP plant its dispatch strategy should take into account the hours of the daily peak load.

- With the increased penetration of renewables, the largest qualitative change in the operation of the reservoir-based hydro occurs at a daily timescale and primarily due to the solar power. At longer timescales, however, the impact of renewables is relatively small, which implies that the available total water reservoir capacity in Spain is sufficient to accommodate very high share of intermittent electricity.

- The use of the renewable power production time series with length of only several decades might be sufficient for the Monte Carlo based GSA evaluations. This also implies that the historical weather records, if available, could be used directly for reliability studies.
- The use of the solar production series ignoring the spatial correlation leads to moderate overestimation of the capacity contributions of PV and CSP plants. This demonstrates that the conventional adequacy studies do not require high precision in the modeling of renewable energy. And yet, when the share of renewables is large and the power system operating details are incorporated into GSA assessment, the quality of the renewable production data could be of significant importance.

13.6 FUTURE WORK

Solar radiation modeling:

Characterization of the spatial correlation of solar radiation by using the clear-sky index instead of the clearness index, investigation of possible new applications of the SCSR regression functions in power system studies, demonstration of the proposed procedure for multisite synthetic data generation by using univariate stochastic algorithms other than those chosen in this thesis

Solar power plant modeling:

Development of the simplified energy models for the third-generation (nanotechnology based) PV cells

Energy storage dispatch modeling:

Further development of the proposed energy storage dispatch model, particularly for more complex types of energy storage, such as multi-purpose multi-reservoir hydroelectric systems; investigation of possible new applications of the given dispatch model in power system studies

Generation system reliability assessment:

Evaluation of the impact of various modeling aspects (e. g. synthetic weather data versus historical records, original length of the time series, model complexity, spatial and inter-variable correlation, analytical versus simulation methods); development of methods for estimating complete reliability (i. e. both adequacy and security) of generation system which would require taking into account the system operating details.

Part VII

APPENDIX

A EFFECT OF AMBIENT TEMPERATURE IN MODELING PARABOLIC TROUGH SYSTEM

The thermal energy loss in solar collector directly depends on the difference between the heat transfer fluid (HTF) temperature T_{HTF} and ambient temperature T_{amb}. This relation for parabolic trough (PTR) systems tends to be quadratic [72, 144], but by assuming that T_{HTF} is constant and the variations of T_{amb} are moderate, it can be linearized as follows:

$$Q_{rec,loss} = C_{ptr}\,(T_{HTF} - T_{amb}), \tag{A.1}$$

where C_{ptr} is the constant estimated based on PTR design operating point.

The effect of including the ambient temperature into the PTR model through (A.1) is tested by performing the concentrated solar power plant simulations for the same case scenarios as in the main validation study (see Chapter 9). The hourly ambient temperature values are taken from SAM. T_{HTF} is approximated by (290+390)/2=340°C, the average of the typical inlet and outlet temperatures in the PTR field [109].

The solar field output predictions by the adopted and the alternative PTR models are compared in Figs. A.1 and A.2 for the case of Madrid where the largest change is observed. The absolute decrease in the net power deviations achieved with the alternative approach in this case is 0.24% (annual) and 0.9% (monthly). When including other locations, the corresponding precision gain on average is 0.14% (annual) and 0.33% (monthly).

The obtained results show that with the addition of T_{amb} into the modeling the predictions for winter months improve, yet as the relative production during this period is relatively small, the change in the overall precision is negligible.

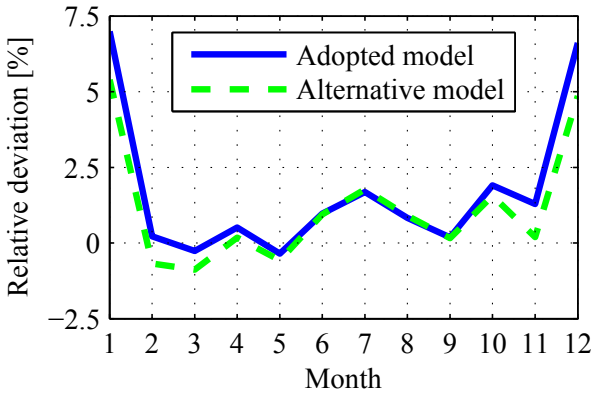

Figure A.1: Deviations in the monthly SF output for PTR plant (Madrid, SM_{csp}=2.5)

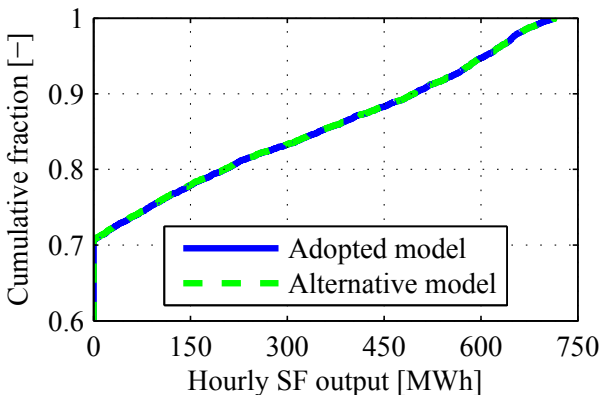

Figure A.2: Cumulative distribution of the hourly SF output for PTR plant (Madrid, SM_{csp}=2.5)

B IDENTIFICATION OF HYDROELECTRIC SYSTEM PARAMETERS

In this work a simple procedure is proposed for estimating the missing parameters of hydroelectric energy storage system (ESS) and it is applied to the case study of the Spanish power system as described in Part V.

The required input data comprise:

V_{max}	maximum reserve volume capacity
P_{max}	installed capacity
E_{max}	maximum reservoir energy capacity
E_{aver}	average reservoir energy capacity
η_h	head-to-power conversion efficiency
λ_H	ratio of minimum to maximum hydraulic head
λ_V	ratio of minimum to maximum reservoir volume

And the assumed outputs are:

A, B	constants describing the reservoir geometry
Q_{max}	maximum water discharge rate
V_{aver}	long-term average value of the reservoir water volume

The power conversion process is formulated as:

$$V = A + B\,H_h \tag{B.1}$$

$$P = \eta_h\,\rho\,g\,H_h\,Q, \tag{B.2}$$

where V is the reservoir water volume; P is the power; H_h is the net hydraulic head; Q is the water discharge rate; ρ is the water density; and g is the gravitational constant.

The calculation steps are the following. The constant A is determined by using the definitions of λ_H and λ_V together with (B.1)

$$\lambda_H = \frac{H_{min}}{H_{max}} = \frac{V_{min} - A}{V_{max} - A} \quad \Rightarrow \tag{B.3}$$

$$\Rightarrow \quad A = \frac{V_{min} - \lambda_H V_{max}}{1 - \lambda_H} = V_{max}\frac{\lambda_V - \lambda_H}{1 - \lambda_H} \tag{B.4}$$

The relation between the reservoir energy E_0 and volume V_0 capacities is derived by assuming that E_0 is the total energy produced by emptying the reservoir from the given level V_0 with maximum discharge Q_{max} (ignoring the power limitation), i. e. :

$$E_0 = \int_0^{t_0} P\,dt; \quad Q(t) = Q_{max}; \quad V(t) = V_0 - Q_{max}t; \quad t_0 = \frac{V_0 - V_{min}}{Q_{max}} \tag{B.5}$$

By combining (B.5) with (B.1), (B.2) one can obtain

$$\begin{aligned} E_0 &= \int_0^{t_0} P dt = \int_0^{t_0} \eta_h \rho g Q_{max} H_h(t) dt = \eta_h \rho g Q_{max} \int_0^{t_0} \frac{V(t) - A}{B} dt \\ &= \frac{\eta_h \rho g Q_{max}}{B} \int_0^{t_0} (V_0 - A - Q_{max} t) dt \\ &= \frac{\eta_h \rho g Q_{max}}{B} \left(V_0 t_0 - A t_0 - \frac{Q_{max} t_0^2}{2} \right) \\ &= \frac{\eta_h \rho g}{B} \left(\frac{V_0^2}{2} - A V_0 - \frac{V_{min}^2}{2} + A V_{min} \right), \end{aligned} \tag{B.6}$$

which, in turn, allows defining the constant B by setting $E_0 = E_{max}$, $V_0 = V_{max}$ and using (B.4)

$$B = \frac{\eta_h \rho g V_{max}^2 (1 - \lambda_V)^2 (1 + \lambda_H)}{2 E_{max} (1 - \lambda_H)} \tag{B.7}$$

Once A, B are known, the value of V_{aver} is calculated from (B.6). Finally, Q_{max} is estimated from (B.1), (B.2) by assuming $P = P_{max}$ and $V = V_{max}$.

One should note that the described approach to calibrate ESS parameters is rather simple and used only to obtain physically consistent data. It is not intended for precise reproduction of the actual hydro power plants. However, with more extensive reference data the calibration approach could be modified to improve the modeling accuracy.

BIBLIOGRAPHY

[1] E. Aguado. Local-scale variability of daily solar radiation–San Diego County, California. *Journal of Climate and Applied Meteorology*, 25(5): 672–678, 1986.

[2] R.J. Aguiar and M. Collares-Pereira. TAG: A time-dependent, autoregressive, Gaussian model for generating synthetic hourly radiation. *Solar Energy*, 49(3):167–174, 1992.

[3] R.J. Aguiar, M. Collares-Pereira, and J.P. Conde. Simple procedure for generating sequences of daily radiation values using a library of Markov transition matrices. *Solar Energy*, 40(3):269–279, 1988.

[4] R.N. Allan and J. Roman. Reliability assessment of hydrothermal generation systems containing pumped storage plant. *IEE Proceedings on Generation, Transmission and Distribution*, 138(6):471–478, 1991.

[5] R.N. Allan, R. Li, and M.M. Elkateb. Modelling of pumped-storage generation in sequential Monte Carlo production simulation. *IEE Proceedings on Generation, Transmission and Distribution*, 145(5):611–615, 1998.

[6] J.D. Álvarez, J.L. Guzmán, L.J. Yebra, and M. Berenguel. Hybrid modeling of central receiver solar power plants. *Simulation Modelling Practice and Theory*, 17(4):664–679, 2009.

[7] M. Amelin. Comparison of capacity credit calculation methods for conventional power plants and wind power. *IEEE Transactions on Power Systems*, 24(2):685–691, 2009.

[8] D. Arvizu, P. Balaya, L. Cabeza, T. Hollands, A. Jäger-Waldau, M. Kondo, ..., and R. Zilles. Direct solar energy. In IPCC special report on renewable energy sources and climate change mitigation. Technical report, 2011.

[9] K.J. Åström and T. Hägglund. *PID controllers: theory, design, and tuning*. Instrument Society of America, Research Triangle Park, 2 edition, 1995.

[10] V. Badescu. *Modeling Solar Radiation at the Earth's Surface: Recent Advances*. Springer, 2008.

[11] J. Badosa, M. Haeffelin, and H. Chepfer. Scales of spatial and temporal variation of solar irradiance on Reunion tropical island. *Solar Energy*, 88(0):42–56, 2013.

[12] Bagen and R. Billinton. Evaluation of different operating strategies in small stand-alone power systems. *IEEE Transactions on Energy Conversion*, 20(3):654–660, 2005.

[13] D. Barlev, R. Vidu, and P. Stroeve. Innovation in concentrated solar power. *Solar Energy Materials and Solar Cells*, 95(10):2703–2725, 2011.

[14] O. Behar, A. Khellaf, and K. Mohammedi. A review of studies on central receiver solar thermal power plants. *Renewable and Sustainable Energy Reviews*, 23(0):12–39, 2013.

[15] F.A. Bhuiyan and A. Yazdani. Reliability assessment of a wind-power system with integrated energy storage. *IET Renewable Power Generation*, 4(3):211–220, 2010.

[16] R. Billinton and R.N. Allan. *Reliability Evaluation of Power Systems*. Springer, 1996.

[17] R. Billinton and Bagen. Generating capacity adequacy evaluation of small stand-alone power systems containing solar energy. *Reliability Engineering & System Safety*, 91(4):438–443, 2006.

[18] R. Billinton and W. Li. *Reliability Assessment of Electrical Power Systems Using Monte Carlo Methods*. Springer, 1994.

[19] R. Billinton and W. Wangdee. Impact of utilising sequential and non-sequential simulation techniques in bulk-electric-system reliability assessment. *IEE Proceedings on Generation, Transmission and Distribution*, 152(5):623–628, 2005.

[20] N. Blair, N. Sather, and A. Dobos. Case studies comparing System Advisor Model (SAM) results to real performance data. In *Proc. of Int. Conf. ASES/WREF*, 2012.

[21] S.J. Bode and P. Gauché. Review of optical software for use in concentrated solar power systems. In *Proc. of Southern African Solar Energy Conference (SASEC)*, May 2012.

[22] M. Bohlen and J. Schumacher. Time series analysis of the long term monthly horizontal solar radiation. In *Proc. of EuroSun'96*, pages 1503–1507, 1996.

[23] C. Cameron, W. Boyson, and D. Riely. Comparison of PV system performance-model predictions with measured PV system performance. In *Proc. of IEEE Conf. Photovoltaic Specialists*, May 2008.

[24] G. Caralis and A. Zervos. Value of wind energy on the reliability of autonomous power systems. *IET Renewable Power Generation*, 4(2): 186–197, 2010.

[25] CEER. Assessment of electricity generation adequacy in European countries. Technical Report C13-ESS-32-03, Council of European Energy Regulators, March 2014.

[26] CENER. Tonatiuh – a Monte Carlo ray tracer for the optical simulation of solar concentrating systems. The National Renewable Energy Center of Spain. Available from: http://code.google.com/p/tonatiuh.

[27] M.K. Chang, J.D. Eichman, F. Mueller, and S. Samuelsen. Buffering intermittent renewable power with hydroelectric generation: A case study in California. *Applied Energy*, 112(0):1–11, 2013.

[28] G. Ciulla, V. Lo Brano, V. Di Dio, and G. Cipriani. A comparison of different one-diode models for the representation of I-V characteristic of a PV cell. *Renewable and Sustainable Energy Reviews*, 32(0):684–696, 2014.

[29] S.H.F. Cunha, F.B.M. Ganes, G.C. Oliveira, and M.V.F. Pereira. Reliability evaluation in hydrothermal generating systems. *IEEE Transactions on Power Apparatus and Systems*, PAS-101(12):4665–4673, 1982.

[30] M. David, P. Lauret, and J. Boland. Evaluating tilted plane models for solar radiation using comprehensive testing procedures, at a southern hemisphere location. *Renewable Energy*, 51(0):124–131, 2013.

[31] M.W. Davis, A.H. Fanney, and B.P. Dougherty. Evaluating building integrated photovoltaic performance models. In *Proc. of IEEE Conf. Photovoltaic Specialists*, pages 1642–1645, May 2002.

[32] A. de Miguel, J. Bilbao, R. Aguiar, H. Kambezidis, and E. Negro. Diffuse solar irradiation model evaluation in the North Mediterranean Belt area. *Solar Energy*, 70(2):143–153, 2001.

[33] W. de Soto. Improvement and validation of a model for photovoltaic array performance. Master's thesis, University of Wisconsin-Madison, 2004.

[34] W. De Soto, S.A. Klein, and W.A. Beckman. Improvement and validation of a model for photovoltaic array performance. *Solar Energy*, 80 (1):78–88, 2006.

[35] C. Demain, M. Journée, and C. Bertrand. Evaluation of different models to estimate the global solar radiation on inclined surfaces. *Renewable Energy*, 50(0):710–721, 2013.

[36] P. Denholm, E. Ela, B. Kirby, and M. Milligan. The role of energy storage with renewable electricity generation. Technical Report NREL/TP-6A2-47187, Jan 2010.

[37] J. D'Errico. Matlab functions for polynomial regression modeling. Available from: http://mathworks.com/matlabcentral/fileexchange/34765-polyfitn, 2011.

[38] J. D'Errico. Matlab function for finding the nearest positive definite matrix. Available from: http://mathworks.com/matlabcentral/fileexchange/42885-nearestspd, 2013.

[39] M. Diez-Mediavilla, A. de Miguel, and J. Bilbao. Measurement and comparison of diffuse solar irradiance models on inclined surfaces in Valladolid (Spain). *Energy Conversion and Management*, 46(13):2075–2092, 2005.

[40] DLR. Greenius – the green energy system analysis tool. The German Aerospace Center. Available from: http://freegreenius.dlr.de.

[41] J.A. Duffie and W.A. Beckman. *Solar Engineering of Thermal Processes*. John Wiley & Sons, 2006.

[42] J. Ehnberg. *Autonomous power systems based on renewables – On generation reliability and system control*. PhD thesis, Chalmers University of Technology, 2007.

[43] J. Ehnberg and M. Bollen. Reliability of a small power system using solar power and hydro. *Electric Power Systems Research*, 74(1):119–127, 2005.

[44] D. Elmakias. *New Computational Methods in Power System Reliability*. Studies in Computational Intelligence. Springer, 2008.

[45] B. Elmegaard and N. Houbak. Software for simulation of power plant processes. Part B – program description and application. In *Proc. of ECOS 2002*, 2002.

[46] B. Elmegaard and N. Houbak. DNA, a general energy system simulation tool. In *Proc. of SIMS 2005*, pages 43–52, 2005.

[47] D.G. Erbs. *Models and applications for weather statistics related to building heating and cooling loads*. PhD thesis, University of Wisconsin-Madison, 1984.

[48] ESRU. ESP-r. Energy Systems Research Unit, University of Strathclyde. Available from: http://www.esru.strath.ac.uk/Programs/ESP-r.

[49] F-Chart Software. Engineering Equation Solver (EES). Available from: http://fchart.com/ees.

[50] Z.Y. Gao, P. Wang, and J. Wang. Impacts of energy storage on reliability of power systems with WTGs. In *Proc. of IEEE 11th Int. Conf. Probabilistic Methods Applied to Power Systems (PMAPS)*, pages 65–70, June 2010.

[51] P. Garcia, A. Ferriere, and J.J. Bezian. Codes for solar flux calculation dedicated to central receiver system applications: A comparative review. *Solar Energy*, 82(3):189–197, 2008.

[52] J. García-Barberena, P. Garcia, M. Sanchez, M.J. Blanco, C. Lasheras, A. Padrós, and J. Arraiza. Analysis of the influence of operational strategies in plant performance using SimulCET, simulation software for parabolic trough power plants. *Solar Energy*, 86(1):53–63, 2012.

[53] L.L. Garver. Effective load carrying capability of generating units. *IEEE Transactions on Power Apparatus and Systems*, PAS-85(8):910–919, 1966.

[54] GE Energy. Western wind and solar integration study. Technical Report NREL/SR-550-47434, May 2010.

[55] C. Gertig, A. Delgado, C. Hidalgo, and R. Ron. SoFia – a novel simulation tool for central receiver systems. *Energy Procedia*, 49(0):1361–1370, 2014.

[56] V.A. Graham and K.G.T. Hollands. A method to generate synthetic hourly solar radiation globally. *Solar Energy*, 44(6):333–341, 1990.

[57] V.A. Graham, K.G.T. Hollands, and T.E. Unny. A time series model for Kt with application to global synthetic weather generation. *Solar Energy*, 40(2):83–92, 1988.

[58] I. Guyon and A. Elisseeff. An introduction to variable and feature selection. *Journal of Machine Learning Research*, 3:1157–1182, 2003.

[59] B. E. Hansen. Econometrics. Draft graduate textbook. University of Wisconsin. Available from: http://ssc.wisc.edu/~bhansen/econometrics, Jan 2013.

[60] S. Herrera, J.M. Gutiérrez, R. Ancell, M. R. Pons, M.D. Frías, and J. Fernández. Development and analysis of a 50-year high-resolution daily gridded precipitation dataset over Spain (Spain02). *International Journal of Climatology*, 32(1):74–85, 2012.

[61] C.K. Ho. Software and codes for analysis of concentrating solar power technologies. Technical Report SAND2008-8053, Sandia National Laboratories, Dec 2008.

[62] T.E. Hoff and R. Perez. Modeling PV fleet output variability. *Solar Energy*, 86(8):2177–2189, 2012.

[63] P. Hu, R. Karki, and R. Billinton. Reliability evaluation of generating systems containing wind power and energy storage. *IET Generation, Transmission and Distribution*, 3(8):783–791, 2009.

[64] IDAE. Plan de Energías Renovables 2011-2020 (*Renenewable Energies Plan 2011-2020*). Technical report, Instituto para la Diversificación y Ahorro de la Energía, IDAE (*The Spanish Institute for Energy Diversification and Saving*), Nov 2011.

[65] IEA. Solar Energy Perspectives. Technical report, International Energy Agency, Dec 2011.

[66] IEA. Technology roadmap: Solar Thermal Electricity. Technical report, International Energy Agency, Sept 2014.

[67] IEA. Technology roadmap: Solar Photovoltaic Energy. Technical report, International Energy Agency, Sept 2014.

[68] IEA. Technology roadmap: Energy storage (including technology annex). Technical report, International Energy Agency, March 2014.

[69] P. Ineichen. Comparison and validation of three global-to-beam irradiance models against ground measurements. *Solar Energy*, 82(6):501–512, 2008.

[70] C.P. Jacovides, F.S. Tymvios, V.D. Assimakopoulos, and N.A. Kaltsounides. Comparative study of various correlations in estimating hourly diffuse fraction of global solar radiation. *Renewable Energy*, 31 (15):2492–2504, 2006.

[71] S.A. Jones, R. Pitz-Paal, P. Schwarzboezl, N. Blair, and R. Cable. TRNSYS modeling of the SEGS VI parabolic trough solar electric generating system. In *Proc. of ASME Int. Solar Energy Forum*, 2001.

[72] S.A. Kalogirou. *Solar Energy Engineering: Processes and Systems*. Processes and Systems Series. Elsevier Science, 2009.

[73] R. Karki, Po Hu, and R. Billinton. Reliability evaluation considering wind and hydro power coordination. *IEEE Transactions on Power Systems*, 25(2):685–693, 2010.

[74] R. Karki, A. Alferidi, and R. Billinton. Reliability modeling for evaluating the contribution of photovoltaics in electric power systems. In *Proc. of 37th IEEE Conf. Photovoltaic Specialists*, pages 1811–1816, June 2011.

[75] A. Keane, M. Milligan, C.J. Dent, B. Hasche, C. D'Annunzio, K. Dragoon, ..., and M. O'Malley. Capacity value of wind power. *IEEE Transactions on Power Systems*, 26(2):564–572, 2011.

[76] M. Khalili, F. Brissette, and R. Leconte. Stochastic multi-site generation of daily weather data. *Stoch. Env. Res. Risk Assess.*, 23:837–849, 2009.

[77] D.L. King, W.E. Boyson, and J.A. Kratochvill. Photovoltaic array performance model. Technical Report SAND2004-3535, Sandia National Laboratories, Dec 2004.

[78] B.L. Kistler. A user's manual for DELSOL3: a computer code for calculating the optical performance and optimal system design for solar thermal central receiver plants. Technical Report SAND86-8018, Sandia National Laboratories, Nov 1986.

[79] G.T. Klise and J.S. Stein. Models used to assess the performance of photovoltaic systems. Technical Report SAND2009-8258, Sandia National Laboratories, Dec 2009.

[80] L.H. Koh, Z.Y. Gao, P. Wang, and K.J. Tseng. Impact of energy storage and variability of PV on power system reliability. *Energy Procedia*, 33 (0):302–310, 2013.

[81] D. Koller and M. Sahami. Toward optimal feature selection. In *Proc. of 13th Int. Conf. on Machine Learning*, pages 284–292, 1996.

[82] M. Lalwani, D.P. Kothari, and M. Singh. Investigation of solar photovoltaic simulation softwares. *International Journal of Applied Engineering Research*, 1(3):585–601, 2010.

[83] T. Larraín, R. Escobar, and J. Vergara. Performance model to assist solar thermal power plant siting in northern Chile based on backup fuel consumption. *Renewable Energy*, 35(8):1632–1643, 2010.

[84] A.M. Leite da Silva, W.S. Sales, L.A. da Fonseca Manso, and R. Billinton. Long-term probabilistic evaluation of operating reserve requirements with renewable sources. *IEEE Transactions on Power Systems*, 25(1): 106–116, 2010.

[85] A.M. Leite da Silva, W.S. Sales, L.A. da Fonseca Manso, and R. Billinton. Long-term probabilistic evaluation of operating reserve requirements with renewable sources. *IEEE Transactions on Power Systems*, 25(1): 106–116, 2010.

[86] M. Lin, H. C. Lucas, and G. Shmueli. Research commentary – Too big to fail: large samples and the p-value problem. *Information Systems Research*, 24(4):906–917, 2013.

[87] I. Llorente García, J.L. Álvarez, and D. Blanco. Performance model for parabolic trough solar thermal power plants with thermal storage: Comparison to operating plant data. *Solar Energy*, 85(10):2443–2460, 2011.

[88] T. Ma, H. Yang, L. Lu, and J. Peng. Technical feasibility study on a standalone hybrid solar-wind system with pumped hydro storage for a remote island in Hong Kong. *Renewable Energy*, 69(0):7–15, 2014.

[89] S.H. Madaeni, R. Sioshansi, and P. Denholm. Capacity value of concentrating solar power plants. Technical Report NREL/TP-6A20-51253, June 2011.

[90] S.H. Madaeni, R. Sioshansi, and P. Denholm. Comparison of capacity value methods for photovoltaics in the Western United States. Technical Report NREL/TP-6A20-54704, July 2012.

[91] S.H. Madaeni, R. Sioshansi, and P. Denholm. Estimating the capacity value of concentrating solar power plants with thermal energy storage: A case study of the southwestern United States. *IEEE Transactions on Power Systems*, 28(2):1205–1215, 2013.

[92] M. Matos, J.P. Lopes, M. Rosa, R. Ferreira, A. Leite da Silva, W. Sales, ..., and R. López. Probabilistic evaluation of reserve requirements of generating systems with renewable power sources: the Portuguese and Spanish cases. *International Journal of Electrical Power & Energy Systems*, 31(9):562–569, 2009.

[93] C. Mendívil Ruas. Almacenamiento de energía mediante bombeo (*Pumped energy storage*). In *Proc. of Madrid Workshop on Energy Storage*, Oct 2013.

[94] Meteonorm. Handbook part II: theory. Version 7.1. Available from: http://meteonorm.com, Sept 2014.

[95] Ministry of Agriculture, Food and Environment of Spain. Hydrological data. Available from: http://magrama.gob.es.

[96] Ministry of Environment of Spain (former). Libro blanco del agua en España (*White book of water in Spain*), 2000.

[97] MIT. Managing large-scale penetration of intermittent renewables. Technical report, MIT Energy Initiative, April 2011.

[98] R.M. Moharil and P.S. Kulkarni. Reliability analysis of solar photovoltaic system using hourly mean solar radiation data. *Solar Energy*, 84(4):691–702, 2010.

[99] J.D. Mondol, Y.G. Yohanis, and B. Norton. Solar radiation modelling for the simulation of photovoltaic systems. *Renewable Energy*, 33(5): 1109–1120, 2008.

[100] M.J. Montes, A. Abánades, J.M. Martínez-Val, and M. Valdés. Solar multiple optimization for a solar-only thermal power plant, using oil as heat transfer fluid in the parabolic trough collectors. *Solar Energy*, 83 (12):2165–2176, 2009.

[101] M. Mosadeghy, T.K. Saha, and Ruifeng Yan. Increasing wind capacity value in Tasmania using wind and hydro power coordination. In *Proc. of IEEE Power and Energy Society General Meeting*, pages 1–5, July 2013.

[102] NASA. Surface meteorology and solar energy. Atmospheric Science Data Center. Available from: http://eosweb.larc.nasa.gov/sse.

[103] Natural Resources Canada. RETScreen International. Available from: http://retscreen.net.

[104] NCDC. National Solar Radiation Data Base (NSRDB). US National Climatic Data Center. Available from: http://ncdc.noaa.gov/data-access/land-based-station-data/land-based-datasets/solar-radiation.

[105] NERC. Generating availability data system. The North American Electric Reliability Corporation. Available from: http://www.nerc.com.

[106] NERC. Methods to model and calculate capacity contributions of variable generation for resource adequacy planning. Technical report, The North American Electric Reliability Corporation, March 2011.

[107] A.M. Noorian, I. Moradi, and G.A. Kamali. Evaluation of 12 models to estimate hourly diffuse irradiation on inclined surfaces. *Renewable Energy*, 33(6):1406–1412, 2008.

[108] G. Notton, C. Cristofari, and P. Poggi. Performance evaluation of various hourly slope irradiation models using Mediterranean experimental data of Ajaccio. *Energy Conversion and Management*, 47(2):147–173, 2006.

[109] NREL. System Advisor Model. Available from: http://sam.nrel.gov.

[110] NREL. PVWatts Calculator. Available from: http://pvwatts.nrel.gov.

[111] NREL. SolTrace optical modeling software. Available from: http://nrel.gov/csp/soltrace.

[112] M. Oukili, S. Zouggar, M. Seddik, F. Vallée, M. El Hafyani, and T. Ouchbel. Evaluation of the Moroccan power grid adequacy with introduction of concentrating solar power (CSP) using solar tower and parabolic trough mirrors technology. *Energy Procedia*, 42(0):113–122, 2013.

[113] J.E. Pacheco. Final test and evaluation results from the Solar Two project. Technical Report SAND2002-0120, Sandia National Laboratories, Jan 2002.

[114] A.M. Patnode. Simulation and performance evaluation of parabolic trough solar power plants. Master's thesis, University of Wisconsin-Madison, 2006.

[115] S. Pelland and I. Abboud. Comparing photovoltaic capacity value metrics: a case study for the city of Toronto. *Progress in Photovoltaics: Research and Applications*, 16(8):715–724, 2008.

[116] R. Perez, P. Ineichen, R. Seals, and A. Zelenka. Making full use of the clearness index for parameterizing hourly insolation conditions. *Solar Energy*, 45(2):111–114, 1990.

[117] R. Perez, R. Seals, A. Zelenka, and P. Ineichen. Climatic evaluation of models that predict hourly direct irradiance from hourly global irradiance: Prospects for performance improvements. *Solar Energy*, 44(2): 99–108, 1990.

[118] R. Perez, P. Ineichen, E.L. Maxwell, R. Seals, and A. Zelenka. Dynamic global to direct conversion models. *ASHRAE Transactions*, 98(1):154–168, 1992.

[119] R. Perez, R. Seals, and R. Stewart. Assessing the load matching capability of photovoltaics for US utilities based upon satellite-derived insolation data. In *Proc. of 23d IEEE Conf. Photovoltaic Specialists*, pages 1146–1151, May 1993.

[120] R. Perez, R. Margolis, M. Kmiecik, M. Schwab, and M. Perez. Update: effective load-carrying capacity of photovoltaics in the United States. Technical Report NREL/CP-620-40068, June 2006.

[121] R. Posadillo and R. L. Luque. Evaluation of the performance of three diffuse hourly irradiation models on tilted surfaces according to the utilizability concept. *Energy Conversion and Management*, 50(9):2324–2330, 2009.

[122] R. Posadillo and R. L. Luque. The generation of hourly diffuse irradiation: A model from the analysis of the fluctuation of global irradiance series. *Energy Conversion and Management*, 51(4):627–635, 2010.

[123] H. Price. A parabolic trough solar power plant simulation model. Technical Report NREL/CP-550-33209, Jan 2003.

[124] B.E. Psiloglou and H.D. Kambezidis. Estimation of the ground albedo for the Athens area, Greece. *Journal of Atmospheric and Solar-Terrestrial Physics*, 71(8-9):943–954, 2009.

[125] T.M. Razykov, C.S. Ferekides, D. Morel, E. Stefanakos, H.S. Ullal, and H.M. Upadhyaya. Solar photovoltaic electricity: current status and future prospects. *Solar Energy*, 85(8):1580–1608, 2011.

[126] REE. Technical information for the Spanish power system. Red Eléctrica de España. Available from: http://ree.es.

[127] REE. Importancia del equipo generador hidroeléctrico en la operación del sistema eléctrico. Instalaciones hidroeléctricas estratégicas (*Importance of hydroelectric generation equipment in power system operation. Strategic hydroelectric installations)*. Technical report, Red Eléctrica de España, Feb 2009.

[128] J. Revuelta, C. Longás, and L. Imaz. Generation adequacy with large scale integration of renewable energy sources. In *Proc. of CIGRE*, pages 1–8, Aug 2012.

[129] C.W. Richardson and D.A. Wright. *WGEN: A model for generating daily weather variables*. U.S. Dept. of Agriculture, Agricultural Research Service, 1984.

[130] B. Ridley, J. Boland, and P. Lauret. Modelling of diffuse solar fraction with multiple predictors. *Renewable Energy*, 35(2):478–483, 2010.

[131] M.M. Rolim, N. Fraidenraich, and C. Tiba. Analytic modeling of a solar power plant with parabolic linear collectors. *Solar Energy*, 83(1):126–133, 2009.

[132] R.W. Beck, Inc. Distributed renewable energy operating impacts and valuation study. Technical report, Jan 2009.

[133] A. Safdarian, M. Fotuhi-Firuzabad, and F. Aminifar. Compromising wind and solar energies from the power system adequacy viewpoint. *IEEE Transactions on Power Systems*, 27(4):2368–2376, 2012.

[134] SBC. Factbook: Concentrating solar power. Technical report, SBC Energy Institute, June 2013.

[135] SBC. Factbook: Solar photovoltaic. Technical report, SBC Energy Institute, Sept 2013.

[136] SBC. Factbook: Electricity storage. Technical report, SBC Energy Institute, Sept 2013.

[137] C.K. Simoglou, P.N. Biskas, E.A Bakirtzis, A.N. Matenli, A.I. Petridis, and A.G. Bakirtzis. Evaluation of the capacity credit of RES: the Greek case. In *Proc. of IEEE Conf. POWERTECH*, pages 1–6, June 2013.

[138] R. W. Sinnott. Virtues of the Haversine. *Sky and Telescope*, 68:159, 1984.

[139] R. Sioshansi, S.H. Madaeni, and P. Denholm. A dynamic programming approach to estimate the capacity value of energy storage. *IEEE Transactions on Power Systems*, 29(1):395–403, 2014.

[140] V. Siva Reddy, S.C. Kaushik, K.R. Ranjan, and S.K. Tyagi. State-of-the-art of solar thermal power plants: a review. *Renewable and Sustainable Energy Reviews*, 27(0):258–273, 2013.

[141] A. Skartveit and J.A. Olseth. A model for the diffuse fraction of hourly global radiation. *Solar Energy*, 38(4):271–274, 1987.

[142] E. Skoplaki and J.A. Palyvos. On the temperature dependence of photovoltaic module electrical performance: A review of efficiency/power correlations. *Solar Energy*, 83(5):614–624, 2009.

[143] J. Spelling, D. Favrat, A. Martin, and G. Augsburger. Thermoeconomic optimization of a combined-cycle solar tower power plant. *Energy*, 41 (1):113–120, 2012.

[144] W.B. Stine and M. Geyer. Power from the sun. Available from: http://powerfromthesun.net/book.htm, 2001.

[145] T. Stoffel, D. Renné, D. Myers, S. Wilcox, M. Sengupta, R. George, and C. Turchi. Concentrating solar power. Best practices handbook for the collection and use of solar resource data. Technical Report NREL/TP-550-47465, Sept 2010.

[146] P.M. Subcommittee. IEEE reliability test system. *IEEE Transactions on Power Apparatus and Systems*, PAS-98(6):2047–2054, 1979.

[147] P.W. Suckling. Spatial coherence of incoming solar radiation for the Southern Piedmont. *Southeastern Geographer*, 35(2):183–193, 1995.

[148] C. Tiba and N. Fraidenraich. Analysis of monthly time series of solar radiation and sunshine hours in tropical climates. *Renewable Energy*, 29(7):1147–1160, 2004.

[149] J.L. Torres, M. de Blas, A. García, and A. de Francisco. Comparative study of various models in estimating hourly diffuse solar irradiance. *Renewable Energy*, 35(6):1325–1332, 2010.

[150] University of Wisconsin-Madison. TRNSYS – a transient systems simulation program. Available from: http://sel.me.wisc.edu/trnsys.

[151] US Department of Energy. EnergyPlus energy simulation software. weather data. Available from: http://apps1.eere.energy.gov/buildings/energyplus/weatherdata_about.cfm.

[152] J. Usaola. Capacity credit of concentrating solar power. *IET Renewable Power Generation*, 7(6):680–688, 2013.

[153] C. Vernaya, S. Pitaval, and P. Blanc. Review of satellite-based surface solar irradiation databases for the engineering, the financing and the operating of photovoltaic systems. In *Proc. of ISES Solar World Congress*, pages 1–9, 2013.

[154] M.J. Wagner. Simulation and predictive performance modeling of utility-scale central receiver system power plants. Master's thesis, University of Wisconsin-Madison, 2008.

[155] M.J. Wagner and P. Gilman. Technical manual for the SAM physical trough model. Technical Report NREL/TP-5500-51825, June 2011.

[156] P.H. Wagner and M. Wittmann. Influence of different operation strategies on transient solar thermal power plant simulation models with molten salt as heat transfer fluid. *Energy Procedia*, 49(0):1652–1663, 2014.

[157] H. Wang and X. Bai. Adequacy assessment of generating systems incorporating wind, PV and energy storage. In *Proc. of IEEE Conf. Innovative Smart Grid Technologies (ISGT Asia)*, pages 1–6, May 2012.

[158] W. Wangdee, L. Wenyuan, and R. Billinton. Coordinating wind and hydro generation to increase the effective load carrying capability. In *Proc. of IEEE 11th Int. Conf. Probabilistic Methods Applied to Power Systems (PMAPS)*, pages 337–342, June 2010.

[159] WATSUN. WATGEN user's manual. Watsun Simulation Laboratory, University of Waterloo, Aug 1992.

[160] D.S. Wilks. Simultaneous stochastic simulation of daily precipitation, temperature and solar radiation at multiple sites in complex terrain. *Agricultural and Forest Meteorology*, 96(1):85–101, 1999.

[161] D.S. Wilks and R.L. Wilby. The weather generation game: a review of stochastic weather models. *Progress in Physical Geography*, 23(3):329–357, 1999.

[162] Xcel Energy. An effective load carrying capability analysis for estimating the capacity value of solar generation resources on the Public Service Company of Colorado system. Technical report, Feb 2009.

[163] Z. Yao, Z. Wang, Z. Lu, and X Wei. Modeling and simulation of the pioneer 1 MW solar thermal central receiver system in China. *Renewable Energy*, 34(11):2437–2446, 2009.

[164] R. Zheng and J. Zhong. Generation adequacy assessment for power systems with wind turbine and energy storage. In *Proc. of IEEE Conf. Innovative Smart Grid Technologies (ISGT)*, pages 1–6, Jan 2010.

COLOPHON

This document was typeset by using slightly modified version of the typographical look-and-feel `classicthesis` developed by André Miede. The style was inspired by Robert Bringhurst's seminal book on typography "*The Elements of Typographic Style*". `classicthesis` is available for both LaTeX and LyX:

http://code.google.com/p/classicthesis/

Happy users of `classicthesis` usually send a real postcard to the author, a collection of postcards received so far is featured here:

http://postcards.miede.de/

Final Version as of April 6, 2015 (`classicthesis` version 4.0).